CUKUROVA UNIVERSITY

INSTITUTE OF NATURAL AND APPLIED SCIENCES

PhD THESIS

Improvement of Low-Temperature Properties of Hydrocarbon Selective Catalytic Reduction Activity by Developing Copper-Based Zeolite Catalyst

Ali Cem YAKARYILMAZ

Department of Automotive Engineering

January, 2025

CUKUROVA UNIVERSITY

INSTITUTE OF NATURAL AND APPLIED SCIENCES

PhD THESIS APPROVAL

Improvement of Low-Temperature Properties of Hydrocarbon Selective Catalytic Reduction Activity by Developing Copper-Based Zeolite Catalyst

---

Ali Cem YAKARYILMAZ

Department of Automotive Engineering

This Doctorate Thesis was evaluated by the following Jury Members on 13/01/2025 and was approved by unanimity / ~~majority of votes~~.

Jury : Assoc. Prof. Dr. Tayfun ÖZGÜR (Advisor) ……

: Prof. Dr. Ali KESKİN ……

: Prof. Dr. Gökhan TÜCCAR ……

: Prof. Dr. Mustafa Atakan AKAR ……

: Assoc. Prof. Dr. Erinç ULUDAMAR ……

This Thesis was written in the Department of Automotive Engineering Institute of Natural and Applied Sciences.

Thesis Number:

Prof. Dr. Sadık DİNÇER
Director
Institute of Natural and Applied Sciences

This work was supported by the Scientific Research Project Office of Çukurova University.
Project ID: FDK-2022-15479

CONTENTS

CUKUROVA UNIVERSITY
INSTITUTE OF NATURAL AND APPLIED SCIENCES

PhD THESIS

Improvement of Low-Temperature Properties of Hydrocarbon Selective Catalytic Reduction Activity by Developing Copper-Based Zeolite Catalyst

Ali Cem YAKARYILMAZ

Advisor: Assoc. Prof. Dr. Tayfun ÖZGÜR

Department of Automotive Engineering

ABSTRACT

Selective catalytic reduction (SCR) is the most effective exhaust after-treatment technology used to reduce NO_x (nitrogen oxides) emissions from diesel engines. This system converts NO_x into harmless nitrogen (N_2) and water (H_2O) with the help of a specified catalyst and a reductant.

In this work, samarium (Sm) doped two distinct copper-based zeolite (Y and Beta) catalysts produced with the ion exchange method. Scanning Electron Microscopy (SEM), Energy Dispersive X-rat Spectroscopy (EDS), X-ray diffraction (XRD), Fourier-Transform infrared (FTIR), and Brunauer-Emmet-Teller (BET) analyses were conducted to determine the chemical characterization of the produced catalysts. Additionally, the catalysts were tested in a real exhaust flow under temperatures ranging from 150 °C to 240°C, with loads of 0, 2, and 4 kW at two different space velocities.

The predominance of Si, O, and Al was observed in all catalysts, while the presence of other utilized chemicals was also confirmed through analyses. For all catalysts, conversion rates increased with higher temperatures. While an increase in engine load positively affected the conversion rates, a higher space velocity (SV) had a negative impact.

Under a load of 4 kW, the highest NO_x conversion rates were observed at a temperature of 240°C. For the Y zeolite set, the Sm1-Y catalyst achieved the highest conversion rate of 95.7481% at an SV of 30000 h^{-1}, while the Sm2-Y catalyst demonstrated a conversion rate of 94.6600% at an SV of 40000 h^{-1}. Similarly, in the BEA zeolite set, the Sm4-BEA catalyst achieved the highest conversion rate of 95.7754% at an SV of 30000 h^{-1}, whereas the Sm1-BEA catalyst exhibited a conversion rate of 94.4719% at an SV of 40000 h^{-1}.

The incorporation of Sm showed beneficial effects across both catalyst sets. The results indicated that the optimal Sm loading levels were 1% and 2%.

Keywords: Selective Catalytic Reduction, Nitrogen Oxides, Low Temperature, Real Exhaust Flow, Zeolite.

ÇUKUROVA ÜNİVERSİTESİ
FEN BİLİMLERİ ENSTİTÜSÜ

DOKTORA TEZİ

Bakır Bazlı Zeolit Katalist Geliştirilerek Hidrokarbon Seçici Katalitik İndirgeme Aktivitesinin Düşük Sıcaklık Özelliklerinin İyileştirilmesi

Ali Cem YAKARYILMAZ

Danışman: Doç. Dr. Tayfun ÖZGÜR

Otomotiv Mühendisliği Anabilim Dalı

ÖZ

Seçici katalitik indirgeme (SCR), dizel motorlardan kaynaklanan NO_x (azot oksit) emisyonlarını azaltmak için kullanılan en etkili egzoz sonrası işlem teknolojisidir. Bu sistem, NO_x'i belirli bir katalizör ve bir indirgeme maddesi yardımıyla zararsız azot (N_2) ve suya (H_2O) dönüştürür.

Bu çalışmada, samaryum (Sm) katkılı, iki farklı bakır bazlı zeolit (Y ve Beta) katalizörleri iyon değişim yöntemiyle üretilmiştir. Üretilen katalizörlerin kimyasal özelliklerini belirlemek amacıyla Taramalı Elektron Mikroskobu (SEM), Enerji Dağılımlı X-ışını Spektroskopisi (EDS), X-ışını Kırınımı (XRD), Fourier Dönüşümlü Kızılötesi (FTIR) Spektroskopisi ve Brunauer-Emmet-Teller (BET) analizleri gerçekleştirilmiştir. Ayrıca, katalizörler 150 ile 240°C arasındaki sıcaklıklarda, 0, 2 ve 4 kW yüklerde ve iki farklı alan hızı altında gerçek bir egzoz akışında test edilmiştir.

Kimyasal analizler, tüm katalizörlerde Si, O ve Al'ın baskın olduğunu ortaya koyarken, kullanılan diğer kimyasalların da varlığı doğrulanmıştır. Performans testleri, sıcaklık artışı ile dönüşüm oranlarının arttığını göstermiştir. Motor yükündeki artış dönüşüm oranlarını olumlu etkilerken, daha yüksek bir alan hızı (SV) dönüşüm oranı üzerinde olumsuz bir etki yaratmıştır.

4 kW yük altında ve 240°C sıcaklıkta en yüksek NOx dönüşüm oranları kaydedilmiştir. Y zeolit setinde, Sm1-Y katalizörü 30000 h^{-1} SV'de %95,7481 dönüşüm oranına ulaşırken, Sm2-Y katalizörü 40000 h^{-1} SV'de %94,6600 dönüşüm oranı göstermiştir. Benzer şekilde, Beta zeolit setinde, Sm4-BEA katalizörü 30000 h^{-1} SV'de %95,7754 dönüşüm oranına ulaşmış, Sm1-BEA katalizörü ise 40000 h^{-1} SV'de %94,4719 dönüşüm oranı sergilemiştir.

Samaryum eklenmesi, her iki katalizör seti için faydalı etkiler göstermiştir. Sonuçlar, optimal Sm yükleme seviyelerinin %1 ve %2 olduğunu ve bu oranların performans ile NO_x dönüşüm verimliliğini artırdığını göstermiştir.

Anahtar Kelimeler: Seçici Katalitik İndirgeme, Azot Oksitler, Düşük Sıcaklık, Gerçek Egzoz Akışı, Zeolit.

GENİŞLETİLMİŞ ÖZET

Ateşin keşfi, insan medeniyetinin tarihinde dönüm noktası niteliğinde bir anı temsil eder. Başlangıçta bir ısıtma ve koruma aracı olarak kullanılan ateş, teknolojinin, kültürün ve toplumun gelişimini tetiklemiştir. Yüzyıllar sonra, yanmanın kontrol altına alınması daha sofistike formlara evrilerek içten yanmalı motorların icadıyla sonuçlanmış ve bu motorlar ulaşımı, sanayiyi ve modern yaşam biçimini kökten değiştirmiştir.

Bu temelin üzerine, 18. ve 19. yüzyıllardaki sanayi devrimi, yanma teknolojisinde yeni bir dönemin kapılarını açmıştır. Kömür yakarak buhar üreten ve makineleri çalıştıran buhar motorları, sanayileşmenin bel kemiği haline gelmiştir. Bu devasa makineler, benzeri görülmemiş üretim ve taşımacılık seviyelerine olanak sağlayarak hızlı kentleşme ve ekonomik büyümeyi ateşlemiştir.

Ateşin keşfinden içten yanmalı motorların ortaya çıkışına kadar olan yolculuk, insan yenilikçiliği ve ilerlemesinin dikkate değer bir hikâyesini temsil etmektedir. Bu süreç boyunca, yanma kontrol altına alınmış, geliştirilmiş ve toplumların değişen ihtiyaçlarına uyacak şekilde uyarlanmıştır. Günümüzde, enerji teknolojilerinde yeni bir dönemin eşiğinde dururken, bu yolculuğu anlamak, karşı karşıya olunan zorluklar ve fırsatlar hakkında paha biçilemez bir içgörü sunmaktadır. Bu zorlukların en önemlilerinden biri kesinlikle hava kirliliğidir.

Enerji kaynaklarının kullanımı doğası gereği emisyonların oluşmasına sebep olmaktadır ve bu da çevresel dinamikler üzerinde önemli bir etki yaratmaktadır. Enerji üretimi ve tüketim süreçlerinden kaynaklanan emisyonlar, çevresel bozulmanın ve iklim değişikliğinin kötüleşmesinin temel sebeplerindendir. Bu emisyonların başında ise karbondioksit (CO_2) gelmektedir. Ancak, araçlardan kaynaklanan emisyonlar yalnızca CO_2 ile sınırlı kalmayıp, çeşitli zararlı maddeleri de kapsamaktadır. CO_2, iklim değişikliğine olan olumsuz etkisi nedeniyle önemli bir endişe kaynağı olmaya devam ederken, araçlardan salınan azot oksitler (NO_x), partikül madde (PM), karbon monoksit (CO), hidrokarbonlar (HC) ve uçucu organik bileşikler (VOC) gibi diğer kirleticilere yönelik ilgi giderek artmaktadır. Bu kirleticiler yalnızca hava kalitesini düşürmekle kalmayıp, aynı zamanda solunum yolu hastalıklarını ve kardiyovasküler sorunları artırarak insan sağlığı için önemli riskler oluşturmaktadır.

Bu çevresel ve sağlıkla ilgili endişelere yanıt olarak, emisyon standartlarının getirilmesi, çevresel düzenlemelerde dönüm noktası niteliğinde bir anı temsil etmektedir ve endüstriyel ve araç emisyonlarının dünya çapındaki seyrini şekillendirmektedir. Bu standartlar, araçlar, enerji santralleri ve sanayi tesisleri gibi çeşitli kaynaklardan atmosfere salınan kirleticiler için izin verilen seviyeleri belirleyen ölçütler olarak hizmet etmektedir. Başlangıçta hava kalitesi ve halk sağlığına yönelik artan endişelere yanıt olarak tanıtılan emisyon standartları, zamanla iklim değişikliği ve kentsel kirlilik gibi ortaya çıkan çevresel zorluklara yanıt verecek şekilde evrim geçirmiştir.

Emisyon standartları, dünyanın farklı bölgelerinde çeşitli çevresel öncelikleri ve düzenleyici çerçeveleri yansıtarak değişiklik göstermektedir. Yaygın standart türleri arasında Avrupa

Birliği'ndeki Euro Standartları, Amerika Birleşik Devletleri'ndeki EPA Standartları, Çin Standartları, Hindistan Bharat Aşama Emisyon Standartları ve Japonya'nın Yeni Uzun Dönem Emisyon Düzenlemeleri yer almaktadır. Bu örnekler, emisyonların yönetiminde bölgesel yaklaşımların çeşitliliğini ortaya koymaktadır. Tüm bu farklılıklara rağmen, emisyon standartlarının küresel olarak uyumlaştırılmasına yönelik artan bir eğilim bulunmaktadır. Bu hareket, sınır ötesi kirlilik sorunlarını ele almayı ve iklim değişikliğinin etkilerini etkili bir şekilde hafifletmeyi amaçlamaktadır. Düzenlemelerin sınır ötesinde uyumlaştırılmasıyla, ülkeler ortak çevresel sorunları iş birliği içinde ele alarak daha sürdürülebilir bir geleceğin yolunu açabileceklerdir.

Hem dizel hem de benzinli araçlar için uygulanan emisyon standartları her geçen gün daha da katı hale gelmekte ve özellikle dizel motorlu araçlar için oldukça zorlu gereklilikler ortaya koymaktadır. Dizel motorlar, hava sıkıştırılarak yüksek bir sıcaklığa ulaştırılması ve bu sıcaklığın, yanma odasına enjekte edilen yakıtı tutuşturması prensibiyle çalışır. Bu süreç oldukça verimlidir ve yüksek tork sağlar, bu nedenle dizel motorlar çeşitli uygulamalarda popüler bir tercih haline gelmiştir. Dizel yanmasının temel prensibi, yakıt içerisinde depolanan kimyasal enerjinin kendine özgü bir şekilde açığa çıkarılmasına dayanır. Bu sürecin gerçekleşmesi için, yakıta oksijenin (O_2) hassas bir şekilde sağlanması gerekir. Yakıt-hava karışımının hazırlanması olarak bilinen bu karışım hazırlama aşaması, yanma reaksiyonunun verimliliği ve tamlığı üzerinde belirleyici bir rol oynar. Dizel motorlar, genellikle benzinli motorlara göre daha yüksek sıcaklıklarda çalışır. Bu yüksek sıcaklıklar, havadaki azotun oksijenle reaksiyona girmesi sonucu azot oksitlerin (NO_x) oluşumuna katkıda bulunur. Sonuç olarak, dizel egzozu, NO_x emisyonlarının birincil ve en temel kaynağı haline gelir. Üstelik, benzer boyuttaki benzinli motorlardan daha güçlü ve yakıt açısından daha verimli olan dizel motorların sayısındaki artış bu durumu daha da belirgin hale getirmektedir.

NO_x emisyonları, azaltılması gereken en kritik kirleticiler arasında yer alsa da dizel motorlarla donatılmış araçlarda kullanılan emisyon kontrol yöntemleri büyük önem taşımaktadır. Bu amaç doğrultusunda kullanılan başlıca sistemler arasında dizel oksidasyon katalizörleri (DOC), dizel partikül filtreleri (DPF), egzoz gazı resirkülasyonu (EGR), zayıf NO_x tuzakları (LNT) ve seçici katalitik indirgeme sistemleri (SCR) bulunmaktadır.

Bu çalışmanın odak noktasında ise SCR sistemleri yer almaktadır. SCR sistemleri, çok çeşitli konfigürasyonlarda tasarlanabilmektedir. Bir indirgeme maddesi ve bir katalizör olmak üzere iki ana bileşenden oluşan bu sistemler, farklı indirgeme maddesi türleri ve katalizör malzemeleriyle çeşitli kombinasyonlar için son derece uyarlanabilir yapıdadır.

Performansı artırmak ve spesifik yüzey alanını genişletmek amacıyla, SCR sistemlerinde çeşitli malzemeler katalizör taşıyıcıları olarak kullanılmaktadır. Yaygın olarak kullanılan taşıyıcılar arasında, termal kararlılığı ve mekanik dayanımı ile bilinen bir seramik malzeme olan kordiyerit ($2Al_2O_3 \cdot 5SiO_2 \cdot 2MgO$) ve yüksek yüzey alanıyla aktif katalitik bileşenler için mükemmel bir temel sağlayan alümina (Al_2O_3) yer almaktadır. Silika (SiO_2), termal direnci ve katalitik aktiviteyi artırmak için sıklıkla alümina ile birleştirilirken, titanya (TiO_2), sülfür zehirlenmesine karşı direnci nedeniyle

vanadyum bazlı katalizörlerin desteklenmesi için tercih edilmektedir. Mikro gözenek kristal yapıları ve yüksek iyon değişim kapasiteleri ile zeolitler, amonyak-SCR reaksiyonlarında yaygın olarak kullanılmaktadır. Bu katalizör taşıyıcıları, SCR sisteminin belirli çalışma koşulları ve performans gerekliliklerine göre seçilmektedir.

Katalizör üretiminde kullanılan kordiyerit yapısı, spesifik yüzey alanını artırmak için oksalik asit ile ön işleme tabi tutulmuştur. Bu ön işlem, aktif alanlara erişimi artırarak katalizörün genel performansını iyileştirmeyi hedeflemiştir. Bir sonraki aşamada, iki farklı zeolit türü (Y ve BEA) ile iyon değişim sürecinde bakır (Cu) kullanılmıştır. Ardından, katalizörün dayanıklılığını artırmak amacıyla seryum (Ce) eklenmiştir. Ayrıca, azot oksit (NO_x) dönüşüm aktivitesi üzerindeki etkisini değerlendirmek için farklı oranlarda samaryum (Sm) ilave edilmiştir.

Üretilen katalizörlerin kimyasal karakterizasyonlarını yapabilmek adına SEM, EDS, XRD, FT-IR ve BET gibi analizlere tabi tutulmuştur.

Üretilen katalizörler, NO_x dönüşüm oranlarını belirlemek amacıyla SCR performans testine tabi tutulmuştur. Testler, 30000 ve 40000 h^{-1} alan hızlarında, 150°C ile 240°C arasındaki bir sıcaklık aralığında gerçekleştirilmiştir. Deneyler, yük uygulanmadan ve iki farklı yük koşulunda (2 kW ve 4 kW) yapılmış olup, indirgeme maddesi olarak etanol kullanılmıştır.

Y zeolit setinde, en yüksek spesifik yüzey alanı 143,7719 m^2/g ile Sm1-Y katalizörüne aittir. Buna karşılık, BEA setinde en yüksek spesifik yüzey alanına sahip katalizör, 74,8524 m^2/g değeri ile Sm2-BEA olmuştur. Tüm katalizörler için, sıcaklık artışı ile NO_x dönüşüm oranları iyileşmiştir. Motor yükündeki artış, dönüşüm oranlarını olumlu yönde etkilerken, daha yüksek bir alan hızı (SV) dönüşüm oranı üzerinde olumsuz bir etki yaratmıştır.

Y zeolit setinde, 4 kW yük altında, en yüksek NO_x dönüşüm oranı %95,7481 ile 30000 h^{-1} SV'de Sm1-Y katalizörü kullanılarak elde edilmiştir. Daha yüksek bir SV olan 40000 h^{-1}'de ise Sm2-Y katalizörü, %94,6600 NO_x dönüşüm oranı göstermiştir. Benzer şekilde, BEA zeolit setinde 4 kW yük altında, en yüksek NO_x dönüşüm oranı %95,7754 ile 30000 h^{-1} SV'de Sm4-BEA katalizörü ile gözlemlenmiştir. 40000 h^{-1} SV'de ise Sm1-BEA katalizörü, %94,4719 NO_x dönüşüm oranı sergilemiştir.

Sm eklemesi her iki katalizör seti için olumlu etkiler göstermiştir. Sonuçlara dayanarak, en uygun Sm yükleme oranlarının %1 ve %2 olduğu sonucuna varılmıştır.

Bu araştırmanın, farklı Sm oranları ve taşıyıcı türleri bağlamında Sm ile modifiye edilmiş SCR katalizörlerinin performansı hakkında değerli bilgiler sağlaması beklenmektedir. Ayrıca, etanolün bir indirgeme maddesi olarak kullanılabilirliği de araştırılacaktır. Elde edilen bulgular, literatürde tanımlanan boşluğu doldurmaya ve verimli ve sürdürülebilir SCR sistemlerinin geliştirilmesine katkı sağlayacaktır.

ACKNOWLEDGEMENTS

First and foremost, I would like to extend my profound appreciation to my thesis advisor, Assoc. Prof. Dr. Tayfun Özgür, for his exceptional guidance, unwavering support, and continuous encouragement throughout the course of this study.

I am equally thankful to Prof. Dr. Ali Keskin, Dean of the Faculty of Engineering, for granting me the privilege of using the thesis template, which significantly streamlined the structuring of this work. Furthermore, I wish to convey my sincere gratitude to the Head of the Automotive Engineering Department, Prof. Dr. Mustafa Özcanlı, for his invaluable assistance and decisive motivation during my academic endeavors.

Special thanks are due to Assit. Prof. Dr. Erdi Tosun and Sinan Keyinci for their invaluable assistance and support. Their contributions have been invaluable to the success of this research.

I would also like to acknowledge the other professors in the Automotive Engineering Department for their guidance and dedication, which have significantly enhanced my learning experience. I would like to extend a special thanks to Şafak Yıldızhan, who is no longer in our department but left a lasting impression with her valuable contributions..

I am grateful to my assistant Dr. colleagues and fellow assistant friends for their constant encouragement and support, creating an environment of collaboration and learning.

Besides, I am grateful to the Çukurova University Scientific Research Project Office for them financial support under contract no: FDK-2022-15479.

My deepest gratitude goes to my beloved wife, Sümeyye, and my beautiful daughter, Beren, who bring endless joy and love into my life. I am forever thankful to my father, Mehmet Kamil, and my mother, Gülden, who have always supported and believed in me, and helping me reach this point. I am also incredibly grateful to my wonderful sisters, Çiğdem and Şükran Ela, who mean the world to me.

LIST OF TABLES

LIST OF FIGURES

SYMBOLS AND ABBREVIATIONS

°	: Degree
µm	: Micrometer
A	: Ampere
ASC	: Ammonia slip catalyst
BET	: Brunauer-Emmett-Teller
C	: Celsius
CAA	: Clean Air Act
CAD	: Crank angle degree
CI	: Compression ignition
cm	: Centimeter
cpsi	: Cells per square inch
DC	: Direct current
DEF	: Diesel exhaust fluid
DOC	: Diesel oxidation catalyst
DPF	: Diesel particulate filter
ECE	: Economic Commission for Europe
EDX/EDS	: Energy dispersive x-ray spectroscopy
EGR	: Exhaust gas recirculation
ELR	: European Load Response
EPA	: Environmental Protection Agency
ESC	: European Steady [State] Cycle
FT-IR	: Fourier transform infrared spectroscopy
g	: Gram
GHSV	: Gas hourly space velocity
GVW	: Gross vehicle weight
h	: Hour
HDV	: Heavy-duty vehicle
ID	: Ignition delay
IPCC	: Intergovernmental Panel on Climate Change
kg	: Kilogram
kHz	: Kilohertz
kW	: Kilowatt
L	: Liter
LEV	: Low emission vehicle
LNT	: Lean NOx trap

m : Meter
mA : Milliampere
mg : Milligram
min : Minute
ml : Milliliter
mm : Millimeter
NMHC : Non-methane hydrocarbons
NMOG : Non-methane organic gases
P : Pressure
Pa : Pascal
PVP : Polyvinylpyrrolidone
PWM : Pulse width modulation
rpm : Revolutions per minute
SCR : Selective catalytic reduction
SCRF : Selective catalytic reduction filter
sec : Second
SEM : Scanning electron microscopy
SI : Spark ignition
SULEV : Super ultra-low emission vehicle
SUV : Sport utility vehicle
TDC : Top dead center
TEM : Transmission electron microscopy
TPD : Temperature-programmed desorption
TPR : Temperature-programmed reduction
TWh : Terawatt-hours
ULEV : Ultra-low-emission vehicle
V : Voltage
VOCs : Volatile organic compounds
W : Watt
WHSC : World Harmonized Stationary Cycle
WHTC : World Harmonized Transient Cycle
WNTE : World Harmonized Not-To-Exceed
XPS : X-ray photoelectron spectroscopy
XRD : X-ray diffraction
ZEV : Zero emission vehicle

1. INTRODUCTION

The discovery of fire marks a pivotal moment in the history of human civilization. From its humble beginnings as a tool for warmth and protection, fire catalyzed the development of technology, culture, and society. Millennia later, the harnessing of combustion evolved into more sophisticated forms, culminating in the invention of internal combustion engines, which revolutionized transportation, industry, and the modern way of life.

The earliest evidence of controlled fire dates back to nearly 1.7 million years ago, with our ancient ancestors mastering the art of kindling flames for cooking, heating, and warding off predators. Fire transformed the human experience, providing not only sustenance but also a means for crafting tools and shaping the environment to human advantage (Wrangham, 2017).

As civilizations flourished, so too did the utilization of combustion. The Bronze Age saw the refinement of metalworking techniques, fueled by the intense heat of furnaces. The Iron Age further propelled this progress, with advancements in smelting and forging techniques powered by coal-fired furnaces. Fire became synonymous with human ingenuity, driving innovation in metallurgy, ceramics, and beyond (Tylecote, 1992).

The industrial revolution of the 18th and 19th centuries ushered in a new era of combustion technology. Steam engines, utilizing the power of burning coal to produce steam and drive machinery, became the backbone of industrialization. These monumental machines facilitated unprecedented levels of production and transportation, sparking rapid urbanization and economic growth.

However, it was the development of the internal combustion engine in the late 19th and early 20th centuries that truly revolutionized the world. Building upon principles established by earlier inventors such as Nikolaus Otto and Étienne Lenoir, pioneers like Karl Benz and Rudolf Diesel engineered compact, efficient engines capable of converting the energy released by burning fuel into mechanical work. These engines powered the automobiles, airplanes, and ships that transformed global travel and trade, shrinking distances and connecting distant corners of the world.

The journey from the discovery of fire to the advent of internal combustion engines represents a remarkable trajectory of human innovation and progress. Along the way, combustion has been harnessed, refined, and adapted to meet the evolving needs of societies. Today, as human beings stand on the cusp of a new era of energy technology, understanding this journey provides invaluable insight into the challenges and opportunities that lie ahead. One of the most crucial of these challenges is undoubtedly air pollution.

The fact that the world population and its needs are increasing daily also increases the need for energy. When looking at the use of energy, it can be seen that it is used in many areas, from small-scale to large stationary applications, from light-duty to heavy-duty machines, and especially in vehicles that people frequently prefer to transfer from one place to another. Figure 1.1 shows the

details of the primary energy consumption by source worldwide. Although there are quite a variety of energy sources, it is seen that most of the energy obtained from these sources is from fossil fuel sources. This graph covers the period between 1970 and 2022. 180000 terawatt-hours (TWh) of energy was consumed in 2022 and the main energy sources providing energy are oil with 52970 TWh, coal with 44854 TWh, and natural gas with 39413 TWh. Among the renewable energy sources, the most abundant one is hydropower with 11300 TWh (Ritchie and Rosado, 2024).

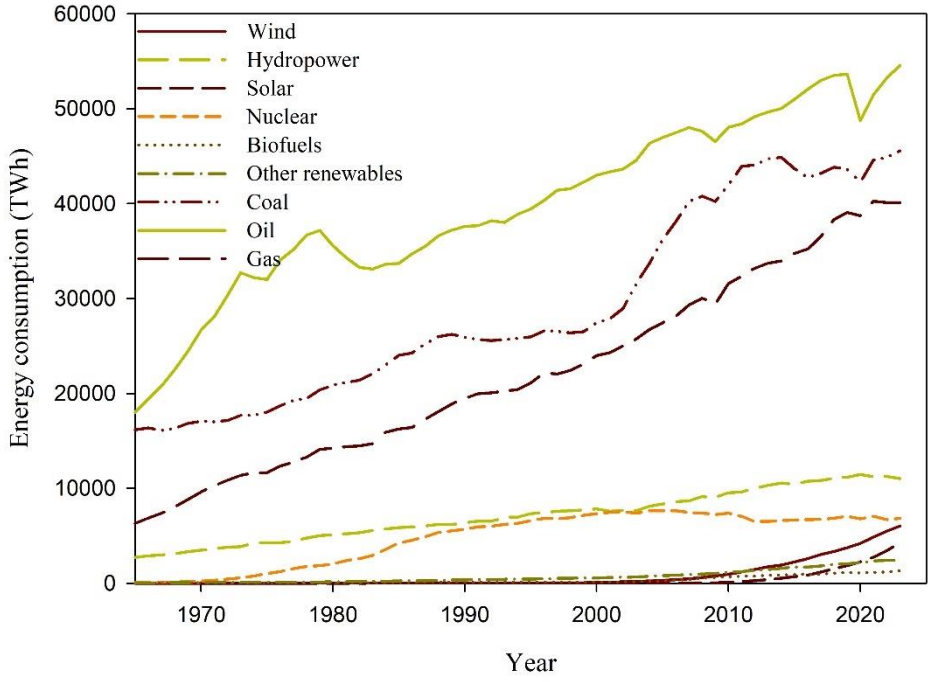

Figure 1.1. World primary energy consumption by source

The utilization of energy resources inherently entails the generation of emissions, thereby exerting a substantial influence on environmental dynamics. Emission releases stemming from energy production and consumption processes are pivotal contributors to environmental degradation and the exacerbation of climate change. At the forefront of these emissions lies carbon dioxide (CO_2) (Ritchie, 2023). In Figure 1.2 annual CO_2 emissions are illustrated worldwide except for land use. This graph shows only CO_2 emissions from fossil fuels and industry. In this chart, it is obvious that the growth of global emissions from the mid-18th century through to today. Before the advent of the Industrial Revolution, emissions levels remained minimal. After this era, the escalation in emissions was gradual until the mid-20th century. In 1950, global CO_2 emissions stood at 6 billion tonnes. By 1990, this figure had surged nearly quadrupled, surpassing 20 billion tonnes. Since then, emissions have exhibited a sustained rapid expansion, currently exceeding 35 billion tonnes annually. While recent years have witnessed a deceleration in the rate of growth, emissions have not yet attained their zenith (Ritchie and Roser, 2024).

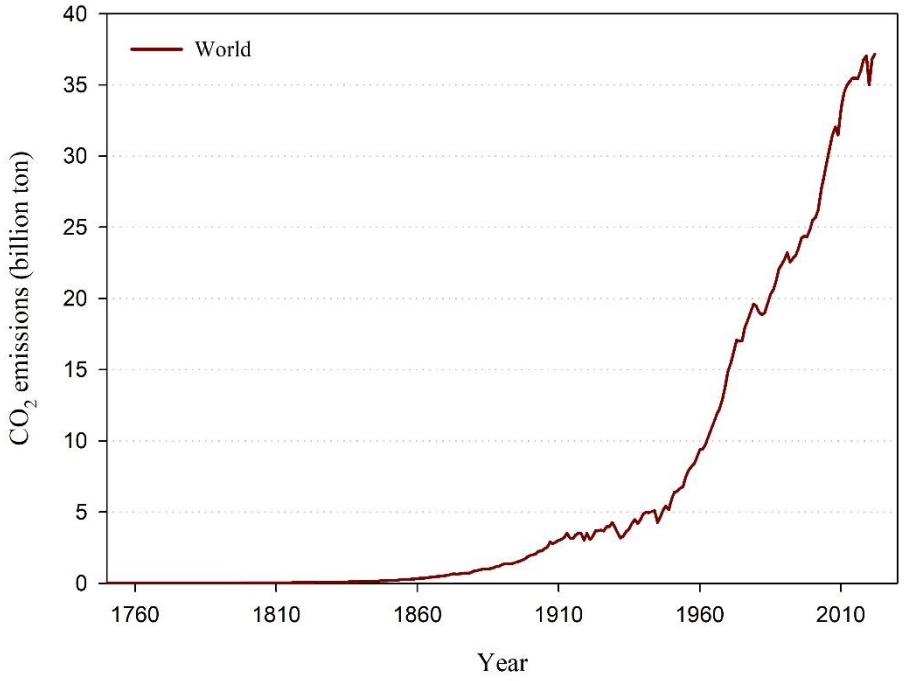

Figure 1.2. Annual CO_2 emissions (Intergovernmental Panel on Climate Change (IPCC), 2023)

Human emissions of carbon dioxide and other greenhouse gases are the primary drivers of the global rise in temperatures (Intergovernmental Panel on Climate Change (IPCC), 2023). This link between global temperatures and greenhouse gas concentrations – especially CO_2 – has been true throughout Earth's history (Lacis et al., 2010). Paris Agreement temperature goal covers keeping the global average temperature rise well below 2°C and pursuing efforts to limit warming to 1.5°C (Ritchie, 2023). In Figure 1.3, the global average temperature is relative to a baseline, which is the average between 1961 and 1990. Average temperatures have risen by over 0.8°C since then. Temperatures in 1850 were around 0.4°C cooler than the baseline, giving a total temperature rise of about 1.2°C compared to pre-industrial times. This warming has not been equally distributed across the world. The Northern Hemisphere has warmed more than the Southern Hemisphere and warming has been especially strong at the poles. In some regions, temperatures have risen by more than 5°C (Rohde, 2023).

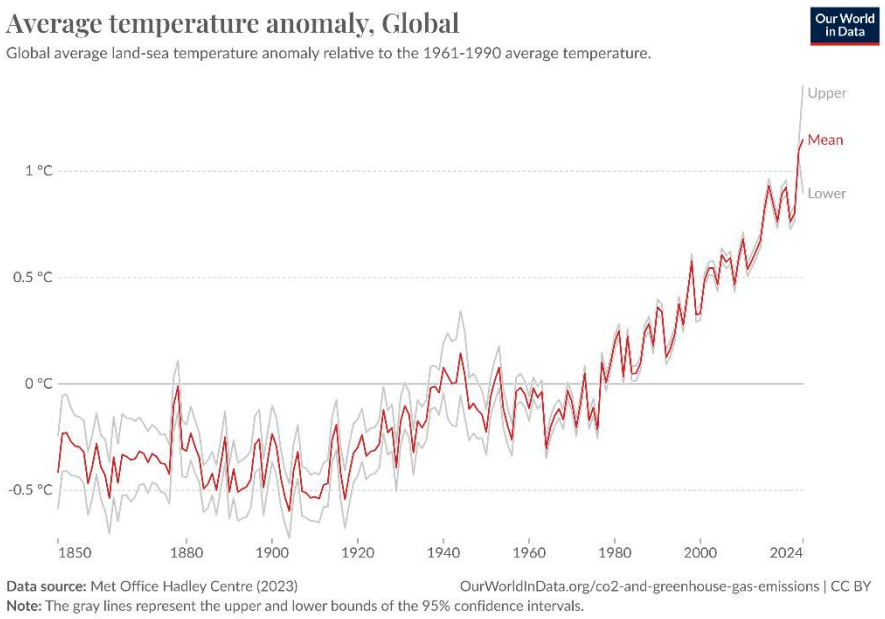

Figure 1.3. Average temperature anomaly, Global (International Energy Agency, 2022)

Transport accounts for around one-fifth of global CO_2 emissions. In Figure 1.4, it can be seen global transport emissions in 2018 (International Energy Agency, 2022). Road transportation constitutes a significant portion of carbon emissions within the transport sector, contributing to three-quarters of its total emissions. Predominantly, this emission is attributed to passenger vehicles, encompassing cars and buses, which collectively contribute 45.1%. Additionally, freight-carrying trucks account for 29.4% of these emissions. Given that the entire transport sector contributes to 21% of total emissions, road transportation alone is responsible for 15% of total CO_2 emissions (Ritchie, 2020).

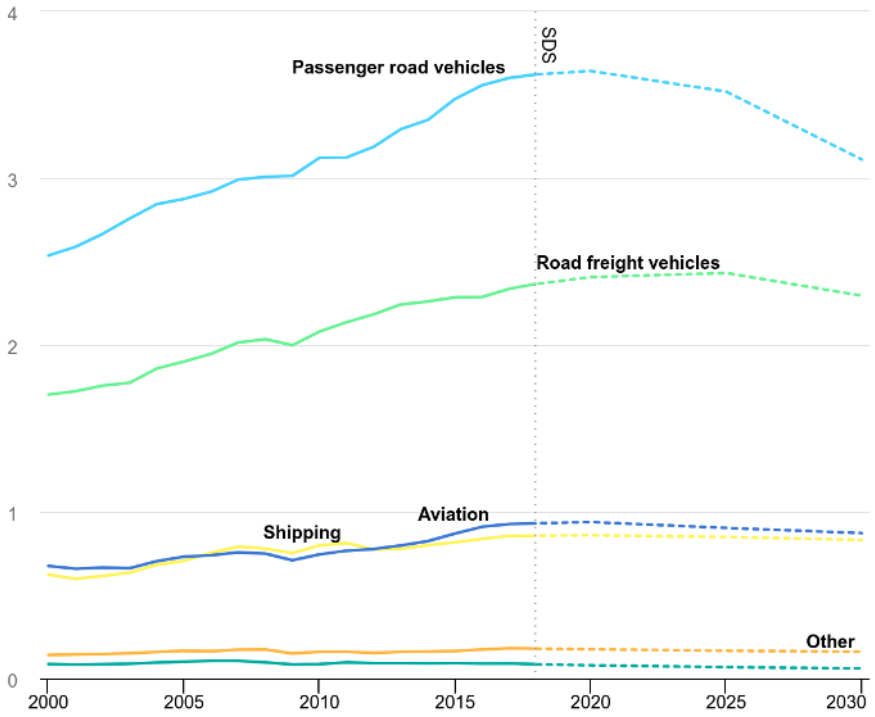

Figure 1.4. Transport sector CO_2 emissions by mode in the Sustainable Development Scenario (International Energy Agency, 2022)

Emissions from vehicles encompass a spectrum of pollutants, extending beyond CO_2 to include various harmful substances. While CO_2 remains a prominent concern due to its contribution to climate change, attention has increasingly turned towards other pollutants emitted by vehicles, such as nitrogen oxides (NO_x), particulate matter (PM), carbon monoxide (CO), hydrocarbon (HC), and volatile organic compounds (VOCs). These pollutants not only degrade air quality but also pose significant health risks to human populations, exacerbating respiratory illnesses and cardiovascular problems.

Nitrogen oxides are a family of highly reactive gases that form when nitrogen and oxygen react at high temperatures during combustion, such as in-vehicle engines or power plants. The primary constituents of NO_x are nitric oxide (NO) and nitrogen dioxide (NO_2), with NO_2 being particularly harmful due to its role in the formation of ground-level ozone and fine particulate matter ($PM_{2.5}$), both of which contribute to respiratory issues and cardiovascular problems. They not only contribute to air pollution but also play a role in the formation of smog and acid rain.

Carbon monoxide is a colorless, odorless gas produced by incomplete combustion of carbon-containing fuels in vehicles. It can interfere with the blood's ability to carry oxygen, leading to symptoms such as headaches, dizziness, and even death in high concentrations. Hydrocarbons, on the other hand, are compounds consisting entirely of carbon and hydrogen atoms, which are emitted as unburned fuel or by-products of combustion. They contribute to the formation of ground-level ozone and smog, as well as being linked to respiratory ailments and cancer.

Hydrocarbons, on the other hand, are compounds consisting entirely of carbon and hydrogen atoms, which are emitted as unburned fuel or by-products of combustion. They contribute to the formation of ground-level ozone and smog, as well as being linked to respiratory ailments and cancer.

Particulate matter refers to tiny particles suspended in the air, which can vary in size and composition. PM can be generated from natural sources such as dust and wildfires, as well as human activities like vehicle emissions and industrial processes. The size of PM is a critical factor in determining its potential health effects, with smaller particles (PM2.5 and PM10) being of particular concern due to their ability to penetrate deep into the lungs and enter the bloodstream. Exposure to PM is associated with a range of health problems, including respiratory issues, cardiovascular diseases, and even premature death. Moreover, PM can also contribute to visibility reduction and environmental damage.

Volatile organic compounds are a diverse group of carbon-based chemicals that can easily evaporate into the air. VOCs are emitted from sources such as vehicle exhaust, industrial processes, and the use of solvents and consumer products. These compounds can react with nitrogen oxides in the presence of sunlight to form ground-level ozone and smog, which can cause respiratory problems and exacerbate existing health conditions. Additionally, VOCs themselves can have adverse health effects, including eye, nose, and throat irritation, as well as being linked to long-term health issues such as cancer.

Addressing these emissions necessitates a comprehensive approach, including technological advancements in vehicle design, stricter emissions standards, and the promotion of cleaner fuels and alternative propulsion systems. Moreover, fostering public awareness and incentivizing the adoption of eco-friendly transportation practices are integral to mitigating the environmental impact of vehicular emissions beyond CO_2. By prioritizing these efforts, societies can strive toward a more sustainable and healthier future for both the planet and its inhabitants.

1.1. Emission Standards

The introduction of emission standards represents a pivotal moment in environmental regulation, shaping the trajectory of industrial and vehicular emissions worldwide. These standards serve as benchmarks, setting limits on the permissible levels of pollutants released into the atmosphere from various sources, including vehicles, power plants, and industrial facilities. Initially introduced in response to growing concerns over air quality and public health, emission standards have evolved over time to address emerging environmental challenges, such as climate change and urban pollution. By establishing clear guidelines and targets for pollutant reduction, emission standards incentivize the development and adoption of cleaner technologies and practices, driving innovation in engineering and industry. Moreover, they provide a framework for regulatory enforcement, ensuring accountability and compliance among stakeholders. Overall, the introduction of emission standards marks a crucial step towards achieving sustainable development goals and safeguarding the health and well-being of both present and future generations.

Emission standards vary around the world, but some common types include:

Euro Standards (European Union): Euro standards are used in Europe to regulate emissions from vehicles, including cars, trucks, and buses. These standards set limits on pollutants such as nitrogen oxides (NO_x), particulate matter (PM), and hydrocarbons (HC).

The Euro I to VII directives, instituted from the outset of the 1990s to the contemporary period, have cultivated a regional legal framework aimed at governing vehicular emissions, consequently emerging as foundational tenets within the domain of European environmental governance (Ballor, 2023). In Table 1.1, European emission standards are tabulated for comparison from Euro I to Euro VI.

In 2022, the European Commission, as the executive body of the European Union, put forth the most recent regulatory framework known as "Euro 7." Pending ultimate formal ratification from member states of the European Union, these novel regulations are slated to be enforced upon automobiles and vans commencing from July 2030, while their application to buses and trucks is scheduled to take effect twelve months thereafter (Reuters, 2024). In Table 1.2 Euro 7 tailpipe emission limits for passenger cars of category M_1 and light-duty vans of category N_1 are given. Also, Table 1.3 shows Euro 7 tailpipe emission limits compared to Euro 6 for heavy-duty vehicles falling into categories M_2, M_3, N_2, and N_3.

U.S. EPA Standards (United States): The Environmental Protection Agency (EPA) in the United States sets emission standards for various pollutants, including criteria pollutants like nitrogen dioxide (NO_2), sulfur dioxide (SO_2), carbon monoxide CO, lead, ozone (O_3), and PM. These standards apply to a wide range of sources, including vehicles, power plants, and industrial facilities. The regulations encompass all passenger vehicles, comprising light-duty vehicles (such as cars), light-duty trucks (like small pickup trucks), and medium-duty passenger vehicles (such as certain larger SUV configurations). Every vehicle, irrespective of its fuel type, falls under these standards.

Following the enactment of the Clean Air Act (CAA) in 1970, the Environmental Protection Agency (EPA) initiated the regulation of NO_x emissions from light-duty vehicles. Subsequent amendments to the CAA in 1990 introduced new emission standards for four additional smog pollutants: non-methane organic gases (NMOG), CO, PM, and formaldehyde (HCHO). These amendments also granted California the authority to implement its own more stringent vehicle emission standards, given its severe air pollution challenges. However, California's stricter standards require approval from the EPA through a waiver process. States have the option to adopt either the federal or California standards (Figure 1.5).

Table 1.1. European emission standards for heavy-duty diesel engines, g/kWh (Wikipedia, 2022)

Tier	Date	Test cycle	CO	HC[a]	NO_x	NH_3[b] [ppm]	PM	PN[c] [#/kWh]	Smoke [m^{-1}]
Euro I	1992, < 85 kW	ECE R49	4.5	1.1	8.0	-	0.612	-	-
	1992, > 85 kW		4.5	1.1	8.0	-	0.36	-	-
Euro II	October 1995		4.0	1.1	7.0	-	0.25	-	-
	October 1997		4.0	1.1	7.0	-	0.15	-	-
Euro III	October 1999 EEVs[d] only	ESC & ELR	1.5	0.25	2.0	-	0.02	-	0.15
	October 2000		2.1	0.66	5.0	-	0.10 0.13[f]	-	0.8
Euro IV	October 2005		1.5	0.46	3.5	-	0.02	-	0.5
Euro V	October 2008		1.5	0.46	2.0	-	0.02	-	0.5
Euro VI	31 December 2012	WHSC	1.5	0.13	0.4	10	0.01	8×10^{11}	-
		WHTC	4.0	0.16	0.46	10	0.01	6×10^{11}	-

Notes:
[a] In EURO VI, HC has been replaced by the measurement of "THC" – Total Hydrocarbons. HC and THC are not necessarily completely comparable values.
[b] EURO VI limits NH_3 measured in ppm/kWh, whereas EURO VII limits NH_3 measured in mg/kWh.
[c] In Euro VII, "PN" includes smaller particle sizes. The cut-off value is lowered from PN23 to PN10. This means that PN in EURO VII includes particulates down to 10 nm as opposed to only down to 23 nm in Euro VI.
[d] enhanced environmentally friendly vehicle.
[e] for engines of less than 0.75 liters swept volume per cylinder and a rated power speed of more than 3,000 per minute.

Table 1.2. Euro 7 tailpipe emission limits for passenger cars of category M_1 and light-duty vans of category N_1 (Dornoff and Rodríguez, 2024)

Category and Class	CO		THC		NMHC		NO_x		THC + NO_x		PM	PN_{10}
	SI	CI	SI	CI	SI	CI	SI	CI	SI	CI	SI & CI	SI & CI
M_1 & N_1 Class I	1000	500	100	-	68	-	60	80	-	170	4.5	$6x10^{11}$
N_1 Class II	1810	630	130	-	90	-	75	105	-	195	4.5	$6x10^{11}$
N_1 Class III	2270	740	160	-	108	-	82	125	-	215	4.5	$6x10^{11}$

Notes: SI: Spark ignition; CI: Compression ignition; CO: Carbon monoxide; THC: Total hydrocarbons; NMHC: Non-methane hydrocarbons; NO_x: Nitrogen oxides; PM: Particulate matter; PN_{10}: Number of particles larger than 10 nm

Table 1.3. Euro 7 tailpipe emission limits for heavy-duty vehicles of categories M_2, M_3, N_2, and N_3 (Dornoff and Rodríguez, 2024)

	WHSC (only CI engines)			WHTC (CI and SI engines)			On-road emissions limit		
	Euro VI (mg/kWh)	Euro 7 (mg/kWh)	Change compared to Euro VI	Euro VI (mg/kWh)	Euro 7 (mg/kWh)	Change compared to Euro VI	Euro VI (mg/kWh)	Euro 7 (mg/kWh)	Change compared to Euro VI
NO_x	400	200	-50%	460	200	-56%	690	260	-62%
PM	10	8	-20%	10	8	-20%	-	-	-
PN_{10}[a]	$6x10^{11}$	$6x10^{11}$	No change	$6x10^{11}$	$6x10^{11}$	No change	$9.8x10^{11}$	$9x10^{11}$	-8%
CO	1500	1500	No change	4000	1500	-62%	6000	1500	-68%
THC	130	-	-	160[b]	-	-	-	-	-
NH_3	-	60	New	-	60	New	-	85	New
CH_4	-	500	New	500[c]	500	No change	750	650	-13%
N_2O	-	200	New	-	200	New	-	260	New

Notes: WHSC: World Harmonized Stationary Cycle; WHTC: World Harmonized Transient Cycle; CI: Compression ignition; SI: Spark ignition;
[a] Particle number limit in #/kWh; [b] Only for diesel engines; [c] Only for gas engines.

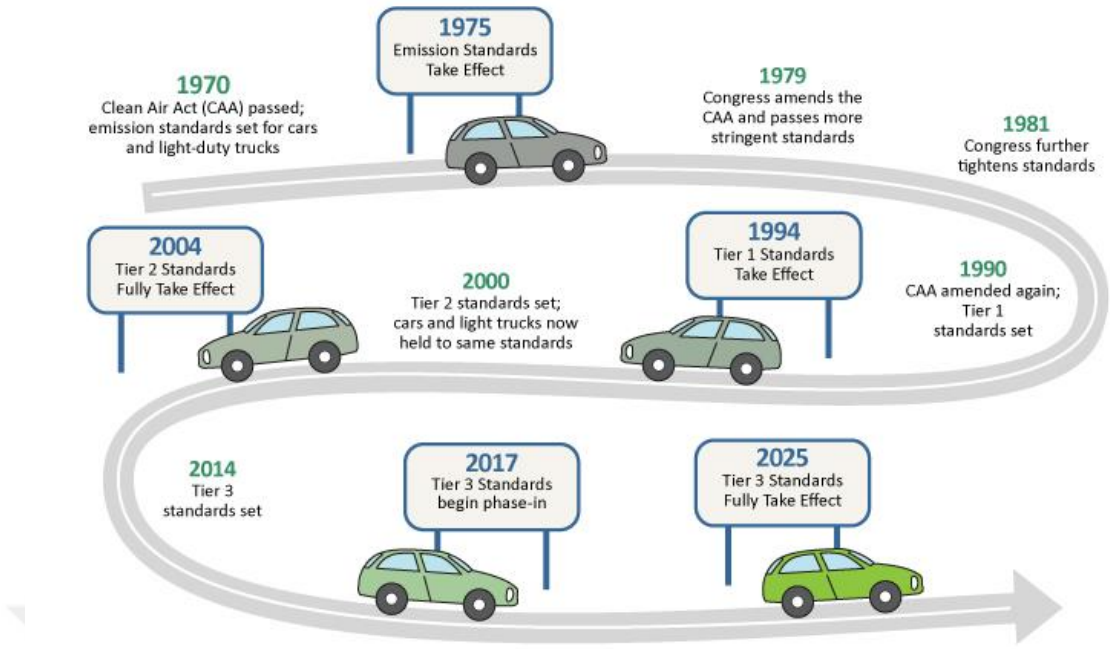

Figure 1.5. History of the U.S. Emission Standards (Environmental Protection Agency, 2024)

Over the years, smog pollution emission standards have undergone significant enhancement, resulting in markedly cleaner and healthier air. The NO_x emission standards set for light-duty vehicles in 2025 represent a remarkable 98% improvement compared to those established in 1975. These stringent standards have played a pivotal role in driving the enhancements observed in the air quality across the United States (Figure 1.6).

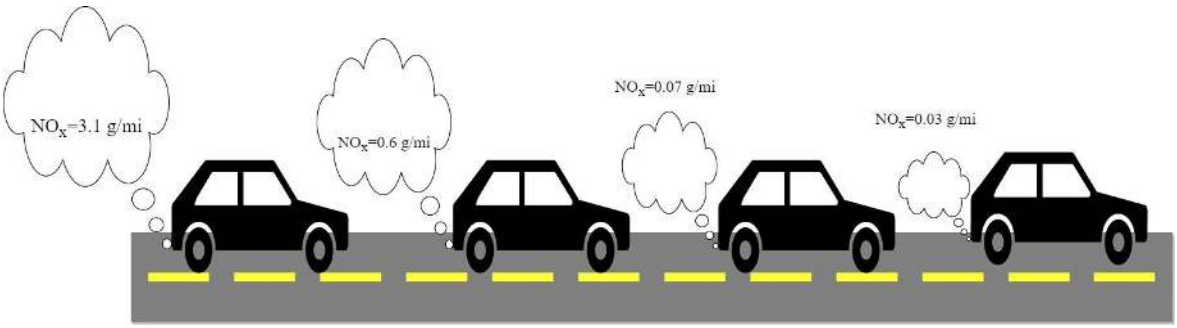

Figure 1.6. The progress in NO_x emissions from 1975 to 2025 (Environmental Protection Agency, 2024)

In Table 1.4 current emission standards for both Federal and California are given.

Table 1.4. Tier 3 (MY 2025+) and LEV III Program (MY 2015+) (Environmental Protection Agency, 2019)

Standards		Emission Limits (grams/miles) *				
Tier (Federal)	LEV[a] (California)	NO_x+NMOG[b]	CO	PM		$HCHO_c$
				Tier	LEV**	
Cars, Trucks, and SUVs						
Bin 1	N/A***	0	0	0	0	0
Bin 20	SULEV20	0.02	1	0.01	0.003	0.004
Bin 30	SULEV30	0.03	1	0.01	0.003	0.004
Bin 50	ULEV50	0.05	1.7	0.01	0.003	0.004
Bin 70	ULEV70	0.07	1.7	0.01	0.003	0.004
Bin 125	ULEV125	0.125	2.1	0.01	0.003	0.004
Bin 160	LEV160	0.16	4.2	0.01	0.003	0.004

Notes: * Maximum allowed grams of pollutant per mile at vehicle's full useful life (150,000 miles).
** Starting in 2017, LEV PM standards dropped to 0.003 g/mi, with 100% certified by 2021, and drop further starting in 2025.
*** ZEVs are handled differently under California's LEV program.
[a] Low-emission vehicle; [b] Non-methane organic gases; [c] Formaldehyde.

China Standards: China standards regulate emissions from vehicles and are designed to be in line with international standards. These standards set limits on pollutants such as NO_x, PM, and HC, with increasingly stringent requirements for newer vehicle models. The emission constraints outlined in China VI closely mirror those specified in Euro VI, as given in Table 1.5. When alongside the preceding China V standards, notable reductions of 77% and 67% are observed in NO_x and PM emissions, respectively, as assessed through transient cycles. Additionally, the China VI-a protocol encompasses a Particle Number (PN) restriction for Heavy-Duty Vehicles (HDVs), with thresholds set at 8.0×10^{11}#/kWh for steady-state cycle evaluations and 6.0×10^{11}#/kWh for transient cycle assessments. Compliance with the PN limitations necessitates the integration of a Diesel Particulate Filter (DPF) system into all newly manufactured diesel HDVs distributed within China (Table 1.6).

Table 1.5. Summarizes the China 6 limits for passenger cars and light-duty commercial vehicles (He and Yang, 2017)

Stage	Category	Class	CO	HC	NHMC	NO_x	N_2O	PM	PN[a]
			g/km						*#/kWh*
China 6a	Type 1		0.700	0.100	0.068	0.060	0.020	0.0045	$6x10^{11}$
	Type 2	I	0.700	0.100	0.068	0.060	0.020	0.0045	$6x10^{11}$
		II	0.880	0.130	0.090	0.075	0.025	0.0045	$6x10^{11}$
		III	1.000	0.160	0.108	0.082	0.030	0.0045	$6x10^{11}$
China 6b	Type 1		0.500	0.050	0.035	0.035	0.020	0.0030	$6x10^{11}$
	Type 2	I	0.500	0.050	0.035	0.035	0.020	0.0030	$6x10^{11}$
		II	0.630	0.065	0.045	0.045	0.025	0.0030	$6x10^{11}$
		III	0.740	0.080	0.055	0.050	0.030	0.0030	$6x10^{11}$

Notes: [a] Prior to July 1, 2020, a PN limit of $6x10^{12}$ to gasoline fueled vehicle.
Type 1: M_1 vehicles for no more than 6 passengers including driver, and GVW ≤ 2.5 ton,
Type 2: Other light-duty vehicles (including N_1 light commercial vehicles) further divided into three classes based on the reference mass (RM):
Class I: RM ≤ 1305 kg
Class II: 1305 kg < RM ≤ 1760 kg
Class III: RM > 1760 kg

Table 1.6. China VI emission standards for heavy-duty engines (Yang and He, 2018)

Stage	Test Cycle	CO	HC	NMHC	CH_4	NO_x	PM	PN	NH_3
		mg/kWh						*kWh^{-1}*	*ppm*
China VI CI	WHSC	1500	130	-	-	400	10	$8.0x10^{11}$	10
	WHTC	4000	160	-	-	460	10	$6.0x10^{11}$	10
	WNTE	2000	220	-	-	600	16	-	-
China VI PI	WHTC	4000	-	100	500	460	10	$6.0x10^{11}$	10
	WNTE	2000	220	-	-	600	10	-	-

Notes: WHSC: World Harmonized Stationary Cycle; WHTC: World Harmonized Transient Cycle; WNTE: World-harmonized Not-to-Exceed

India Bharat Stage Emission Standards (BSES): Bharat Stage emission standards are used in India to regulate vehicle emissions. Similar to Euro standards, they set limits on pollutants such as NO_x, PM, and HC, with progressively stricter standards being implemented over time. The limits are tabulated in Table 1.7.

Table 1.7. Pollutant emission limits for BSES standards based on certification tests (Gajbhiye et al., 2023)

BS Standards	Regulatory test	*Pollutant emissions limits (g/kWh)*			
		CO	HC	NO_x	PM
BS-VI	WHSC (CI)	1.50	0.13	0.40	0.01
	WHTC (CI)	4.00	0.16	0.46	0.01
	WHSC (PI)	4.00	0.16	0.46	0.01

Japan's New Long-term Emission Regulations: Japan's emission regulations, often referred to as "Long-term Regulations," aim to reduce emissions from vehicles and engines over an extended period. These regulations set limits on pollutants such as NO_x, PM, and HC, with a focus on improving air quality and public health. Tables 1.8 and 1.9 show the emission standards for light and heavy-duty vehicles, respectively.

Table 1.8. Japanese Emission Standards for Diesel Passenger Cars and Light Commercial Vehicles g/km (*Japan: Light-Duty: Emissions*, 2024)

Curb Weight	Date	Test	CO	HC	NO_x	PM
Passenger Cars						
≤ 1250 kg*	2009	JC08[a]	0.63	0.024[b]	0.08	0.005
> 1250 kg*	2009[c]	JC08[a]	0.63	0.024[b]	0.08	0.005
Light Commercial Vehicles						
≤ 1700 kg	2009	JC08[a]	0.63	0.024[b]	0.08	0.005
> 1700 kg	2009[c]	JC08[a]	0.63	0.024[b]	0.15	0.007

Notes: * equivalent inertia weight (EIW); vehicle weight of 1265 kg
[a] full phase-in by 2011
[b] non-methane hydrocarbons
[c] 2009.10 for new domestic models; 2010.09 for existing models & imports

Table 1.9. Diesel Emission Standards for Heavy-duty Commercial Vehicles (GVW>3500 kg) (*Japan: Heavy-Duty: Emissions*, 2024)

Date	Test	Unit	CO	HC	NO_x	PM
2016	WHTC	g/kWh	2.22	0.17[a]	0.4[b]	0.01

Notes: GVW: gross vehicle weight
[a] non-methane hydrocarbons
[b] enforcement: 2016 for GVW>7.5t; 2017 for tractors; 2018 for 3.5t < GVW ≤ 7.5t

These are just a few examples, and many other countries and regions have their own emission standards tailored to their specific environmental and regulatory needs. However, there is an increasing trend towards harmonizing standards globally to address transboundary pollution and mitigate climate change effectively.

1.2. Diesel Engines

Diesel engines operate by compressing air to a high temperature, which ignites the fuel injected into the combustion chamber. This process is efficient and provides high torque, making diesel engines popular in various applications. The combustion process in diesel engines is highly complex, and until the 1990s, its underlying mechanisms were not fully understood. Despite the availability of advanced tools, such as high-speed photography in "transparent" engines, the computational power of modern computers, and various mathematical models designed to simulate diesel combustion, researchers faced significant challenges in unraveling its intricacies. For decades, these complexities posed a substantial obstacle to comprehensive understanding. However, the introduction of laser-sheet imaging technology in the 1990s marked a pivotal advancement, significantly enhancing the scientific understanding of conventional diesel combustion processes (Majewski and Jääskeläinen, 2023).

The fundamental principle of diesel combustion lies in its distinctive method of releasing the chemical energy stored within the fuel. For this process to occur, oxygen (O_2) must be supplied to the fuel in a precise manner to enable effective combustion. A critical aspect of this process is the fuel-air mixing, commonly referred to as mixture preparation, which plays a pivotal role in determining the efficiency and completeness of the combustion reaction (Majewski and Jääskeläinen, 2023).

In diesel engines, fuel injection typically occurs near the end of the compression stroke, just a few crank angle degrees (CAD) before the top dead center (BTDC) (Heywood, 2018). The liquid fuel is injected at high velocity through one or more jets via small orifices or nozzles located at the injector tip. Upon injection, the fuel undergoes atomization, breaking into small droplets as it penetrates the combustion chamber. The atomized fuel absorbs heat from the surrounding compressed air, vaporizes, and subsequently mixes with the high-temperature, high-pressure air. As the piston approaches the top dead center (TDC), the mixture-composed predominantly of air—reaches the ignition temperature of the fuel. Following a brief ignition delay (ID) period, rapid ignition of the premixed fuel and air occurs, marking the onset of combustion. This is indicated by a

sharp increase in cylinder pressure as the fuel-air mixture combusts. The pressure rise from this premixed combustion further compresses and heats the remaining unburned charge, thereby reducing the ignition delay of the subsequent mixture and accelerating the evaporation of the remaining fuel. The processes of atomization, vaporization, fuel-air mixing, and combustion continue until all the injected fuel is fully combusted (Majewski and Jääskeläinen, 2023).

Without delving into the specifics of the combustion process, a simplified expression for mass conservation can be formulated by considering the interaction of reactant species such as fuel ($C_xH_yO_z$) and air (primarily nitrogen, N_2, and oxygen). In the appropriate conditions, these reactants undergo a chemical reaction, producing various exhaust components, which can be represented as follows:

$$C_xH_yO_z + aO_2 + 3.76aN_2 \rightarrow bCO_2 + dH_2O + eOH_2 + fH_2 + g(HC) + hNO + iHCHO + jNH_3 + kN_2 + pO_2 \quad (1.1)$$

The left-hand side of Equation (1.1) represents the reaction of a hydrocarbon fuel ($C_xH_yO_z$) with air, which consists of 20.99% oxygen and 79.01% nitrogen by volume. For hydrocarbon (HC) fuels, where (z=0), the primary exhaust products are carbon dioxide (CO_2), water (H_2O), and nitrogen (N_2), along with excess oxygen (O_2) in the case of lean-burn engines. These major species typically account for over 99% of the exhaust gases, with less than 1% comprising other, predominantly undesirable, emission species (Majewski and Jääskeläinen, 2023).

Diesel engines typically operate at higher temperatures compared to gasoline engines. The high temperatures contribute to the formation of NO, as nitrogen in the air reacts with oxygen during combustion (Figure 1.7). Thus, diesel exhaust becomes the primary and most fundamental source of NO_x emission as the increasing number of diesel engines which are more powerful and fuel-efficient than similar-sized gasoline engines. Although NO_x emissions are the most critical emissions that need to be reduced, emission control methods in vehicles equipped with this engine are of great importance. The primary systems for this purpose are as follows; diesel oxidation catalyst, diesel particulate filter, exhaust gas recirculation, lean NO_x trap, and selective catalytic reduction.

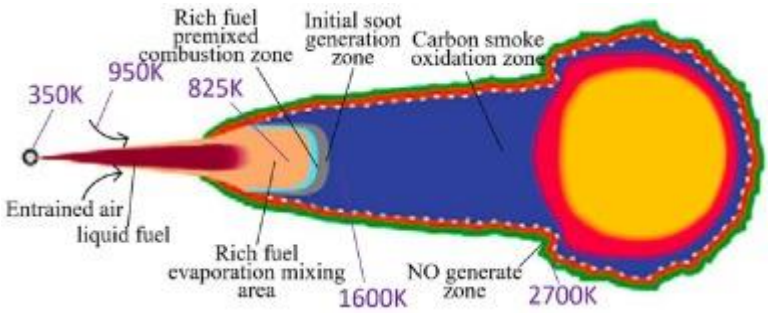

Figure 1.7. Conceptual model of the mixing-controlled burn phase (Dec, 1997)

1.3. Diesel Vehicle Aftertreatment Systems

Table 1.10 represents the evolution of after-treatment systems for diesel engines under various emission regulations, starting from Euro 4 to Post Euro 6. Each level introduces more advanced components to meet increasingly stringent emission standards. Euro 4 relies on diesel oxidation catalyst (DOC) to reduce CO and HC emissions. Euro 5 adds a catalyzed soot filter (CSF) for particulate matter (PM) reduction. For Euro 6b, systems incorporate lean NO_x traps (LNT) and advanced selective catalytic reduction filter (SCRF) to control NO_x and PM emissions, with an ammonia slip catalyst (ASC) to prevent excess ammonia release. Euro 6d enhances these systems further with real driving emissions (RDE) testing capabilities, while Post Euro 6 configurations include electric heated catalysts (EHC) for improved performance during cold starts and low-temperature operations. This progression highlights the increasing complexity and efficiency of emission control systems to comply with stricter environmental regulations (Selleri et al., 2021).

Table 1.10. Evolution and newly proposed after-treatment system configurations for Diesel light-duty vehicles (Selleri et al., 2021)

Regulation	After-treatment system
Euro 4	
Euro 5	
Euro 6b CN 6a BS 6	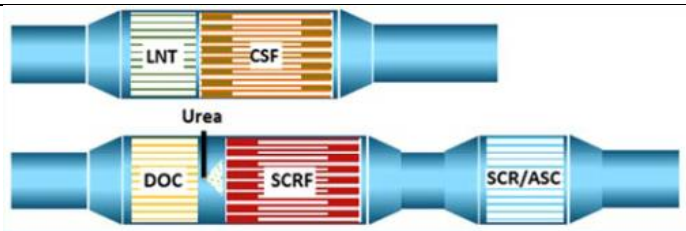
Euro 6d CN 6b BS 6 w/RDE	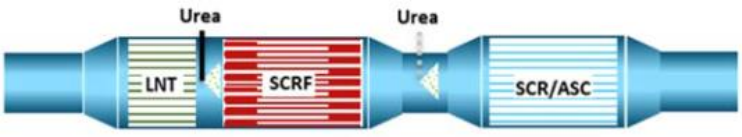
Post Euro 6	

Table 1.11 shows the evolution of after-treatment systems designed for HDV, from Euro IV to post-Euro VI. While Euro IV and Euro V systems rely on a basic SCR unit with urea injection to

reduce NO_x emissions, Euro VI introduces more advanced configurations, including a DOC for CO and HC oxidation, a DPF for PM reduction, and an ASC to prevent excess ammonia emissions. Post Euro VI systems further enhance these technologies by incorporating Close-Coupled DOC (cc-DOC) and selective catalytic reduction (cc-SCR) for improved low-temperature performance and cold-start efficiency, as well as SCR-on-DPF (diesel particulate filter) technology to reduce both PM and NO_x in a single unit. This progression reflects the increasing complexity of exhaust after-treatment systems aimed at addressing a broader range of pollutants under diverse operating conditions (Selleri et al., 2021).

Table 1.11. Evolution and newly proposed after-treatment system configurations for Diesel heavy-duty vehicles (Selleri et al., 2021)

Regulation	**After-treatment system**
Euro 4 Euro 5	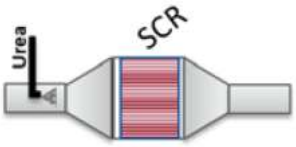
Euro 6	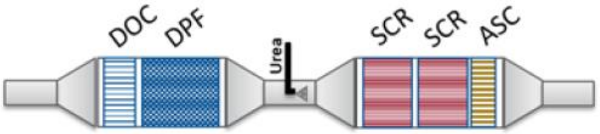
Post Euro 6	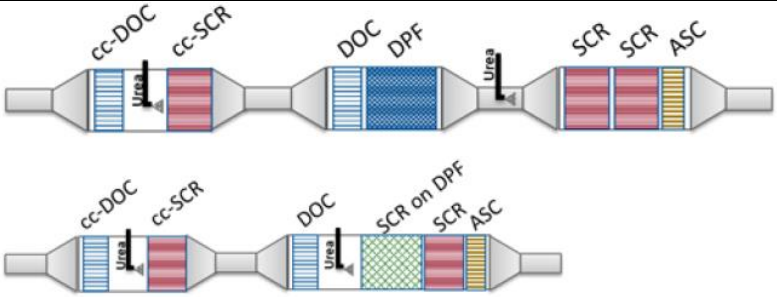

1.3.1. Diesel Oxidation Catalyst (DOC)

The primary function of a diesel oxidation catalyst (DOC) is to oxidize CO, HC, and unburned fuel into less harmful gases, such as CO_2 and H_2O. It also plays a role in converting some NO_x into N_2, though its efficiency in this regard is limited.

The DOC typically works as part of a broader after-treatment system, which may include components like the Diesel Particulate Filter (DPF) and Selective Catalytic Reduction (SCR) system, to further reduce PM and NO_x emissions. By doing so, the DOC helps vehicles comply with stringent emissions regulations and contributes to cleaner exhaust outputs.

1.3.2. Diesel Particulate Filter (DPF)

A DPF is an emissions control device designed to capture and remove PM, or soot, from the exhaust gases before they are released into the atmosphere. These particles are primarily composed of carbon and other harmful substances produced during the combustion of diesel fuel.

The DPF works by trapping the particulate matter within a filter structure that allows the exhaust gases to pass through while collecting the solid particles. Over time, the filter accumulates soot, and in order to maintain its efficiency, the DPF periodically undergoes a process called regeneration. During regeneration, the trapped soot is burned off at high temperatures, converting it into CO_2, which can then be safely emitted.

There are two main types of regeneration processes:

Passive regeneration: Occurs naturally during normal driving conditions when the exhaust temperature is high enough to oxidize the trapped particles.

Active regeneration: Initiated by the vehicle's engine control system when passive regeneration is insufficient, typically by increasing the exhaust temperature through post-injection of fuel or other means.

1.3.3. Exhaust Gas Recirculation (EGR)

It is an emissions control technology used to reduce the formation of NO_x, which are harmful pollutant produced during the combustion process, especially at high temperatures.

The EGR system works by recirculating a portion of the exhaust gases back into the engine's intake manifold, where they are mixed with fresh air and fuel. By reintroducing exhaust gases into the combustion chamber, the following effects occur:

Lowering Combustion Temperature: The inert gases from the exhaust (mainly nitrogen and carbon dioxide) do not combust, so they absorb heat without contributing to combustion. This reduces the peak combustion temperature, which is one of the key factors in NO_x formation.

Reducing Oxygen Availability: The re-circulated exhaust gases also dilute the oxygen concentration in the intake air, further suppressing NOx formation.

There are two main types of EGR systems in diesel engines:

High-pressure EGR: Takes exhaust gases before they pass through the turbocharger and reintroduces them into the intake manifold.

Low-pressure EGR: Extracts exhaust gases after they have passed through the particulate filter, allowing cleaner exhaust gases to be recirculated.

The EGR system plays a crucial role in enabling diesel engines to meet strict emissions standards by reducing NO_x emissions, but it can also lead to issues like increased soot production and carbon buildup within the intake system if not properly maintained. A schematic representation is given in Figure 1.8.

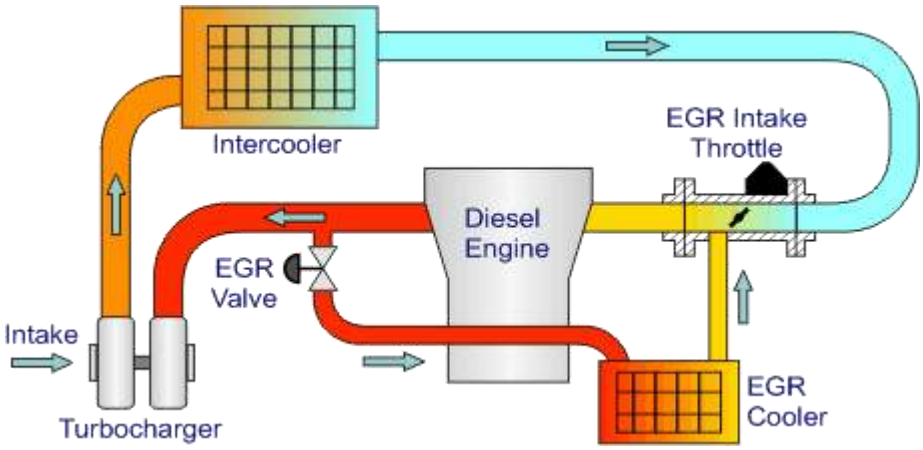

Figure 1.8. Schematic diagram of an EGR

1.3.4. Lean NO_x Trap (LNT)

In a diesel engine-equipped vehicle, LNT stands for Lean NO_x Trap (also known as a NO_x adsorber). It is an emissions control technology designed to reduce NO_x emissions, particularly in lean-burn engines, such as diesel engines, where the air-fuel mixture contains excess oxygen.

The LNT works by trapping NO_x emissions in the exhaust during lean (oxygen-rich) operating conditions and then converting them into less harmful substances, primarily N_2 and H_2O, during a regeneration phase. The process happens in two key stages:

NO_x Trapping (Lean Conditions): Under normal lean operation, the LNT adsorbs and stores NO_x on the catalyst surface, typically using materials such as barium or potassium. These materials react with NO_x to form nitrates, which are stored in the trap.

NO_x Reduction (Rich Conditions): When the trap becomes saturated with NO_x, the engine control system briefly adjusts the air-fuel ratio to create a rich (fuel-rich) condition, reducing the amount of oxygen in the exhaust. During this phase, a small amount of fuel is injected to help convert the stored NO_x into harmless N_2 and H_2O. This process is known as *regeneration*.

The Lean NO_x Trap is especially useful for reducing NO_x emissions in light-duty diesel vehicles, where SCR systems may be less practical due to size, cost, or operational constraints. However, LNT systems can be less efficient in heavy-duty applications, and their performance can be sensitive to factors like sulfur in the fuel, which can poison the trap. Regular regeneration is also needed to maintain effectiveness.

1.3.5. Selective Catalytic Reduction (SCR)

Selective catalytic reduction is an advanced emissions control technology used to reduce NO_x, which is a significant pollutant produced during combustion, especially in diesel engines. SCR works by injecting a liquid reductant, commonly a urea-based solution known as diesel exhaust fluid (DEF) or AdBlue, into the exhaust stream before the gases pass through a catalyst. A schematic illustration is given in Figure 1.9.

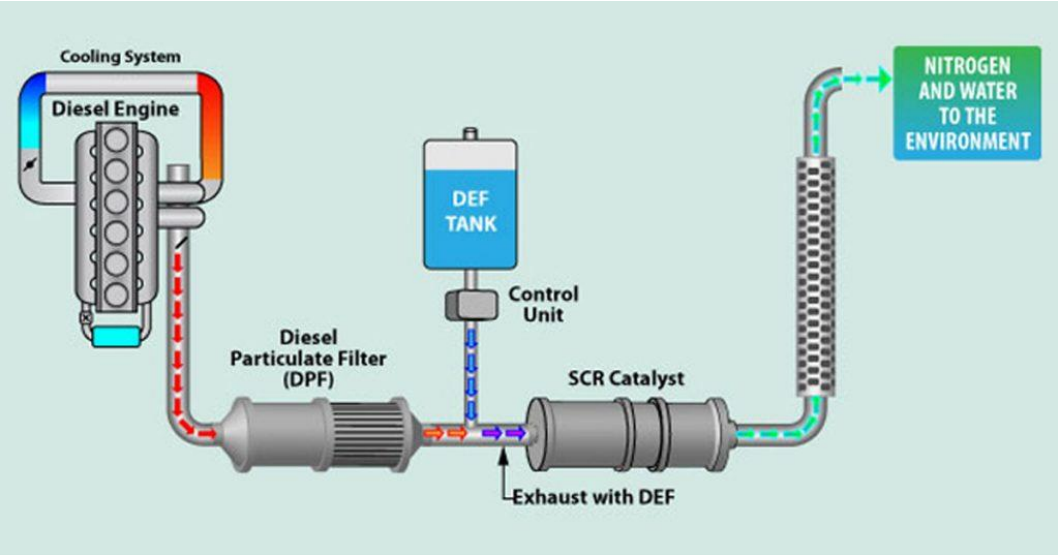

Figure 1.9. Schematic diagram of basic SCR system (Stephens, 2020)

The SCR system operates as follows:

Injection of DEF: The DEF is injected into the hot exhaust gases, where it decomposes into ammonia (NH_3) and CO_2. This ammonia then acts as the key reductant that reacts with NO_x.

NO_x Reduction: As the exhaust gases, along with the ammonia, pass over the catalyst (typically made of materials like vanadium, titanium, or zeolites), a chemical reaction occurs that converts harmful NO_x into harmless N_2 and H_2O. This reaction is highly selective and efficient, hence the name Selective Catalytic Reduction.

Catalyst Function: The catalyst facilitates the reaction without being consumed, allowing it to continuously aid in the conversion of NO_x to nitrogen and water.

SCR systems are highly effective in reducing NO_x emissions, with reduction efficiencies often exceeding 90%. This makes them critical in helping diesel vehicles meet stringent emissions regulations, such as Euro 6 in Europe or Tier 4 in the U.S. SCR systems are particularly suited for heavy-duty applications, such as trucks, buses, and large industrial equipment, where high NO_x emissions are a concern.

The SCR system requires careful monitoring of DEF levels to ensure proper operation. If the DEF supply is depleted or the system malfunctions, the engine may operate with reduced power or enter a "limp mode" to prevent excessive NO_x emissions. Additionally, SCR systems are often integrated with other after-treatment devices, such as DPF and DOC, to further reduce other pollutants like PM and HC.

The literature survey on SCR systems encompasses a comprehensive analysis of catalyst materials, their physical and chemical characterization, and subsequent performance evaluations. Extensive research has been conducted on various catalyst types, focusing particularly on the conditions under which these catalysts achieve optimal efficiency and activity. While the inclusion of Sm as a catalytic component has garnered attention in recent years, its application remains highly

limited. To date, there appear to be no reported studies in the literature investigating the combination of Sm, Cu, and zeolites with different reductants, highlighting a significant gap that warrants further exploration.

Although numerous studies have systematically examined the effects of varying Cu ratios as an active material in SCR catalysts, the same level of investigation has not been applied to Sm. Addressing this gap, the present study focuses on keeping the Cu ratio constant while introducing Sm at varying concentrations. Two distinct sets of catalysts were prepared, utilizing Y and BEA zeolites as carriers. This two carrier approach aims to evaluate the influence of zeolite type on the catalytic performance of Sm-modified systems.

The lack of information on the optimal proportions of Sm usage in the literature, along with the unknown effects of the synergistic use of Sm-Cu and ethanol as a reducing agent on NOx emissions, can be identified as another gap in the research. Thus, ethanol was chosen as the reductant for this study due to its notable potential, as reported in prior studies, and its advantageous properties such as ease of blending with diesel fuel under standard operating conditions. Additionally, the use of ethanol offers a practical alternative to commercially utilized AdBlue, addressing several associated disadvantages such as freezing issues and storage challenges. By integrating ethanol into the SCR process, the study aims to leverage its favorable chemical properties while investigating its compatibility with Sm-Cu-zeolite catalysts.

This research is expected to provide valuable insights into the performance of Sm-modified SCR catalysts, particularly in the context of varying Sm ratios and carrier types, while also exploring the feasibility of ethanol as a reductant. The findings will contribute to bridging the identified gap in the literature and advancing the development of efficient and sustainable SCR systems.

2. PRELIMINARY WORK

A review of the literature reveals that SCR systems can be designed in a wide variety of configurations. Comprising two main components, a reductant, and a catalyst, these systems are highly adaptable for use with diverse combinations of reductant types and catalyst materials.

Today, AdBlue which is a 32.5% solution of urea in de-mineralized water, commonly used as a commercial reductant, stands out as the most frequently encountered reductant (Ström et al., 2018; W. Wang et al., 2015). Despite its widespread use, it leads to various issues, including catalyst degradation, ammonia slip, and ash-related odors (Costa et al., 2007; Valanidou et al., 2011). Therefore, studies on new reductants that can be used as alternatives are also encountered in the literature. Examples of these reductants include CO, hydrogen (H_2), HC, or oxygenated hydrocarbons (OHC) (K. Liu et al., 2018).

In SCR systems, various materials are used as catalyst supports to enhance their performance while enhancing specific surface area. Commonly employed supports include cordierite ($2Al_2O_3.5SiO_2.2MgO$), a ceramic material known for its thermal stability and mechanical strength, and alumina (Al_2O_3), valued for its high surface area, providing an excellent foundation for active catalytic components. Silica (SiO_2) is often combined with alumina to improve thermal resistance and catalytic activity, while titania (TiO_2) is preferred for supporting vanadium-based catalysts due to its resistance to sulfur poisoning. Zeolites, with their microporous crystalline structure and high ion-exchange capacity, are frequently used in ammonia-SCR reactions. Additionally, stainless steel substrates are employed for their durability and thermal conductivity, especially in high-temperature applications. These catalyst supports are selected based on the specific operating conditions and performance requirements of the SCR system.

2.1. Ammonia SCR

NO_x emissions result from the high operating temperature caused by the high working pressure of the diesel engine. Normally, N_2 does not react with O_2 but at high temperatures, above 1600 °C, NO_x form becomes due to the combination of N_2 and O_2 (Zeldovich mechanism) (Mehregan and Moghiman, 2020). Zeldovich equations are given in the following equations (Bowman, 1975).

$$O + N_2 \leftrightarrow NO + N \tag{2.1}$$

$$N + O_2 \leftrightarrow NO + O \tag{2.2}$$

$$N + OH \leftrightarrow NO + H \tag{2.3}$$

$$NO + HO_2 \leftrightarrow NO_2 + H_2 \quad (2.4)$$

$$NO_2 + O \leftrightarrow NO + O_2 \quad (2.5)$$

Ammonia or NH_3-SCR systems that have commercial acceptance globally use urea solution (67.5% pure H_2O and 32.5% urea ($(NH_2)_2CO$) or ammonia (NH_3) as a reductant (Held et al., 1990). The use of urea solution is more common due to the toxic and volatile properties of ammonia (F. Liu et al., 2019). When a solution is sprayed into the exhaust gas, the evaporation of pure water leads to the melting of solid urea particles, initiating the thermolysis process, as represented in Equation (2.6).

$$(NH_2)_2CO \rightarrow NH_3 + HNCO\ (thermolysis) \quad (2.6)$$

During the thermolysis reaction, NH_3 and isocyanic acid are formed. NH_3 participates in the reactions occurring within the SCR catalyst, while isocyanic acid undergoes a hydrolysis reaction with water, resulting in the additional production of NH_3 (Reşitoğlu et al., 2015; Vignesh and Ashok, 2020).

$$HNCO + H_2O \rightarrow NH_3 + CO_2\ (hydrolysis) \quad (2.7)$$

Major constituents of NO_x are NO and NO_2 in proportions of about 90% and 10% respectively. And, the chemical reactions of the de-NO_x process in the presence of NH_3 are given as follows: The reduction of NO to N_2 is termed a slow reaction, and NO_2 to N_2 is termed a fast reaction (Mohan et al., 2020). The standard SCR reduction is shown in Equation (2.8) where the reduction of NO to N_2 proceeds. Due to the presence of DOC upstream of the SCR catalyst, the oxidation of NO to NO_2 would have been formed. This leads to a faster reaction as shown in Equation (2.9) where moles of NO equal to NO_2 participate in the reduction. However, in leaner conditions (O_2/NO_2=0), a much slower reaction as shown in Equation (2.10) has proceeded (Guan et al., 2014).

$$4NH_3 + 4NO + O_2 \rightarrow 4N_2 + 6H_2O\ (standard\ reaction) \quad (2.8)$$

$$4NH_3 + 2NO + 2NO_2 \rightarrow 4N_2 + 6H_2O\ (fast\ reaction) \quad (2.9)$$

$$8NH_3 + 6NO_2 \rightarrow 7N_2 + 12H_2O\ (slow\ reaction) \quad (2.10)$$

Table 2.1 provides an overview of previous studies focused on Cu-based zeolite catalysts used in NH_3-SCR applications.

Wilken et al. (2013) examined the effects of accelerated hydrothermal aging on the Cu-BEA catalyst for NH_3-SCR applications. They found that the hydrothermal treatment at temperatures above 800°C caused significant structural collapse of the Beta zeolite framework, as confirmed by XRD and BET measurements. Catalytic tests revealed that the NO_x conversion efficiency dropped substantially after aging at these high temperatures, correlating with the observed structural damage and the formation of CuO. The study highlighted that while the catalyst remained stable up to 700°C, hydrothermal aging above this threshold led to irreversible deactivation due to zeolite degradation and migration of copper species out of the zeolite framework. These findings underscore the critical role of hydrothermal stability in maintaining long-term SCR catalyst performance.

Zhu et al. (2020) explored the effects of NO_2 on the NH_3-SCR performance of two small-pore zeolite catalysts, Cu-SSZ-13 and Cu-SSZ-39, under standard and fast SCR conditions. The study found that while NO_2 inhibited NO_x conversion on Cu-SSZ-13 at lower temperatures due to NH_4NO_3 accumulation and pore-plugging, it promoted NO_x conversion on Cu-SSZ-39 by enhancing the reactivity of NH_4NO_3 with NO. Under standard SCR conditions, both catalysts demonstrated high NO_x conversion at elevated temperatures, with Cu-SSZ-39 outperforming Cu-SSZ-13 in fast SCR due to its higher surface acidity and efficient NH_4NO_3 reduction. The catalysts were tested with 500 ppm NO_x, 500 ppm NH_3, 5% O_2, and GHSV of 400000 h^{-1}, revealing distinct mechanistic behaviors influenced by the catalysts' structural and acidic properties. These findings emphasize the role of zeolite structure and surface acidity in optimizing NH_3-SCR activity for diesel engine NO_x abatement.

Y. Cao et al. (2016) investigated the effect of yttrium (Y) addition on Cu-SAPO-34 catalysts for the SCR of NO_x using NH_3. They found that the CuY-SAPO-34 catalyst exhibited a broader temperature range of 80% NO_x conversion (167-454 °C) compared to the Cu-SAPO-34 catalyst (179-393 °C) under conditions of 350 ppm NO, 350 ppm NH_3, 8% O_2, 5 vol% H_2O, and GHSV of 30000 h^{-1}. The introduction of Y improved the dispersion of copper species, increased the density of acid sites, and enhanced HC resistance by reducing the deposition of coke. These findings demonstrate the potential of Y-doped Cu-SAPO-34 as a promising catalyst for NH_3-SCR, particularly in HC-rich environments.

Fu et al. (2021) studied the hydrothermal stability and NH_3-SCR activity of Cu/SSZ-39 catalysts, revealing a significant dependency of stability and catalytic performance on Cu content. Their findings showed that higher Cu contents, particularly with more isolated Cu^{2+} ions, enhanced NO_x conversion rates and structural stability under hydrothermal conditions at 750–800°C. Under standard SCR conditions (500 ppm NO, 500 ppm NH_3, 5% O_2, 5% H_2O, and GHSV of 19000 h^{-1}), NO_x conversion rates exceeded 90% in the temperature range of 150–550°C, with a peak N_2 selectivity of 98% at optimal conditions. The study identified mutual protective effects between Cu^{2+} ions and framework Al atoms, where Cu ions shielded Al from hydrothermal damage, and Al sites stabilized Cu species. Additionally, they proposed a mixed Langmuir-Hinshelwood (L-H) and Eley-

Rideal (E-R) mechanism for SCR reactions, with NH_4NO_3 and NH_4NO_2 as key intermediates, highlighting the potential of Cu/SSZ-39 as a robust SCR catalyst for NO_x abatement.

Lin et al. (2018) conduct research to investigate the effects of hydrothermal deactivation on CuFe/BEA catalysts used for NH_3-SCR under various conditions. They found that fresh CuFe/BEA achieved over 90% NO_x conversion between 212 °C and 550 °C under test conditions of 200 ppm NO, 200 ppm NH_3, 10 vol.% O_2, 5 vol.% H_2O, with a GHSV of 40000 h^{-1}. However, after hydrothermal treatment at 700 °C for 10 hours, the NOx conversion of CuFe/BEA-HT significantly decreased to a maximum of 79%. The study revealed that hydrothermal treatment damaged the BEA zeolite structure, leading to the loss of Brønsted acid sites and aggregation of isolated Cu/Fe species into larger oxides. This structural degradation reduced the catalyst's redox properties and its ability to adsorb and activate reactant molecules, negatively impacting low-temperature NO_x conversion. The findings highlight the importance of preserving structural integrity and acid site density for maintaining high NH_3-SCR activity.

Ming et al. (2019) examined the chemical deactivation of Cu-SAPO-18 catalysts for NH_3-SCR caused by basic inorganic contaminants such as K, Na, Ca, and Mg, which are common in diesel exhaust. They found that these contaminants reduced the catalytic activity by decreasing the acidic sites and isolated Cu^{2+} species. Contaminants were introduced via wet impregnation, and the extent of deactivation increased with higher contaminant concentrations (0.5 to 1.0 mmol/g_{catal}). Specifically, Cu^{2+} ions were replaced by contaminant ions, leading to the formation of CuO and $CuAl_2O_4$ species, which caused pore blockage and structural damage. The NH3-SCR activity of contaminated Cu-SAPO-18 dropped significantly, with the deactivation effect following the order K>Na>Ca>Mg. Kinetic analyses showed that the contaminants had minimal impact on the reaction mechanism, but the reduction in acidic sites played a dominant role in the decline of catalytic performance. These findings underscore the importance of improving catalyst resistance to contaminants for practical diesel exhaust applications.

H. Wang et al. (2019) examined the effects of zeolite topology on the SCR performance and stability of Cu-zeolite catalysts for NH_3-SCR. They observed that catalysts with cage-type structures (e.g., Cu-SSZ-13) exhibited superior NH_3-SCR activity compared to straight-channel zeolites (e.g., ZSM-5, Beta, Y) and hybrid-structure zeolites (e.g., ZSM-34). Under test conditions of 1000 ppm NO, 1000 ppm NH_3, 6 vol% O_2, 5 vol% H_2O, and GHSV of 300000 h^{-1}, Cu-SSZ-13 achieved high NO_x conversion across a broad temperature range. Cage-type zeolites demonstrated enhanced stability and prevented dealumination, owing to their small cage apertures (~3.8 Å). The findings underscore the critical role of zeolite structure in determining the distribution and reducibility of Cu species, with isolated Cu ions in cage-type zeolites providing optimal SCR activity and N_2 selectivity.

Yue et al. (2019) developed a novel one-pot synthesis method to create hierarchical FeCu-ZSM-5 zeolite, which exhibits superior catalytic performance for the SCR of NO_x with NH_3. The synthesized catalyst features a unique micro-mesoporous structure, increased amounts of isolated

Cu^{2+} species, and Fe^{3+} incorporated into the zeolite framework. Compared to reference catalysts prepared through traditional impregnation methods, FeCu-ZSM-5 achieved high NOx conversion (>90%) and nearly 100% N_2 selectivity across a broad temperature range (230-500°C). Additionally, the catalyst demonstrated exceptional hydrothermal stability and SO_2 tolerance under harsh conditions, making it a promising candidate for practical NO_x abatement applications. This study emphasizes the synergistic effects of iron and copper species and the role of hierarchical structures in enhancing SCR performance.

Dou et al. (2015) investigated the SCR of NO_x using NH_3 over cerium-doped Cu/ZSM-5 catalysts. They demonstrated that the incorporation of cerium significantly enhanced the redox properties and catalytic activity of the Cu/ZSM-5 catalyst. Among the tested samples, the CuCe4-Z catalyst achieved 95% NO_x conversion within a temperature range of 148–427 °C under test conditions of 1000 ppm NO, 1000 ppm NH_3, 10% O_2, and GHSV = 15000 h^{-1}. Cerium doping increased the dispersion of copper species, prevented their crystallization, and enriched copper on the zeolite surface, as confirmed by XPS and H_2-TPR analyses. These findings highlight the potential of CuCe/ZSM-5 catalysts for efficient NO_x removal over a wide temperature range.

J. Wang et al. (2021) investigated the influence of niobium (Nb) addition on the low-temperature NH_3-SCR performance of Al-rich Cu-SSZ-13 catalysts. Their findings demonstrated that $Nb_{0.7\%}/Cu_{2\%}$-SSZ-13 achieved 90% NO_x conversion over a broad temperature range (200–625°C), significantly outperforming undoped Cu-SSZ-13. Additionally, the catalyst retained 67% NO_x conversion at 150 °C under standard test conditions of 500 ppm NO, 500 ppm NH_3, 5% O_2, 10% H_2O, and GHSV = 60000 h^{-1}. The introduction of Nb increased the abundance of $[Cu(OH)]^+$ active sites and enhanced Lewis and Brønsted acidity, promoting NH_3 adsorption and reactivity. Furthermore, the catalyst exhibited excellent SO_2 resistance, with NO_x conversion quickly recovering to 98.8% after SO_2 exposure was stopped. These results highlight the potential of Nb-modified Cu-SSZ-13 as a robust catalyst for practical NO_x abatement applications, particularly in low-temperature environments.

Table 2.1. Previous studies of Cu-based zeolite catalysts for NH_3-SCR

Reference	Catalyst	Test Setup	GHSV (h^{-1})	Max. NO/NO_x conversion rate
Wilken et al. (2013)	Cu/BEA	F.R.	30300	>90% @ 225-475 °C
Zhu et al. (2020)	$Cu_{1.8}$-SSZ-39	F.R.	400000	~100% @ 240-550 °C
Y. Cao et al. (2016)	CuY-SAPO-34	F.R.	30000	>90% @ 200-310 °C
Fu et al. (2021)	Cu-SSZ-39	F.R.	19000	~90% 260-550 °C
Lin et al. (2018)	CuFe/BEA	F.R.	40000	>90% @ 225-375 °C
Ming et al. (2019)	$Cu_{2.49}$-SAPO-18	F.R.	30000	>80% @ 225-575 °C
H. Wang et al. (2019)	Cu-BEA	F.R.	300000	>90% @ 250-325 °C
Yue et al. (2019)	Cu-ZSM-5	F.R.	180000	>90 @ 240-350 °C
Dou et al. (2015)	CuCe4-Z	F.R.	15000	95% @ 148-427 °C
J. Wang et al. (2021)	$Nb_{0.7\%}/Cu_{2\%}$-SSZ-13	F.R.	60000	>90% @ 200-625 °C

*F.R.: Fixed bed reactor

2.2. CO-SCR

The NH_3-SCR method is widely used for NO_x reduction in automotive and industrial exhaust gases, but alternative approaches utilizing inherent exhaust components like CO, H_2, and hydrocarbons are emerging as cost-effective and sustainable options (S. Liu et al., 2024). Among these, CO-SCR offers key advantages over NH_3-SCR, including the use of CO in flue gas as a reducing agent, integration of heat from CO oxidation into the process, and avoidance of by-products that deactivate catalysts, making it a promising technology for sustainable development (Li et al., 2023).

The general reactions involved in CO-SCR are expressed as follows (Gholami and Luo, 2018):

$$NO + CO \rightarrow 1/2N_2 + CO_2 \quad (2.11)$$

$$NO_2 + 2CO \rightarrow 1/2N_2 + 2CO_2 \quad (2.12)$$

$$2NO + 2CO \rightarrow N_2 + 2CO_2 \quad (2.13)$$

Some recent studies in the literature about the DeNOx performance of Cu-based-catalysts for CO-SCR are given in Table 2.2.

The SCR of NO with CO over alumina-supported catalysts has been investigated under oxygen-rich conditions (16 vol% O_2) by Liu et. al (K. Liu et al., 2018). Catalysts synthesized via the wet impregnation method included binary and ternary combinations of CuO/Cu_2O, Co_3O_4/CoO, MnO_2/Mn_2O_3, and CeO_2/Ce_2O_3. Among the catalysts tested, the $Cu–Mn/Al_2O_3$ catalyst with a Cu:Mn ratio of 1.5 demonstrated nearly 90% NO_x conversion at 160°C. The superior performance was attributed to the synergistic interaction between Cu_xO_y and Mn_xO_y, enhancing oxygen resistance and catalytic activity.

Li et al. (2023) have studied the potential of CuCe catalysts for CO-SCR (carbon monoxide selective catalytic reduction) reactions aimed at the simultaneous reduction of NO_x and CO from flue gases. The study emphasizes the superior catalytic activity and environmental advantages of CuCe catalysts over a wide temperature range (250-500°C), attributed to their high redox capacity and synergetic active sites.

Amano et al. (2006) investigated the catalytic reduction of NO with CO using low-loaded CuO/Al_2O_3 catalysts under oxidizing conditions. Their study highlighted that isolated Cu^{2+} species on γ-Al_2O_3 surfaces exhibit unique one-electron redox behavior ($Cu^{2+} \leftrightarrow Cu^{+}$), which promotes NO reduction while minimizing CO oxidation. At temperatures above 523 K, the catalyst selectively reduced NO to N_2 and N_2O even in the presence of O_2. The NO conversion reached approximately 30% at 773 K, with minimal N_2O formation compared to other copper oxide-supported catalysts.

The findings underline the importance of atomically dispersed Cu^{2+} species, which resist further reduction to metallic Cu^0, thereby enabling selective NO reduction in CO-SCR processes under challenging oxidizing environments.

Sierra-Pereira and Urquieta-González (2014) investigated the reduction of NO with CO over CuO and Fe_2O_3 catalysts supported on TiO_2 in the presence of O_2, SO_2, and water steam. Their findings showed that Fe_2O_3/TiO_2 catalysts achieved higher activity and selectivity for N_2 formation at temperatures below 450°C, compared to CuO/TiO_2 catalysts. Notably, Fe_2O_3 catalysts maintained superior stability under conditions with O_2, SO_2, and water steam at 500°C, demonstrating their robustness in realistic exhaust environments. These results highlight the potential of Fe_2O_3/TiO_2 catalysts for NO_x abatement in combustion processes.

Martínez-Arias et al. (2012) examined the redox and catalytic properties of CuO/CeO_2. They found that NO acts as a promoter for CO oxidation, significantly lowering the temperature required for CO conversion compared to reactions without NO. NO_x reduction occurred in two distinct steps, starting at approximately 443 K, with mechanisms transitioning as the temperature increased. The study highlights the role of interfacial sites between CuO and CeO_2 in facilitating NO reduction and enhancing the overall redox activity, making CuO/CeO_2 a promising candidate for catalytic NO_x abatement. This dual role of NO both as a promoter and a reactant provides valuable insights into the design of efficient catalysts for mixed CO and NO emissions control.

Gholami and Luo (2018) studied the low-temperature SCR of NO by CO using Cu-Ce catalysts supported on multi-walled carbon nanotubes (CNTs). Their findings revealed that the 20 wt.% Cu1:Ce3/CNT catalyst achieved a NO_x conversion of 96% at 220 °C, even in the presence of oxygen ($O_2/CO \leq 0.6$). This high activity was attributed to the synergistic interaction between surface oxygen vacancies and Cu^+ species. The study also demonstrated that higher oxygen concentrations ($O_2/CO \geq 0.6$) inhibited NO reduction due to preferential CO oxidation. The results highlight the potential of Cu-Ce/CNT catalysts for efficient NO_x removal at low temperatures in oxygen-rich environments.

Bai et al. (2019) investigated CuO/CeO_2-Al_2O_3 catalysts with varying Ce/Al molar ratios for the reduction of low-concentration NO with CO under oxidizing conditions, including O_2 and SO_2. Their findings indicated that the $Cu/Ce_{0.1}Al$ catalyst achieved over 90% NO conversion between 330°C and 650°C, demonstrating excellent catalytic performance and resistance to O_2 and SO_2. The synergistic interaction of Ce^{3+} and Cu^{2+} enhanced oxygen vacancy formation, improving the redox properties and adsorption capacities. The study concluded that incorporating ceria into alumina supports significantly lowered activation temperatures and increased N_2 selectivity, making $Cu/Ce_{0.5}Al$ a promising candidate for NO_x abatement in exhaust gas treatments.

Pan et al. (2020) examined the catalytic reduction of NO with CO using Cu-based and Mn-based catalysts supported on TiO_2. Among the tested catalysts, Cu-Ce-Fe-Co/TiO_2 and Mn-Ce-Fe-Co/TiO_2 exhibited the highest NO conversion efficiencies, achieving 100% NO conversion at 250°C

under conditions of 200 ppm NO, 200 ppm CO, and GHSV of 10,000 h^{-1}. The Cu-Ce-Fe-Co/TiO_2 catalyst demonstrated superior tolerance to H_2O, SO_2, and O_2, maintaining 94% NO conversion in the presence of 50 ppm SO_2 and 10% H_2O at 200°C.

Z. Liu et al. (2021) explored the catalytic reduction of NO with CO over transition-metal-doped ceria (TM-CeO_2) supported on two-dimensional vermiculite (VMT). Among the tested catalysts, Cu–Ce/VMT achieved 100% NO conversion at 300°C under test conditions of 1000 ppm CO, 500 ppm NO, and GHSV of 102000 h^{-1}, significantly outperforming other transition metal dopants. The study attributed this performance to the synergy between Cu and Ce, which enhanced the formation of oxygen vacancies (Ov) and improved redox properties. Density functional theory (DFT) calculations supported these findings, showing that Cu doping significantly reduced the energy barriers for the CO-SCR reaction.

Du et al. (2023) investigated the catalytic performance of a Cu_xO_y(9)-CeO_2(1) catalyst for the NO reduction with CO under oxidizing conditions. The catalyst achieved 100% NO conversion at 150°C and 100% N_2 selectivity under a gas composition of 500 ppm NO, 5000 ppm CO, and a space velocity of 7800 h^{-1}. The study revealed that CO pretreatment significantly enhanced catalytic activity by creating and stabilizing surface synergistic oxygen vacancies (SSOVs). These vacancies facilitated NO adsorption and dissociation, forming N_2 and CO_2 as final products.

Table 2.2. Previous studies of Cu-based catalysts for CO-SCR

Reference	Catalyst	Test Setup	GHSV (h^{-1})	Max. NO/NO_x conversion rate
K. Liu et al. (2018)	Cu–Mn/Al_2O_3	F.R.	10000	~90% @ 160 °C
Li et al. (2023)	CuCe	F.R.	90000	>80% @ 250-500 °C
Amano et al. (2006)	CuO/TiO_2	F.R.	12000	>30% @ 500 °C
Sierra-Pereira and Urquieta-González (2014)	10Cu/Ti	F.R.	75000	60% @ 500 °C
Martínez-Arias et al. (2012)	CuO/CeO_2	F.R.	30000	100% @ 570 °C
Bai et al. (2019)	Cu/$Ce_{0.5}Al$	F.R.	36000	96% @ 333 °C
Gholami and Luo (2018)	Cu1:Ce3/CNT	F.R.	12600	96% @ 220 °C
Pan et al. (2020)	Cu-Ce-Fe-Co/TiO_2	F.R.	10000	87% @ 200 °C
Z. Liu et al. (2021)	Cu-Ce/VMT	F.R.	102000	100% @ 300 °C
Du et al. (2023)	Cu_xO_y(9)-CeO_2(1)	F.R.	7800	100% @ 150 °C

*F.R.: Fixed bed reactor

2.3. H_2-SCR

Among the diverse SCR technologies, hydrogen-based H_2-SCR stands out as a highly effective method for NO_x removal. This approach offers several advantages, including exceptional selectivity, operation at lower temperatures, compatibility with a wide range of catalysts, and reduced reliance on noble metals. Furthermore, the availability of hydrogen and the environmentally benign nature of the process position H_2-SCR as a promising green technology for efficient NO_x reduction and sustainable emissions management (Muhammad Farhan et al., 2024). The reactions involved in the H_2-SCR system are represented by Equations (2.14), (2.15), and (2.16) (Qi et al., 2006).

$$2NO + 4H_2 + O_2 \rightarrow N_2 + 4H_2O \quad (2.14)$$

$$2NO + 3H_2 + O_2 \rightarrow N_2O + H_2O \quad (2.15)$$

$$O_2 + 2H_2 \rightarrow H_2O \quad (2.16)$$

Equation (2.14) represents the desired reaction responsible for converting NO to N_2, the primary goal of the H_2-SCR process. Conversely, Equation (2.16) describes the oxidation of H_2, while Equation (2.15) corresponds to an undesirable side reaction leading to the formation of N_2O. N_2O is a highly detrimental gas due to its significant environmental impact and contribution to climate change. Its greenhouse gas effect is notably more pronounced than that of CO_2, underscoring the importance of minimizing N_2O formation in catalytic processes (Costa and Efstathiou, 2007).

The utilization of H_2 in SCR has been a topic of extensive research over the years. Investigations into H_2-SCR systems have predominantly focused on simulated diesel engine emissions under controlled laboratory conditions, employing a variety of catalysts to evaluate system performance. Table 2.3 presents a summary of recent studies from the literature investigating the $DeNO_x$ performance of zeolite-based catalysts in H_2-SCR systems.

Yu et al. (2010) investigated the effect of chromium (Cr) on the catalytic performance of Pt/ZSM-35 for the selective catalytic reduction (SCR) of NO with H_2 in excess oxygen. They found that the addition of Cr significantly enhanced catalytic activity, achieving a 94.7% NO conversion at 120°C, compared to 80.5% for Pt/ZSM-35 without Cr. This improvement was attributed to the increased formation of NH_4^+ species and the promotion of NO adsorption facilitated by Cr. The catalyst with 1 wt.% Cr prepared through co-impregnation exhibited optimal performance, with enhanced surface interactions between Pt and Cr identified as key to its activity.

L. Cao et al. (2020) developed a novel Pt/Beta catalyst for low-temperature H_2-SCR of NO_x. The catalyst achieved 100% NO conversion at 90°C under oxygen-rich conditions (1000 ppm NO, 1% H_2, 4% O_2). Using polyvinylpyrrolidone (PVP) as a structure-directing agent, they enhanced the dispersion and size control of Pt particles, which significantly improved catalytic performance. However, the study observed irreversible SO_2 poisoning in the Pt/Beta catalyst system, with some recovery achieved through Zr and Ce modifications.

Wen (2002) investigated the SCR of NO with H_2 over Pd/MFI catalysts in the presence of excess O_2. The catalyst prepared by the sublimation method achieved 70% NO conversion to N_2 at 100°C under test conditions of 1000 ppm NO, 8000 ppm H_2, 2% O_2, and a GHSV of 90000 h^{-1}. Pd^0 was identified as the active site for NO reduction, and no formation of undesired byproducts such as N_2O or NH_3 was observed. The presence of O_2 inhibited NH_3 formation while allowing NO reduction to proceed selectively. At higher temperatures, the oxidation of Pd^0 and agglomeration of PdO led to decreased catalytic activity.

Borchers et al. (2023) investigated the SCR of NO_x using H_2 over palladium-based catalysts supported on ZSM-5 and Zeolite Y. Their study revealed that adding 10% and 20% TiO_2 to the catalyst formulations enhanced catalytic performance. The 1%Pd/20%TiO_2/HY catalyst achieved over 85% NO conversion at 250°C under test conditions of 1000 ppm NO, 5000 ppm H_2, 10% O_2, and GHSV of 60000 h^{-1}, outperforming a benchmark catalyst (1%Pd/5%V_2O_5/20%TiO_2-Al_2O_3). The incorporation of TiO_2 improved the reducibility of Pd particles and shifted selectivity towards N_2 while reducing undesired byproducts such as N_2O. However, water tolerance varied significantly between the two supports; Zeolite Y-based catalysts maintained high activity and selectivity in humid conditions, whereas ZSM-5-based catalysts suffered substantial performance losses.

Li et al. (2015) examined the effect of support properties on the catalytic performance of Pt-based catalysts for H_2-SCR of NO_x. The study compared four supports: HZSM-5, ZrO_2, γ-Al_2O_3, and MgO. Among these, Pt/HZSM-5 exhibited the highest NO_x conversion, reaching 71.4% at 120°C, and superior N_2 selectivity, outperforming other supports due to its strong acidity and low NO_x adsorption capacity.

Hong et al. (2019) investigated the H2-SCR of NO_x using hydrogen over Pt/SSZ-13, Pt/ZSM-5, and Pt/SAPO-34 catalysts. Among these, Pt/SSZ-13 demonstrated the highest performance, achieving 81% NO_x conversion at 100°C with an N_2 selectivity of 93% under test conditions of 1000 ppm NO, 5000 ppm H_2, 10% O_2, and GHSV of 50000 h^{-1}. The Pt/SSZ-13 catalyst also exhibited superior SO_2 and H_2O resistance compared to the other catalysts, with only minor deactivation observed.

L. Wang et al. (2014) studied the SCR of NOx using H_2 over Zn-ZSM-5, Pd/Zn-ZSM-5, and Pd/Ru/W/(ZrO_2-SiO_2)SO_4 catalysts under oxidizing conditions. Among these, Pd/Ru/W/(ZrO_2-SiO_2)SO_4 achieved the highest NO_x conversion of 75.5% at 150°C, while Zn-ZSM-5 exhibited a maximum NO_x conversion of 39.5% at 250°C. The Pd/Zn-ZSM-5 catalyst showed intermediate performance with a peak NO_x conversion of 61.4% at 250°C.

Hong et al. (2018) investigated H_2-SCR of NO over Pt nanoparticles encapsulated in hollow ZSM-5 zeolites. The Pt/h-ZSM-5 catalyst demonstrated superior activity, achieving 84% NO conversion at 90°C with 92% N_2 selectivity under conditions of 1000 ppm NO, 5000 ppm H_2, 10% O_2, and a GHSV of 50000 h^{-1}.

Table 2.3. Previous studies of zeolite-based catalysts for H_2-SCR

Reference	Catalyst	Test Setup	GHSV (h^{-1})	Max. NO/NO_x conversion rate
Yu et al. (2010)	Pt/Cr/ZSM-35	F.R.	80000	95% @ 120 °C
L. Cao et al. (2020)	Pt/Beta	F.R.	32000	100% @ 90 °C
Wen (2002)	Pd/MFI	F.R.	90000	70% @ 100 °C
Borchers et al. (2023)	Pd/TiO_2/ZSM-5 Pd/TiO_2/HY	F.R.	60000	80% @ 260 °C 85% @ 190 °C
Li et al. (2015)	Pt/HZSM-5	F.R.	36000	~70% @ 120 °C
Hong et al. (2019)	Pt/SSZ-13	F.R.	50000	81% @ 100 °C
L. Wang et al. (2014)	Pd/Zn-ZSM-5	F.R.	12000	~62% @ 250 °C
Hong et al. (2018)	Pt/ZSM-5	F.R.	50000	84% @ 90 °C

*F.R.: Fixed bed reactor

2.4. HC and OHC-SCR

The catalysts employed in HC or OHC-SCR for NO_x removal primarily consist of zeolite catalysts, metal oxide catalysts, and noble-metal catalysts. Among these, zeolite catalysts are extensively utilized in HC or OHC-SCR due to their remarkable specific surface areas, high selectivity, and superior catalytic activity (J. Xu et al., 2020).

Schay et al. (2002) studied the $DeNO_x$ reactions over Cu-ZSM-5 catalyst, focusing on the decomposition of NO and N_2O as well as the SCR of NO with propane and methane. The SCR of NO with propane achieved conversion efficiencies of 80-100% at 320-370°C, whereas SCR with methane exhibited significantly lower NO conversion (~20%) at higher temperatures. The research further highlighted that only 10–20% of the copper in the zeolite catalysts actively participates in the catalytic cycles.

Saaid et al. (2002) investigated the SCR of NO_x using a bimetallic Pt-Cu-ZSM-5 catalyst with i-C_4H_{10} as the reducing agent under oxygen-rich conditions. The bimetallic catalyst demonstrated a significantly wider operating temperature window than its monometallic counterparts (Pt-ZSM-5 and Cu-ZSM-5), achieving more than 50% NO_x conversion between 250°C and 520°C. The Pt-Cu-ZSM-5 catalyst was resistant to oxygen and high space velocities.

Habib et al. (2014) researched DeNOx performance of Cu/Y zeolite catalysts using propane. Among the catalysts tested, 16 wt.% Cu/Y (16Cu/Y) exhibited the highest performance, achieving a maximum NO_x to N_2 conversion yield of 98% at 290°C, under a feed containing 1000 ppm NO_x, 1000 ppm C_3H_6, 12 vol% O_2, and 5 vol% H_2O with a GHSV of 47000 h^{-1}.

Janas and Dzwigaj (2011) compared the catalytic activity of FeAlBEA and FeSiBEA zeolites for the selective catalytic reduction (SCR) of NO with ethanol and methane. The study revealed that FeAlBEA showed superior catalytic performance compared to FeSiBEA, achieving a maximum NO conversion of 53% at 673 K in SCR with ethanol. Conversely, FeSiBEA, containing predominantly framework Fe(III) species, exhibited a lower maximum NO conversion of 40% at 623 K.

Bartolomeu et al. (2011) evaluated the catalytic activity of Ag/H-ZSM-5 and H-ZSM-5 zeolites for the SCR of NO_x using ethanol. The results demonstrated that Ag/H-ZSM-5 exhibited

superior performance, achieving a maximum NO_x conversion of 48% at 500°C, compared to 24% for H-ZSM-5. The study also highlighted the critical role of silver particles in enhancing the oxidation of NO to NO_2 and the subsequent reduction of NO to N_2.

Dzwigaj et al. (2009) compared the catalytic performance of commercial BEA, MOR, and MFI zeolites for the SCR of NO using ethanol. The study demonstrated that HAlBEA(700), with higher Fe impurity levels, achieved the best performance, with a maximum NO conversion of 62% at 673-723 K and N_2 selectivity exceeding 90%. In contrast, MOR(150) and MFI(300) showed lower NO conversions of 43% and 37.5%, respectively, under similar conditions. The superior activity of BEA was attributed to tetrahedral and octahedral Fe(III) species near lattice Al, which enhanced catalytic activity compared to other zeolites.

Janas et al. (2007) compared the catalytic performance of $Co_{0.7}$SiBEA and $Co_{3.6}$SiBEA zeolites for the SCR of NO using ethanol. $Co_{0.7}$SiBEA demonstrated superior activity, achieving a maximum NO conversion of 75% and selectivity toward N_2 exceeding 95% at 623 K. Conversely, $Co_{3.6}$SiBEA exhibited a lower maximum NO conversion of 60% and N_2 selectivity above 50% in the range of 573-725 K, with significant NO_2 formation at higher temperatures.

Popovych et al. (2016) investigated the effect of partial dealumination of BEA zeolites on the physicochemical and catalytic properties of AgAlSiBEA catalysts for the H_2-promoted SCR of NO with ethanol. The study demonstrated that the catalytic activity and NO-to-N_2 conversion were significantly influenced by the Si/Al ratio and the silver content. The AgAlSiBEA catalyst with a Si/Al ratio of 100 exhibited higher catalytic performance, achieving up to 56% NO conversion at 675 K, compared to its counterpart with a Si/Al ratio of 200.

Table 2.4. Previous studies of zeolite-based catalysts for HC and OHC-SCR

Reference	Catalyst	Reductant	GHSV (h^{-1})	Max. NO/NO_x conversion rate
Schay et al. (2002)	Cu-ZSM-5	C_3H_8	-	80-100% @ 320-370 °C
Saaid et al. (2002)	Pt-Cu-ZSM5	C_4H_{10}	10000-90000	80-90% @ 350-400 °C
Habib et al. (2014)	Cu/Y	C_3H_6	47000	98% @ 290 °C
Janas and Dzwigaj (2011)	FeAlBEA FeSiBEA	C_2H_5OH	10000	53% @ 673 K 40% @ 623 K
Bartolomeu et al. (2011)	Ag/H-ZSM-5	C_2H_5OH	-	48% @ 500 °C
Dzwigaj et al. (2009)	HAlBEA	C_2H_5OH	10000	62% @ 673-723 K
Janas et al. (2007)	Co0.7SiBEA	C_2H_5OH	-	75% @ 623 K
Popovych et al. (2016)	AgAlSiBEA	C_2H_5OH	24000	56% @ 675 K

*F.R.: Fixed bed reactor

2.5. Previous Studies on Sm

Samarium (Sm), a rare earth element with unique chemical properties, has emerged as a noteworthy material in the field of catalyst development. Particularly in studies aimed at enhancing catalyst performance, Sm has demonstrated significant potential due to its high thermal stability, oxygen storage capacity, and catalytic efficiency.

The use of Sm as a catalytic material dates back to the early 2000s, with initial studies involving the impregnation of Sm_2O_3 in varying ratios onto V_2O_5 catalysts (Barbero and Cadus, 2002). These materials were subjected to characterization analyses such as BET, X-ray diffraction (XRD), temperature-programmed reduction (TPR), Fourier transform infrared spectroscopy (FT-IR), X-ray photoelectron spectroscopy (XPS), and transmission electron microscopy (TEM). The results demonstrate the formation of $SmVO_4$ through a solid-state reaction, which significantly influences the catalytic performance, especially in propane oxidative dehydrogenation reactions.

Han et al. (2018) investigated the use of Sm-doped Mn on zirconium-iron polymeric pillared interlayered montmorillonite (ZrFe-PILM) catalysts for low-temperature selective catalytic reduction (SCR) of NO_x with ammonia. The Mn/Sm molar ratio of 18:2 showed the highest catalytic activity, achieving a NO_x conversion rate of 95.5% at 200°C. The results indicated that Sm addition improved surface acidity, particularly weak acid sites, which enhanced ammonia adsorption and activation.

Sun et al. (2018) studied the Sm-doped MnO_x-TiO_2 catalysts and have shown promising results in NH_3-SCR systems, achieving high NO_x conversion rates of up to 100% at temperatures between 125-275°C, with a maximum N_2 selectivity of over 95%. The catalysts utilize NH_3 as the reductant and operate at a GHSV of 30000 h^{-1}. Sm doping enhances the catalyst's redox properties, improves SO_2 resistance, and broadens the operating temperature range, making it highly effective for low-temperature applications. These characteristics position Sm-doped catalysts as a potential solution for efficient NO_x reduction in industrial processes.

Gao et al. (2018) examined SCR of NO_x with NH_3 using Sm-modified MnO_x-TiO_2 catalysts prepared via inverse co-precipitation. The optimal SMT-0.3 catalyst, with a Sm/Mn molar ratio of 0.3, achieved 100% NO_x conversion in a broad temperature range (180-390 °C) and 100% N_2 selectivity from 120-390 °C under a GHSV of 36000 h^{-1}. Sm addition enhanced the specific surface area, increased chemisorbed oxygen species, and strengthened acid sites on the catalyst surface while modifying the SCR mechanism. The SMT-0.3 catalyst exhibited a fast SCR reaction mechanism above 200 °C, demonstrating superior performance compared to MnOx-TiO_2 without Sm. The study highlighted Sm-modified MnO_x-TiO_2 as a promising low-temperature NO_x reduction catalyst.

H. Liu et al. (2019) conducted an activity test on a fixed bed, SmCeTi catalyst achieved nearly 98% NO_x conversion at 250°C, with over 96% N_2 selectivity. The Sm-doped catalyst maintained high activity under SO_2 and H_2O exposure, with a NO_x conversion rate of ~80% after prolonged exposure to both contaminants. These findings highlighted the potential of Sm-doped CeO_2-TiO_2 catalysts as efficient and durable solutions for industrial NO_x reduction.

Y. Wang et al. (2020) investigated the enhancement of hydrothermal stability in Al-rich Cu-SSZ-13 catalysts for NH_3-SCR reactions through modification with Ce and Sm. The Ce- or Sm-modified Cu-SSZ-13 catalysts, prepared via ion exchange, demonstrated significant improvements in structural stability, catalytic activity, and resistance to hydrothermal aging. The catalysts achieved

a high NO_x conversion rate of over 80% in a temperature range of 250-550°C with minimal N_2O formation.

Q. Xu et al. (2020) designed a novel Ti-doped Sm-Mn mixed oxide ($TiSmMnO_x$) catalyst for low temperature SCR of NO_x. The $TiSmMnO_x$ catalyst achieved over 80% NO_x conversion and above 90% N_2 selectivity in a wide operating temperature range of 60-225°C under a GHSV of 50000 h^{-1}. Also, the $TiSmMnO_x$ catalyst displayed high durability, maintaining over 80% NO_x conversion even at elevated space velocities. These results highlighted the potential of $TiSmMnO_x$ catalysts for industrial low-temperature NO_x removal applications.

L. Chen et al. (2021) conducted on research to evaluate the effects of Sm modification on Mn oxide biochar-based (BC) catalysts for low-temperature NH_3-SCR of NO_x. The Sm(0.2)-Mn/BC catalyst demonstrated the best performance, achieving 85% NO_x conversion at 200°C with high N_2 selectivity in a broad temperature range of 75-250°C. Sm doping increased the surface oxygen content (Oα) and enhanced weak acid sites, significantly improving NH_3 adsorption and catalytic activity.

Z. Chen et al. (2022) have investigated the effects of samarium (Sm) doping on MnFeOx catalysts for low-temperature NH_3-SCR processes. Their findings indicate that the optimal SmMnFe-0.1 catalyst achieved nearly 100% NO conversion between 75-200 °C and maintained about 90% NO conversion even in the presence of SO_2 and H2O, under test conditions of 500 ppm NO, 500 ppm NH_3, 5% O_2, 5% H_2O, 100 ppm SO_2, and a GHSV of 60000 h^{-1}. Sm doping enhanced catalyst performance by increasing oxygen vacancies, facilitating NO oxidation to NO_2, and promoting a fast SCR reaction. Additionally, Sm inhibited sulfation of active Mn sites by redirecting SO_2 to react with Fe species, improving SO_2 resistance and catalyst durability.

M. Chen et al. (2022) investigated the NH_3-SCR performance of Cu-SSZ-13 catalysts enhanced with Sm^{3+} ions, achieving nearly 90% NO_x conversion across a wide temperature range of 200–550°C. The Sm^{3+} ions improved the catalytic activity by facilitating the formation of active $[ZCu^{2+}(OH)]^+$ species and enhancing electron transfer. Even after hydrothermal aging at 750°C for 16 hours, the Sm-modified catalyst retained higher NOx conversion compared to unmodified Cu-SSZ-13. This enhancement was attributed to the stability of Cu active sites, reduced formation of inactive CuO_x species, and improved intermediate formation (NH_4NO_2 and H_2NNO), highlighting the potential of Sm incorporation for robust NOx abatement in NH_3-SCR systems.

S. Zhang et al. (2023) investigated the effects of Sm doping on manganese-titanium oxide (Mn-TiO_2) catalysts for NH_3-SCR of NO_x. The optimal catalyst, $Sm_{0.15}Mn_{0.15}Ti$, achieved 100% NO conversion and 87% N_2 selectivity at 180-300°C under a GHSV of 36000 h^{-1}. Sm doping enhanced the catalyst's BET surface area, surface oxygen concentration, and acidity while suppressing Mn^{4+} content to improve N_2 selectivity and reduce N_2O formation.

Q. Zhang et al. (2024) examined Sm-doped $MnFeO_x$ catalysts for low-temperature NH_3-SCR applications, achieving close to 100% NO_x conversion between 90°C and 240°C and maintaining

over 80% selectivity for N_2. The optimal Sm loading (7.5% by weight) significantly improved SO_2 resistance, with only a 3.65% activity reduction after 10 hours of SO_2 exposure at 180 °C. Sm doping increased weak acid sites and enhanced redox properties, facilitating better NH_3 adsorption and active site availability. The catalyst operates under a GHSV of 50000 h^{-1}, demonstrating its potential for efficient industrial NO_x reduction at low temperatures.

Table 2.5 highlights previous studies on Sm-doped SCR catalysts.

Table 2.5. Previous studies of Sm-doped SCR catalysts

Reference	**Catalyst**	**Reductant**	**Test Setup**	**GHSV (h^{-1})**	**Max. NO/NO_x conversion rate**
Han et al. (2018)	Mn–Sm/ZrFe-PILM	NH_3	F.R.	20000	~95% @ 200 °C
Sun et al. (2018)	MnO_x-SmO_x(ZrO_x)-TiO_2	NH_3	F.R.	30000	100% @ 125-275 °C
Gao et al. (2018)	SMT-0.3	NH_3	F.R.	36000	100% @ 180-390 °C
H. Liu et al. (2019)	$Sm_{0.1}Ce_{0.3}Ti$	NH_3	F.R.	90000	98% @ 250 °C
Y. Wang et al. (2020)	$Cu_{2.5}Ce_{0.5}$-SSZ-13 $Cu_{2.4}Sm_{0.5}$-SSZ-13	NH_3	F.R.	800000	>80% @ 250-450 °C >80% @ 250-550 °C
Q. Xu et al. (2020)	$TiSmMnO_x$	NH_3	F.R.	50000	~100% @ 80-200 °C
L. Chen et al. (2021)	Sm(0.2)-Mn/BC	NH_3	F.R.	36000	~85% @ 200 °C
Z. Chen et al. (2022)	SmMnFe-0.1	NH_3	F.R.	60000	~100% @ 75-200 °C
M. Chen et al. (2022)	Cu-Sm-SSZ-13	NH_3	F.R.	60000	>90% @ 200-550 °C
S. Zhang et al. (2023)	$Sm_{0.15}Mn_{0.15}Ti$	NH_3	F.R.	36000	100% @ 180-300 °C
Q. Zhang et al. (2024)	$Sm_{7.5}CeMnFe$	NH_3	F.R.	50000	100% @ 90-240 °C

*F.R.: Fixed bed reactor

3. MATERIAL AND METHOD

In this section, a comprehensive explanation of all the characteristics of the materials used in the study will be provided, the procedures for their collection, any alterations they underwent, and their condition throughout the research process. Additionally, the methods applied during the study will be outlined in detail, with a clear description of any modifications made to these methods.

3.1. Materials for Catalyst Preparation

3.1.1. Cordierite Structure

Ceramic cordierite with a cell density of 400 cells per square inch (cpsi), a length of 100 mm, and a diameter of 130 mm was utilized as the carrier material with a chemical formula $2Al_2O_3.5SiO_2.2MgO$ (Figure 3.1). Cordierite was selected for experimental use over other carrier structures due to its high catalytic loading capacity, durability, material strength, low thermal expansion coefficient, and cost-effectiveness.

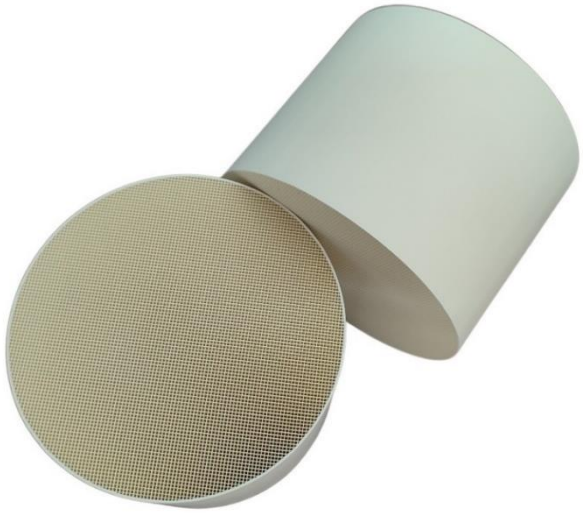

Figure 3.1. Cordierite

3.1.2. Oxalic Acid Dihydrate

Oxalic acid dihydrate was employed in the catalyst preparation process to enhance the surface area of the cordierite. The oxalic acid dihydrate used in the study was of the Merck-Supelco brand. Its chemical formula is $C_2H_2O_4*2H_2O$, and the corresponding CAS number is 6153-56-6 (Figure 3.2). The chemical properties of the oxalic acid dihydrate are given in Table 3.1.

Figure 3.2. Oxalic acid dihydrate

Table 3.1. The chemical properties of oxalic acid dihydrate

Product information	
Molecular weight	126.07 g/mol
Boiling point	149-160 °C (1013 hPa)
Density	1.65 g/cm^3 (20 °C)
Flash point	157 °C
Melting Point	98-100 °C
pH value	1.5 (10 g/L, H_2O)
Solubility	> 100 g/L

3.1.3. Zeolite Y

Zeolite Y was employed in the catalyst preparation process to support the cordierite for the active materials. The Zeolite Y used in the study was of Thermo Fisher-Alfa Aesar brand. Its molecular formula is Al_2O_5Si, and the corresponding CAS number is 1318-02-1 (Figure 3.3). Zeolite Y has 730 m^2/g specific surface area and 5.1:1 mole ratio of SiO_2:Al_2O_3.

Figure 3.3. Zeolite Y

3.1.4. Zeolite Beta

Zeolite Beta was also employed in the catalyst preparation process to support the cordierite for the active materials. The Zeolite Beta used in the study was of ABCR Chemicals brand. Its molecular formula is Al_2O_5Si, and the corresponding CAS number is 1318-02-1 (Figure 3.4). Zeolite Beta has a 710 m^2/g specific surface area and a 38:1 mole ratio of SiO_2:Al_2O_3.

Figure 3.4. Zeolite Beta

3.1.5. Copper (II) chloride

Copper (II) chloride was used as the primary active material in the catalyst production process, particularly during the ion exchange procedure. Its chemical formula is $CuCl_2$, with a CAS number of 7447-39-4, and it was sourced from Merck Sigma-Aldrich. The chemical properties of the $CuCl_2$ are given in Table 3.2.

Table 3.2. The chemical properties of copper (II) chloride

Product information	
Molecular weight	134.45 g/mol
Density	3.39 g/cm^3 (20 °C)
Melting Point	498 °C
pH value	3.5 (20°C, 50 g/L in H_2O)
Solubility	620 g/L

3.1.6. Samarium oxide

Samarium oxide was used as the secondary active material and was sourced from Nanografi. Its CAS number is 12060-58-1, and its chemical formula is Sm_2O_3 (Figure 3.5). The chemical properties of the samarium oxide are given in Table 3.3.

Figure 3.5. Samarium oxide

Table 3.3. The chemical properties of samarium oxide

Product information	
Purity	99.99%
Particle Size	325 mesh
Density (g/cm^3)	8.35 g/cm^3
Molecular weight	348.72 g/mol
Melting Point (°C)	2335 °C
Crystal Structure	Cubic

3.1.7. Cerium oxide

Cerium oxide was used just a small amount to enhance both the efficiency and durability of catalyst. The cerium dioxide used in this study was of Merck brand, with a CAS number of 13306-38-3, and its chemical formula is CeO_2 (Figure 3.6). The chemical properties of the cerium oxide are given in Table 3.4.

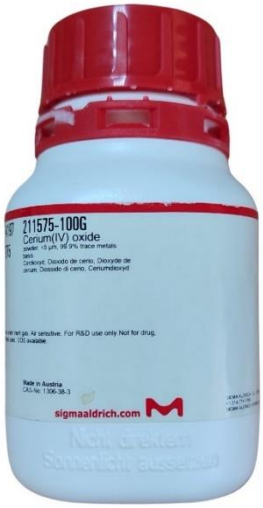

Figure 3.6. Cerium oxide

Table 3.4. Chemical properties of cerium oxide

Product information	
Purity	99.9%
Particle Size	<5 µm
Density (g/cm^3)	7.13 g/cm^3 (25 °C)
Molecular weight	172.11 g/mol

3.1.8. Colloidal Silica

In this study, Ludox HS-40 colloidal silica served as the binder in the catalyst preparation process. Its chemical formula is SiO_2, with a CAS number of 7631-86-9, and it is sourced from Merck Sigma-Aldrich. The chemical properties of the colloidal silica are given in Table 3.5.

Table 3.5. The chemical properties of colloidal silica

Product information	
Quality level	100
Form	Viscous liquid
Concentration	40 wt. % suspension in H_2O
Surface area	~ 220 m^2/g
pH value	9.8
Density (g/cm^3)	1.3 g/cm^3 (25 °C)
Molecular weight	60.08 g/mol

3.1.9. Ethanol

Various alcohols are utilized as reductants in scientific studies examining SCR performance systems. In this study, ethanol was used. Its chemical formula C_2H_6O and CAS number of 64-17-5 (Figure 3.7). The chemical properties of the ethanol are given in Table 3.6.

Figure 3.7. Ethanol

Table 3.6. The chemical properties of ethanol

Product information	
Molecular weight	46.07 g/mol
Boiling point	78,29 °C (1013 hPa)
Density	0.79 g/cm^3 (20 °C)
Flash point	13 °C (closed cup)
Melting Point	-114.0 °C
pH value	7.0 (20 °C, 10 g/L in H_2O)

3.2. Devices for Catalyst Preparation

3.2.1. Precision scales

Radwag AS 220 R2 was used to weigh the necessary chemicals. The technical properties of the scales are given in Table 3.7 and the scales are shown in Figure 3.8.

Table 3.7. The technical properties of Radwag AS 220 R2

Device information	
Maximum capacity	220 g
Minimum capacity	10 mg
Precision	0.1 mg
Repeatability	0.1 mg
Operating temperature	+10 °C - +40 °C
Power supply	12/16 V DC
Response time	3.5s
Calibration type	Automatic
Net weight	5.6 kg

Figure 3.8. Radwag AS 220 R2

3.2.2. Magnetic stirrer with heating

A magnetic stirrer with heating, model MS300 HS from the MTOPS brand, was used to mix the solution prepared for catalyst production (Figure 3.9). The technical specifications of the device are provided in Table 3.8.

Figure 3.9. MTOPS MS300 HS

Table 3.8. The technical properties of MTOPS MS300 HS

Device information	
Temperature	Max 380 °C
Temperature control	Electronic Energy Regulator
Heating power	680 W
Mixing speed	100-1500 rpm
Mixing capacity	5 L (H_2O)
Heating plate	Ceramic coated aluminum
Plate dimensions	180 x 180 mm
Net weight	2.9 kg

3.2.3. Ultrasonic stirrer

During the preparation of solutions to be used in the production of catalysts, an ultrasonic stirrer Vibra-Cell V750 was used as well as a magnetic stirrer. The picture of the ultrasonic mixer can be seen in Figure 3.10, and its technical specifications can be seen in Table 3.9.

Figure 3.10. Vibra-Cell V750

Table 3.9. The technical specifications of Vibra-Cell V750

Device information		
Power supply	Power Output	Max. 750 W
	Frequency	20 kHz
	Dimensions	235 x 190 x 340mm
	Weight	6.8 kg
Converter	Diameter	64 mm
	Height	183 mm
	Weight	900 g
	Cable length	1.8 m
Standard prop	Tip Diameter	13 mm
	Length	139 mm
	Material	Ti6Al4V titanium alloy
	Weight	340 g
	Capacity	10-250 ml

3.2.4. Drying oven

During the catalyst preparation, the drying process was conducted using a MEMMERT BAIC UNB 500 oven (Figure 3.11). The technical specifications of the drying oven are provided in Table 3.10.

Figure 3.11. Memmert Baic UNB 500 oven

Table 3.10. The technical properties of Memmert Baic UNB 500 oven

Device information	
Chamber width/height/depth	560 x 480 x 400 mm
Chamber volume	108 L
Oven width/height/depth	710 x 760 x 550 mm
Maximum temperature	220 °C
Power	2000 W
Weight	50 kg
Total load per oven	60 kg
Ambient conditions	5 °C to 40 °C
Setting accuracy	0.5 °C

3.2.5. Sintering oven

During the catalyst preparation, the sintering process was performed using a Protherm PLF 110/6 oven (Figure 3.12). The technical specifications of the Protherm PLF 110/6 oven are presented in Table 3.11.

Figure 3.12. Protherm PLF 110/6

Table 3.11. The technical specifications of Protherm PLF 110/6

Device information	
Chamber width/height/depth	150 x 210 x 200 mm
Chamber volume	6.3 L
Oven width/height/depth	650 x 550 x 580 mm
Maximum temperature	1100 °C
Power	2000 W

3.3. Methods for Catalyst Preparation

Figure 3.13 illustrates the main step for catalyst preparations in this study.

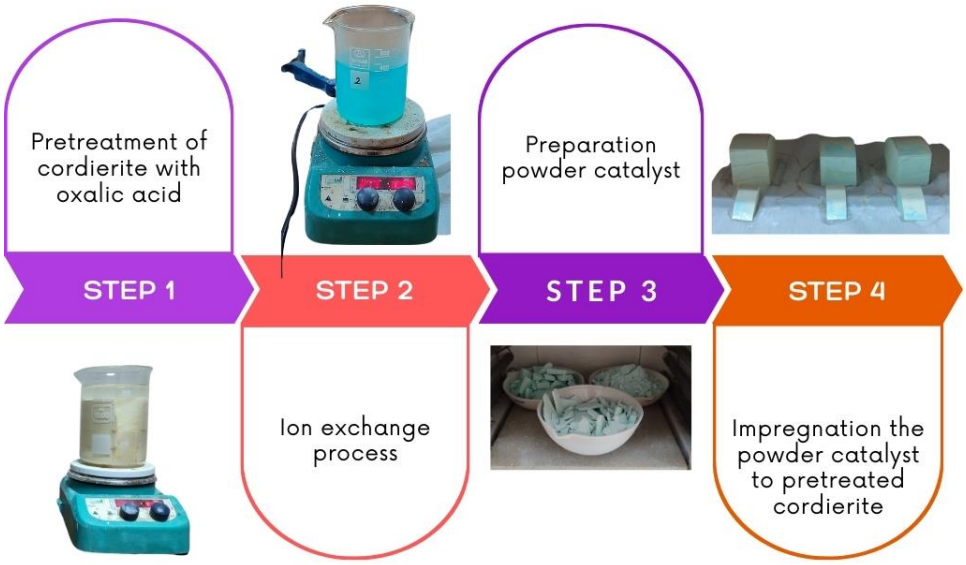

Figure 3.13. Catalyst preparation steps

In the first step, the cordierite structure was pretreated with oxalic acid to enhance the specific surface area. To carry out this process, the cordierite structure was immersed in 500 ml of deionized water in a beaker, and 250 grams of oxalic acid was added. The cordierite structure was subjected to treatment at approximately 95°C for four hours. After the treatment, the structure was washed with deionized water until the pH was balanced. Following the washing process, it was dried at 120°C for one hour and subsequently sintered at 500°C for two hours. As a result of these procedures, a pre-treated cordierite structure was prepared. Figure 3.14 shows the details of the ion exchange process.

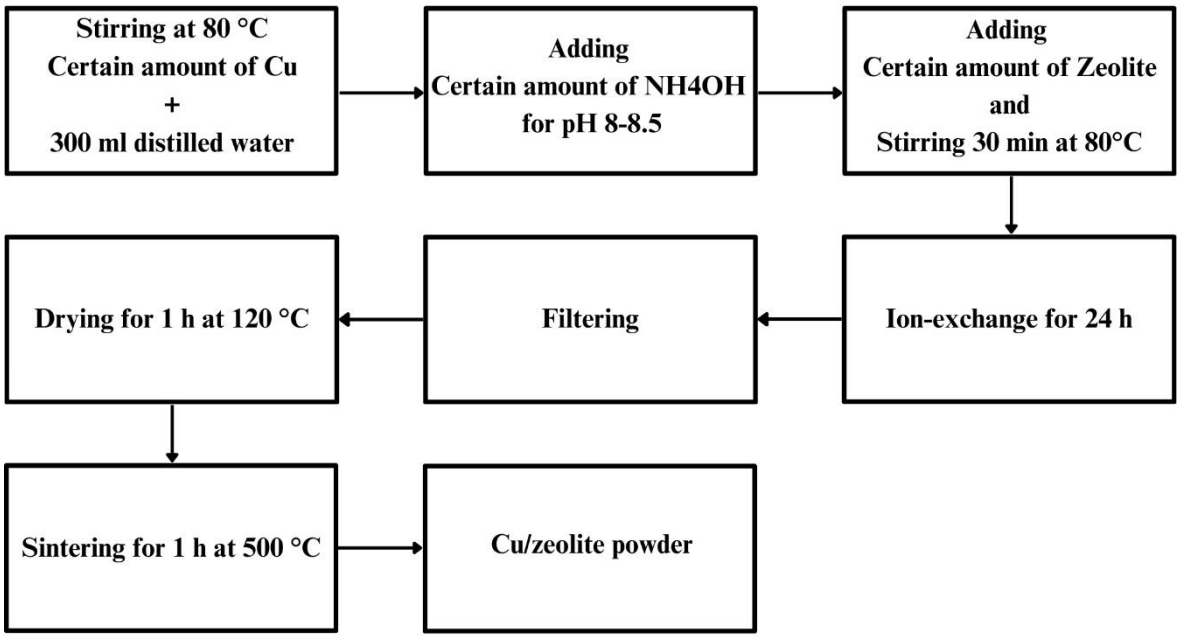

Figure 3.14. The main steps for the ion exchange process

First, 300 ml of distilled water was mixed with Cu, followed by stirring for 30 minutes at 80°C. A small amount of NH_4OH was added to adjust the pH to 8-8.5. Then, a certain amount of zeolites was added, and the was stirred for another 30 minutes at 80°C. The solution underwent 24 hours of ion exchange, after which it was filtered. The product was dried for 1 hour at 120°C, followed by 1 hour of calcination at 500°C. The obtained powder was called Cu/zeolite powder.

The Cu-zeolite was combined with chemicals and 300 ml of distilled water. The mixture was subjected to ultrasonic stirring for 15 minutes, and the water was evaporated by magnetic stirring. The product was dried for 2 hours at 120°C, followed by 3 hours of calcination at 500°C. The last product was called powder catalyst. In Figure 3.15, the stages of powdered catalyst production are visualized for easier understanding.

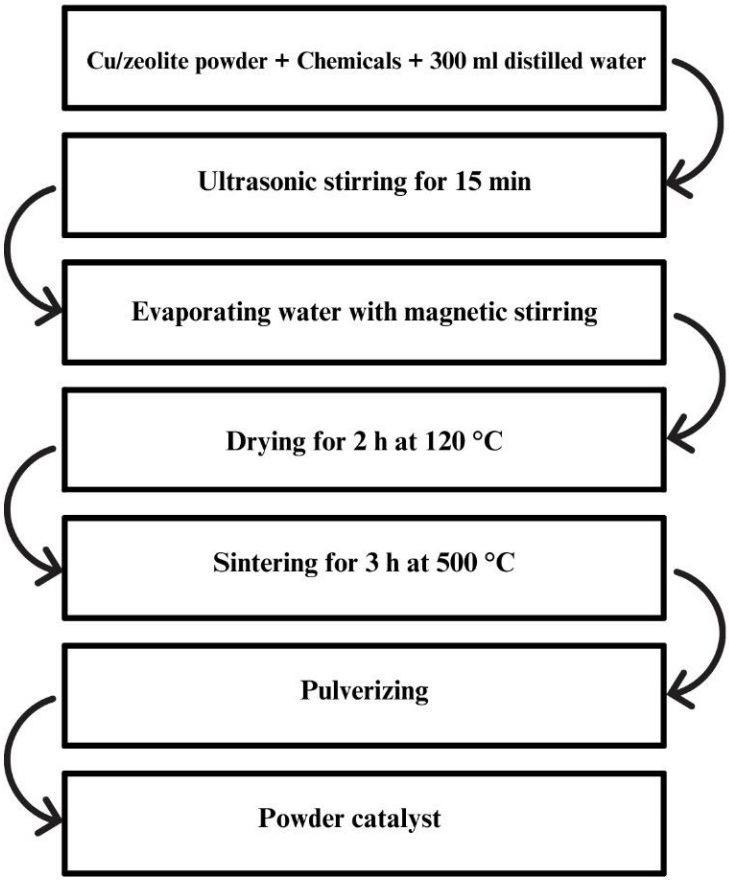

Figure 3.15. Powder catalyst preparation

In the process of catalyst powder preparation, Cu was utilized in the ion-exchange phase with two different types of zeolites. In the subsequent stage, cerium was added to enhance the durability of the catalyst, and samarium in varying proportions was employed to assess its effect on NO_x conversion activity. The table showing the material contents is provided below. Table 3.12 shows the percentage distribution of the materials contained in the catalyst powders prepared from a total of 50 grams, along with the abbreviations of the catalyst names. While creating the abbreviations, attention was paid to the percentage of samarium used and the type of zeolite applied.

Table 3.12. Chemical content and abbreviation for catalysts

SET-Y	**Sm**	**Ce**	**Cu**	**Zeolite Y (approx.)**	**Abbreviation**
Content (%)	0	0.3	4	96	Sm0-Y
	1	0.3	4	95	Sm1-Y
	2	0.3	4	94	Sm2-Y
	4	0.3	4	92	Sm4-Y
SET-Beta	**Sm**	**Ce**	**Cu**	**Zeolite Beta (approx.)**	**Abbreviation**
Content (%)	0	0.3	4	96	Sm0-BEA
	1	0.3	4	95	Sm1-BEA
	2	0.3	4	94	Sm2-BEA
	4	0.3	4	92	Sm4-BEA

After the production of the powder catalyst, colloidal silica equivalent to 10% of the weight of the obtained powder catalyst was used during the impregnation process onto the cordierite material to enhance adhesion. A total of three dipping processes were carried out. After each dipping process, an air gun was used to prevent the blockage of the pores in the cordierite structure, followed by a drying process for 1 h at 120 °C and then followed by 3 hours of calcination at 500°C. As a result of these procedures, the ratio of the impregnated cordierite weight to the unit volume of the catalyst was calculated. The results obtained from the calculations are presented in Table 3.13.

Table 3.13. Details of the loading status of the catalyst samples

Catalyst	The volume of the cordierite (L)	The bare weight of the cordierite (g)	Loaded Weight (g)	Loading (g)	Loading ratio (g/L)
Sm0-Y	0.215	81.65	88.43	6.78	31.5349
Sm1-Y	0.214	78.41	85.72	7.31	34.1589
Sm2-Y	0.213	79	86.38	7.38	34.6479
Sm4-Y	0.205	77.07	83.82	6.75	32.9268
Sm0-BEA	0.23	81.78	89.03	7.25	31.5217
Sm1-BEA	0.226	82.35	89.49	7.14	31.5929
Sm2-BEA	0.219	81.05	88.75	7.7	35.1598
Sm4-BEA	0.231	81.91	89.98	8.07	34.9351

Upon examining the table, it was determined that the loading ratio for all catalysts showed similarity and varied between approximately 31.5 and 35.2 g/L.

3.4. Catalyst Characterization

This section provides information on the instruments required for the characterization of catalysts and the conditions under which the analyses are conducted.

3.4.1. Scanning Electron Microscopy

Scanning Electron Microscopy (SEM) is a widely used technique for characterizing the surface morphology and composition of materials at the micro to nanometer scale. It operates by scanning a focused beam of high-energy electrons across the surface of a sample. The interaction between the electron beam and the sample produces various signals that provide detailed information about the sample's topography, composition, and other properties. SEM provides critical insights into the physical and chemical properties of materials, contributing to research and development in fields such as nanotechnology, materials science, and semiconductor fabrication.

SEM analysis was conducted at Çukurova University Central Research Laboratory (CUMERLAB) a device branded FEI Quanta 650 FEG (Figure 3.16). Analyses can be performed with the SEM device at magnifications ranging from 6x to 1000000x. This device allows for the analysis of samples that do not possess liquid properties. Non-conductive samples were made suitable for analysis by being coated with a very thin layer of conductive material (approximately 2 Å/second).

Figure 3.16. FEI Quanta 650 FEG

3.4.2. Energy Dispersive X-ray Spectroscopy

Energy Dispersive X-ray Spectroscopy (EDX or EDS) is an analytical technique used for the elemental characterization or chemical composition analysis of a sample. It is commonly integrated with SEM and relies on the interaction between the sample and an incident beam of electrons. When the electron beam strikes the surface of a sample, the atoms within the material are excited, causing inner-shell electrons to be ejected. This results in the formation of vacancies in the electron shells, and electrons from higher-energy outer shells drop down to fill these vacancies. During this process, the energy difference between the shells is released in the form of X-rays. These characteristic X-rays are specific to each element, making it possible to identify the elements present in the sample. Thanks to the EDX detector SEM device can generate maps that display how various elements are distributed across the surface of a sample. The same device used for SEM was also utilized to perform this analysis (Figure 3.16).

3.4.3. X-ray Diffraction

X-ray Diffraction (XRD) is an analytical technique used to determine the crystalline structure, phase composition, and physical properties of materials. XRD is based on the principle that each crystalline phase diffracts X-rays in a characteristic pattern according to its unique atomic

arrangement. These diffraction patterns serve as a “fingerprint” identifying the specific crystal phase. XRD is a non-destructive analytical technique, allowing for the analysis of even very small quantities of samples without causing any damage.

XRD analysis was conducted using a PANalytical Empyrean device at Çukurova University Central Research Laboratory (CUMERLAB) (Figure 3.17). The technical specifications are tabulated in Table 3.14.

Figure 3.17. PANalytical Empyrean XRD

Table 3.14. The technical specifications of PANalytical Empyrean XRD

X-Ray Tube	Cu-Ka
Operating Voltage Range	20 – 50 kV
Operating Current Range	5 – 60 mA
Goniometer Diameter	480 mm
Smallest Size of Step	0.00010 ($\theta/2\theta$)
Goniometer Scanning Speed	0.0001° / min and 70° / min
Angle to Angle Passing Speed	500°/min
Maximum Available Measuring Angles	-111°< 2θ <168°
Maximum Counting Capacity	1x106 signals/sec
Sensor	Pixel-based high-speed detector
Minimum Pixel Area	70 micron x 70 micron
Mapping	2D
Optical Module	Bragg-Brentano
Collimator	Cross Slit

3.4.4. Fourier-Transform Infrared

Fourier Transform Infrared (FT-IR) spectrum is a spectroscopy technique used to identify the chemical composition of a substance. The FT-IR spectrum analyzes the interaction of infrared light with the substance. This spectrum shows the absorbed or transmitted light at different

wavelengths (typically expressed in terms of wavenumber) and provides information about the functional groups in the substance. Especially common for organic compounds, the FT-IR spectrum is based on the vibrational energies of bonds within molecules. Each chemical bond vibrates at a specific frequency, and these vibrations are detected by the FT-IR instrument, appearing as peaks (absorption maxima) in the spectrum. Each peak corresponds to a specific type of bond or functional group.

FT-IR analysis was conducted using a PerkinElmer MID Spectrum Two UATR device at the Advanced Technology Education Research and Application Center (MEİTAM) of Mersin University (Figure 3.18). The technical specifications are presented in Table 3.15.

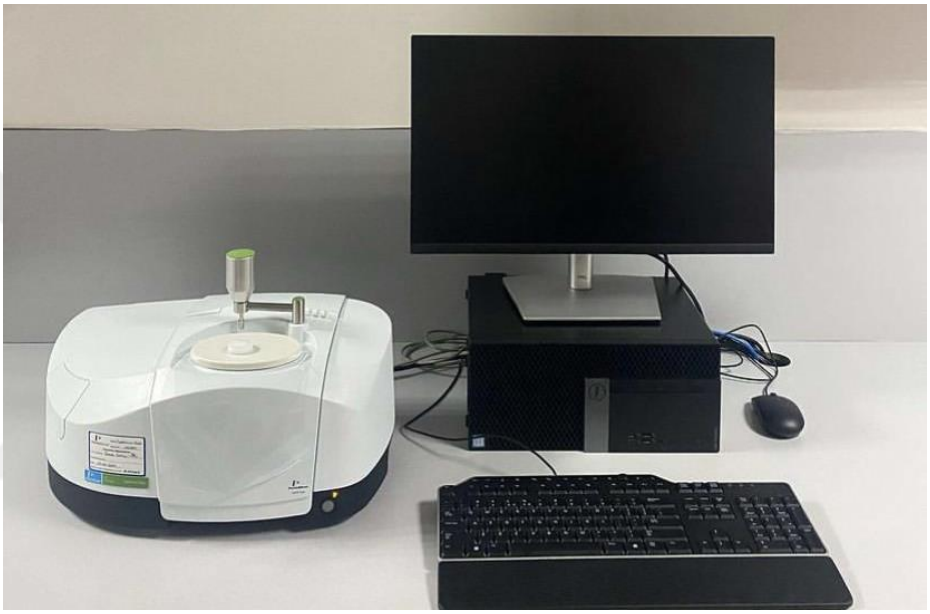

Figure 3.18. Perkin Elmer/MID Spectrum Two/UATR

Table 3.15. The technical specifications of Perkin Elmer/MID Spectrum Two/UATR

Operating range	5 – 45 °C
Wave length	8
Wave length range	8300 – 350 cm^{-1}
Depth x height x width	300 x 210 x 450 mm
Weight	13 kg

3.4.5. Brunauer-Emmet-Teller

The Brunauer-Emmett-Teller (BET) method is widely used for measuring materials' surface area, particularly porous solids. It is based on the physical adsorption of gas molecules on a solid surface and provides valuable insights into the texture and porosity of the material.

BET analysis was conducted using a Micromeritics TriStar II device at the Advanced Technology Education Research and Application Center (MEİTAM) of Mersin University (Figure 3.19). The technical specifications are presented in Table 3.16.

Figure 3.19. Micromeritics TriStar II

Table 3.16. The technical specifications of Micromeritics TriStar II

Pressure Measurement	
Absolute	Range: 0 to 950 mmHg Resolution: Within 0.05 mmHg Accuracy: Within 0.1% of full scale
Relative	P/P_o range: 0 to 1.0 P/P_o Resolution: < 10^{-4}
Analysis	
Specific surface area	From 0.01 m^2/g
Total surface area	From 0.1 m^2
Pore volume	From 4 × 10^{-6} cm^3/g
Operating Environment	
Temperature	10 to 35 °C, operating
Humidity	20 to 80 % relative, non-condensing
Depth x height x width	510 x 740 x 400 mm
Weight	37 kg

3.5. Experimental Test Setup

Performance tests were performed using the SCR test system located in the Motor Laboratory of the Automotive Engineering Department at Çukurova University. A schematic representation of the test system is provided in Figure 3.20. A part of the test setup is also shown in Figure 3.21. Equation 3.1 was used to calculate NO_x conversion efficiency.

$$NO_x\ conversion\ efficiency\ (\%) = \left(\frac{NO_{x,in} - NO_{x,out}}{NO_{x,in}}\right) x100 \quad (3.1)$$

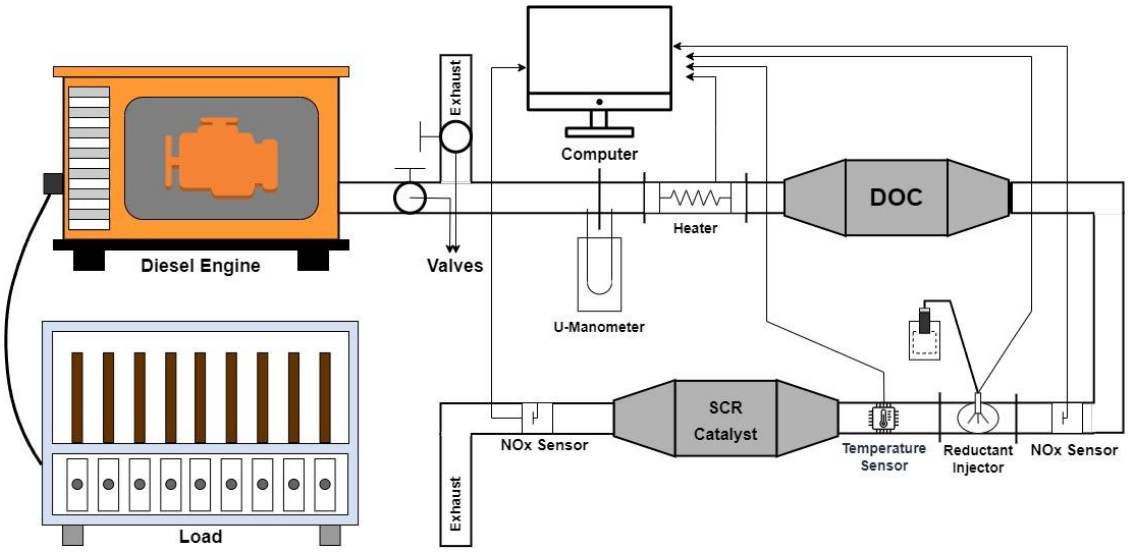

Figure 3.20. SCR test system

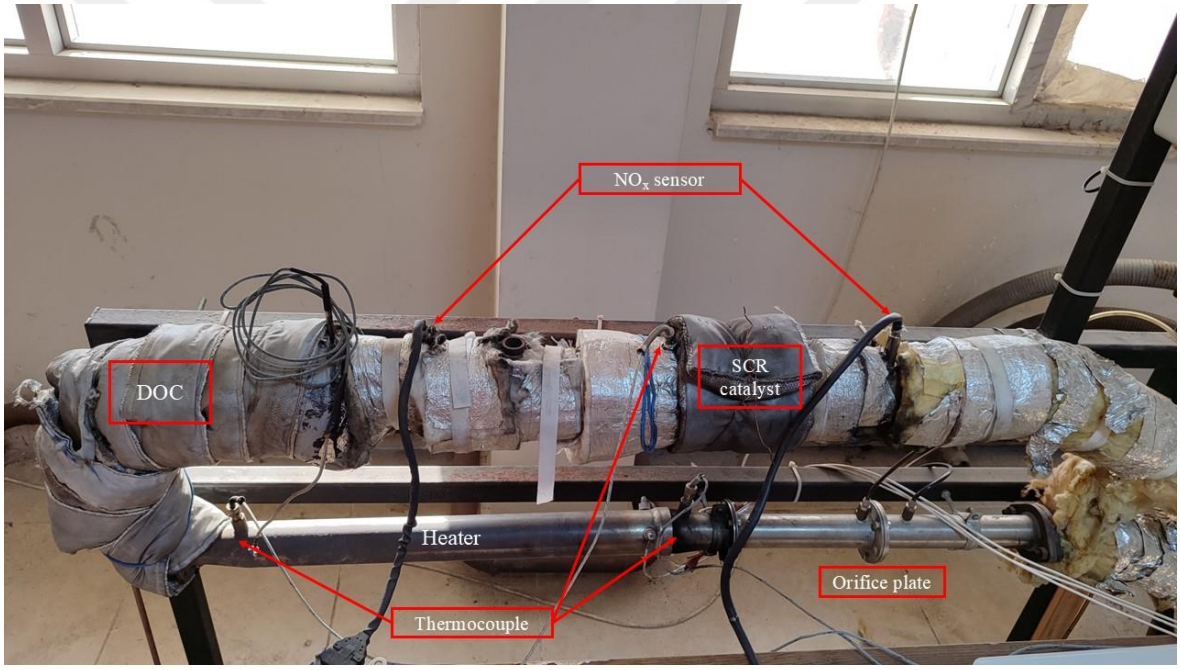

Figure 3.21. Picture of SCR setup

3.5.1. Diesel Engine

Exhaust gas samples used to investigate the NO_x reduction efficiency of SCR catalysts were obtained from an AKSA A2CRX08 brand two-cylinder V-type diesel engine. The appearance of the test engine operating at a constant speed of 3000 rpm is shown in Figure 3.22. The technical specifications of the engine are listed in Table 3.17.

Figure 3.22. Diesel engine

Table 3.17. The technical specifications of the diesel engine

Motor model	A2CRX08
Motor type	V
Number of cylinders	2
Bore / stroke	80 mm / 79 mm
Cylinder volume	0.794 L
Suction air flow rate	1 m^3/min
Exhaust gas flow rate	2.07 m^3/min
Compression ratio	23:1
Speed	3000 rpm
Prime power	9.6 kW
Fuel consumption	4 L/h
Cooling type	Water
Weight	250 kg

3.5.2. Loading Unit

Since the NO_x concentration in the exhaust gas varies under different loads, the tests were conducted at no load as well as under 2 kW and 4 kW loads. The loading unit consists of 10 resistors, each providing 1 kW of load. A visual representation of the loading unit is shown in Figure 3.23. The power drawn by the system from the engine was monitored using an ammeter and voltmeter installed on the system.

Figure 3.23. Loading unit

3.5.3. NO_x sensor

In the experiments, two NO_x sensors were integrated into the emission test system. The first sensor was located upstream of the SCR catalyst, while the second was positioned downstream. The first sensor measured NO_x emissions before reductant injection, and the second measured NO_x emissions after the catalyst, following reductant injection. The CANBUS J1939 protocol is used in the sensor communication system. Figure 3.24 illustrates the Continental UniNO_x sensor used in the experiments

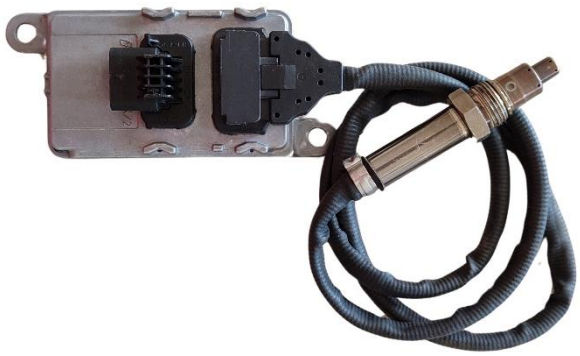

Figure 3.24.Continental UniNOx sensor

3.5.4. Temperature sensor

Figure 3.25 displays the K-type thermocouple used in the SCR system. This thermocouple allows for temperature measurements ranging from -200°C to 1370°C.

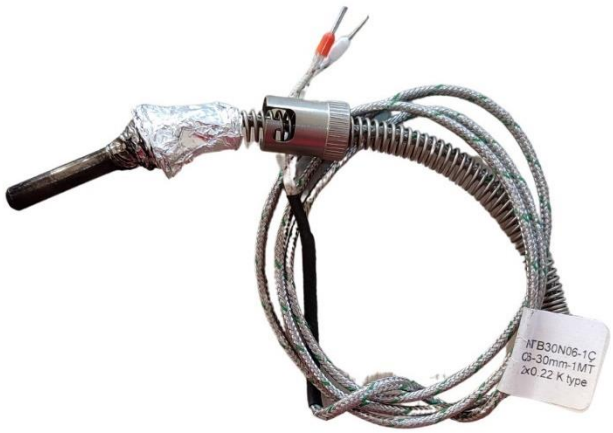

Figure 3.25. K-type thermocouple

3.5.5. Electronic control unit

The electronic control module is composed of several subcomponents integrated together, as illustrated in Figure 3.26. An Arduino Due microcontroller was employed in the system, along with a CANBUS Shield module compatible with the Arduino Due for reading data from the NO_x sensors. Additionally, an SRD-05VDC-SL-C module was used to regulate pump flow, a pulse width modulation (PWM) driver module to control the reductant spray rate, and a MAX6675 module to read thermocouple data. The technical details of the Arduino Due are provided in Table 3.18 below.

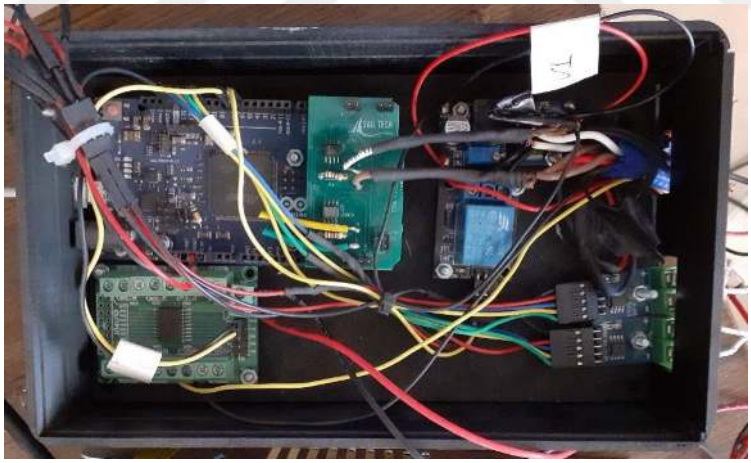

Figure 3.26. Electronic control unit

Table 3.18. The technical details of electronic control unit

Microcontroller	AT91SAM3X8E
Operating voltage	+3.3 V DC
Recommended input voltage	7 – 12 V DC
Input voltage limit	6 – 20 V
Digital in / out pins	54
Analog input/ output pins	12 / 12
Total DC output current over All I/O	130 mA
DC current for 3.3 V pin	800 mA
DC current for 5 V pins	800 A
Flash memory	512 kB
SRAM	96 kB (two parts: 64 KB and 32 KB)

3.5.6. Control panel of the exhaust gas heater

To examine the effects of low temperature on catalyst performance, tests were conducted within a temperature range of 150 °C to 240 °C. The control panel, shown in Figure 3.27, was used to adjust the exhaust gas temperature to the desired level.

Figure 3.27. Exhaust gas heater control panel

3.5.7. Reductant pump and solenoid valve

The reductant is delivered to the injection chamber via a pump and solenoid valve. A gasoline vehicle fuel pump, operating at a pressure of 3-3.5 bar, was used as the reductant pump. A multi-point fuel injector (with six holes), commonly used in gasoline vehicles, served as the solenoid valve for spraying the reductant.

3.5.8. Manometer and orifice plate

The space velocity is regulated using a U-tube manometer connected to the orifice. The orifice has a measurement range between 10000 h^{-1} and 50000 h^{-1}. The section where the orifice plate is positioned is shown in Figures 3.20 and 3.21.

3.5.9. Control program computer screen

The software interface was developed using C++ and Node.js programming languages. Figure 3.28 displays the interface that shows the NO_x values obtained in the SCR system, along with parameters such as temperature, injection duration, and frequency.

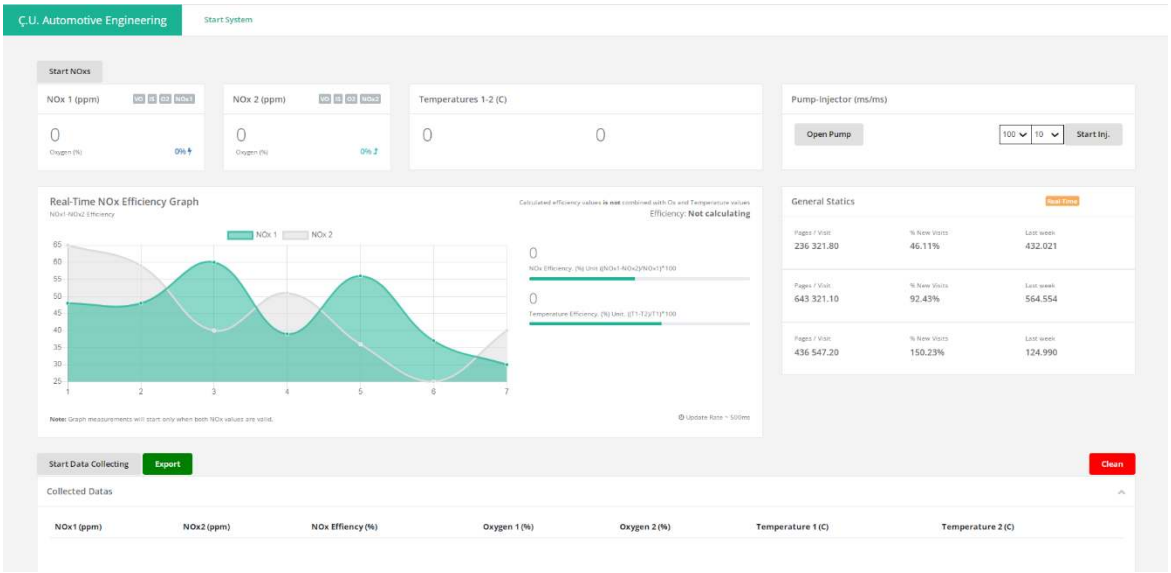

Figure 3.28. Software interface

4. RESULTS AND DISCUSSIONS

In this section, the findings from SEM, EDS, XRD, FT-IR, and BET analyses have been thoroughly examined, followed by a presentation of the NO_x conversion efficiencies.

4.1. SEM analysis

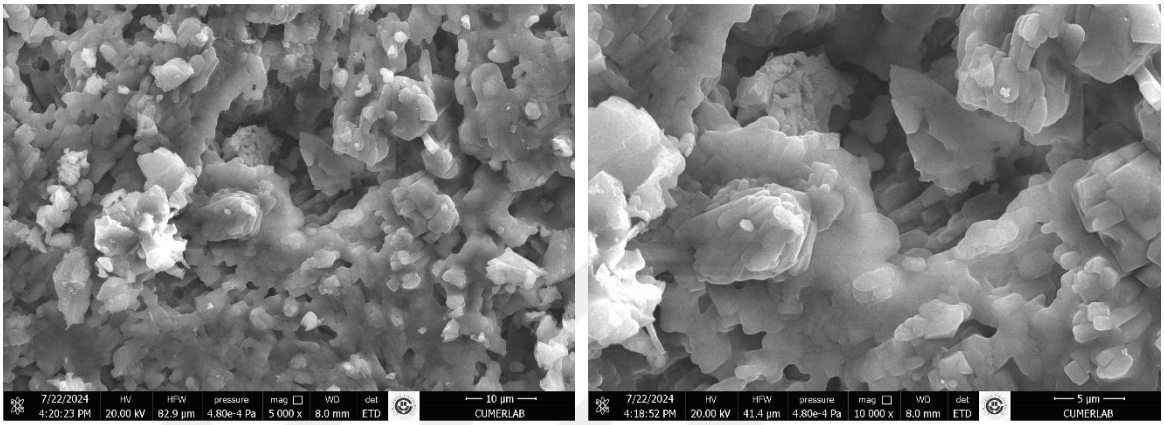

5000x 10000x

Figure 4.1. Bare cordierite

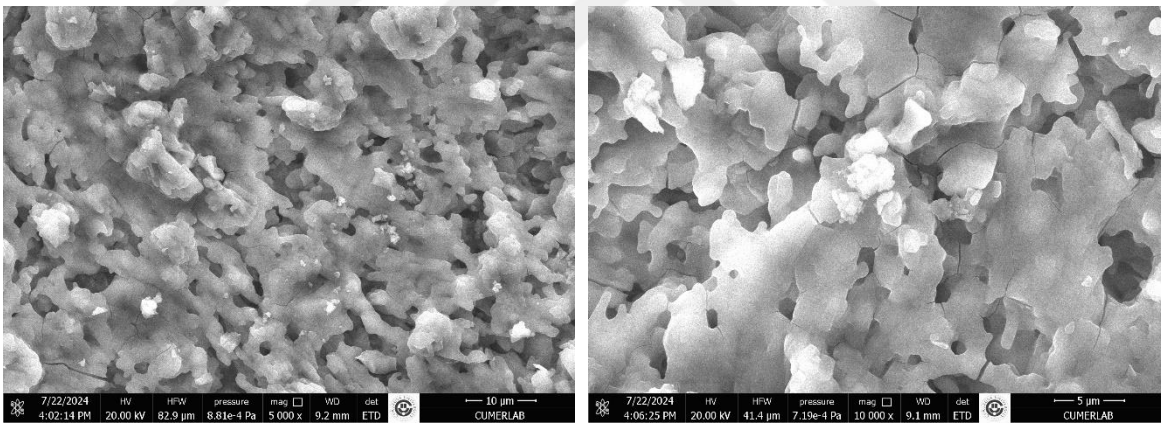

5000x 10000x

Figure 4.2. Acid-treated cordierite

The surface morphologies of bare and acid-treated cordierite samples are presented in Figures 4.1 and 4.2 through SEM images at magnifications of 5000x and 10000x. Upon examination of the SEM images following the acid treatment process (Figure 4.2), the formation of cracks on the surface of the cordierite structure is evident. These cracks, resulting from the acid treatment, clearly contribute to an increase in the surface area of the cordierite. This enhancement in specific surface area could improve catalyst production by providing more active sites and promoting a more uniform distribution of active components across the surface.

Table 4.1. EDS results of uncoated cordierite samples

Element	EDS-Bare			EDS-Acid-treated		
	Weight (%)	**Atomic (%)**	**Net Int.**	**Weight (%)**	**Atomic (%)**	**Net Int.**
O	43.3	56.35	3395.96	49.71	62.91	3149.31
Mg	8.56	7.33	1950.22	4.58	3.81	755.19
Al	20.78	16.04	4884.83	10.71	8.04	1995.17
Si	27.36	20.28	5626.03	35	25.24	6397.89

Upon examining Table 4.1, it is observed that the elemental composition of the acid-treated cordierite changes both in terms of weight and atomic percentage. Due to the inherent nature of the cordierite structure, the proportions of O and Si increase, while the proportions of Mg and Al decrease following the acid treatment.

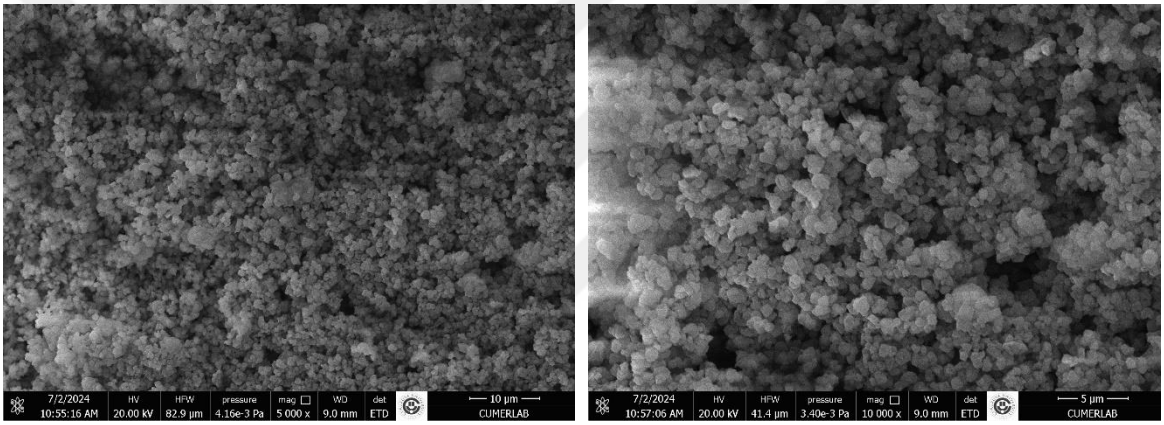

5000x 10000x

Figure 4.3. Sm0-Y

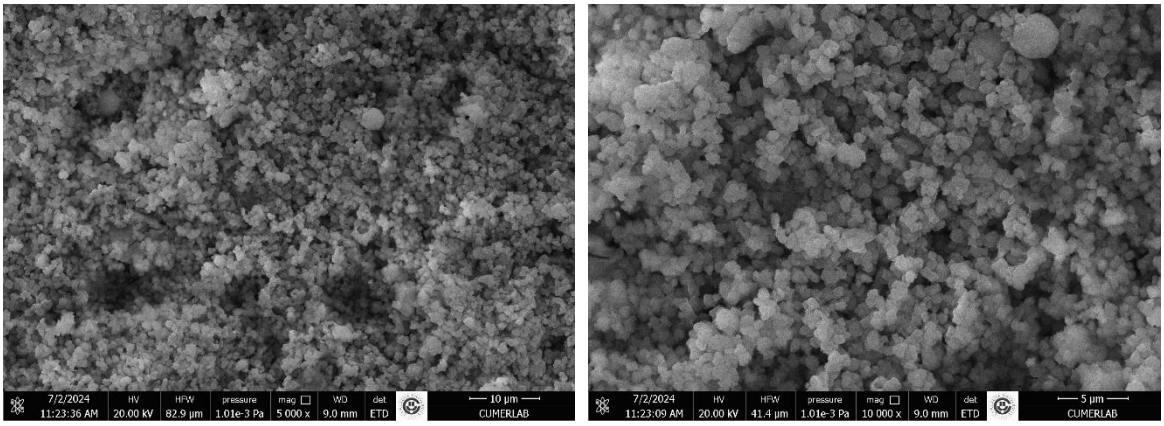

5000x 10000x

Figure 4.4. Sm1-Y

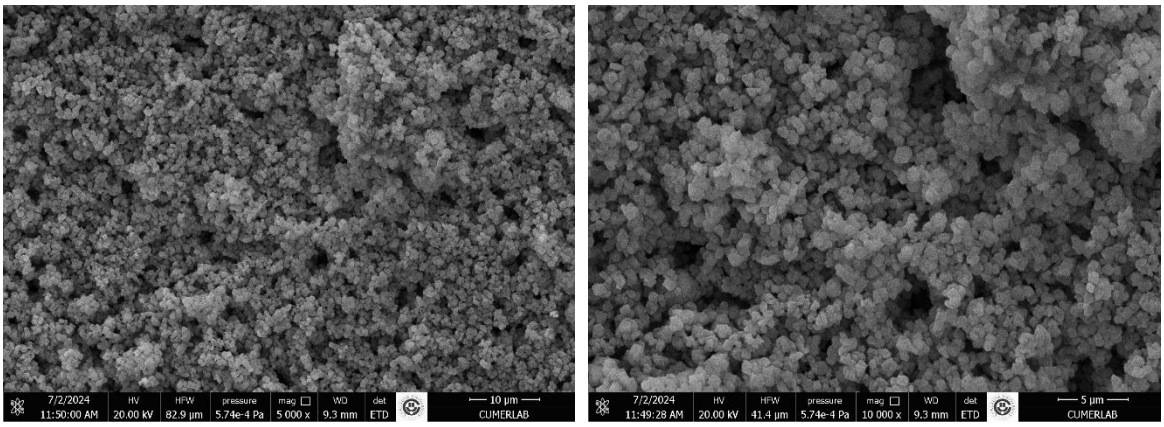

5000x 10000x

Figure 4.5. Sm2-Y

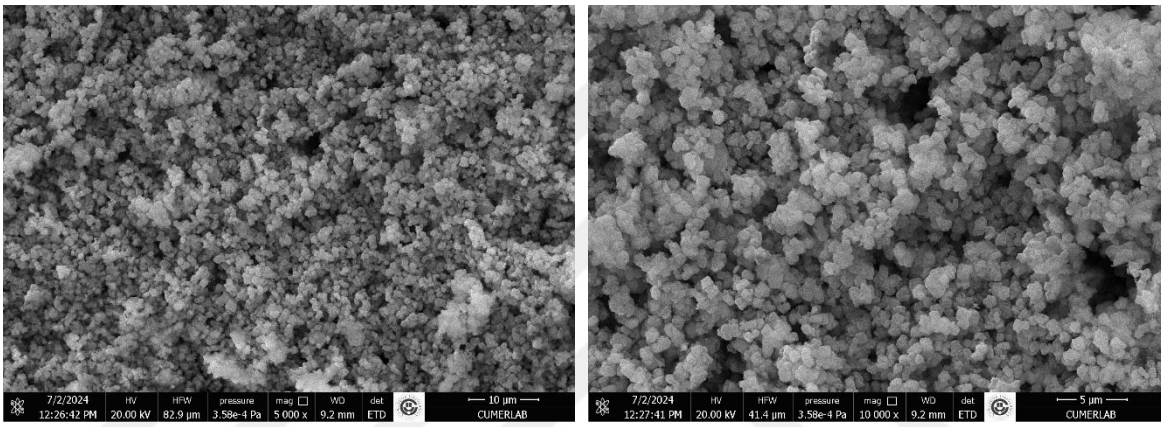

5000x 10000x

Figure 4.6. Sm4-Y

Figures 4.3 to 4.6 present SEM images of the set-in which Y zeolite was used as a support material. Upon examining the images taken at 5000x and 10000x magnifications, it is evident that a uniform distribution has occurred on the surface morphology. Additionally, the cracks and pores formed after acid treatment are effectively covered by the powder catalyst.

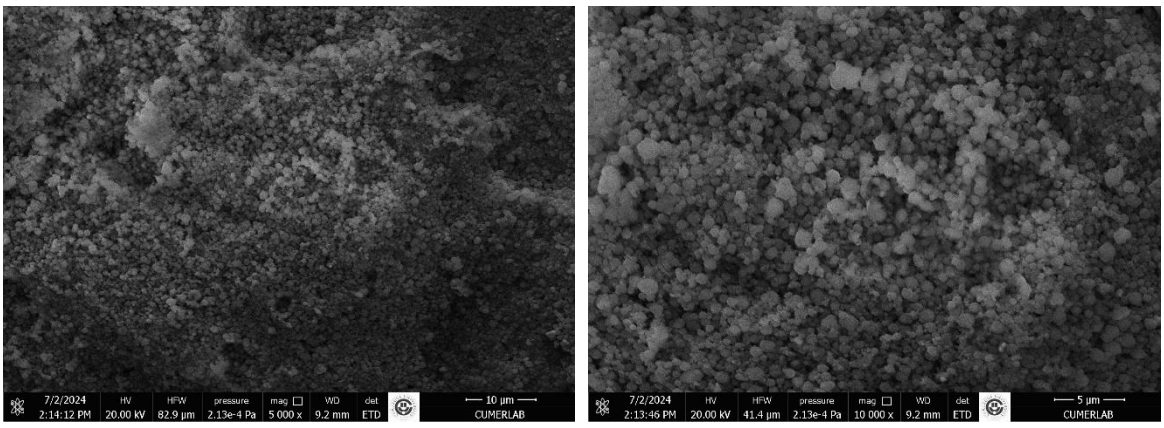

5000x 10000x

Figure 4.7. Sm0-BEA

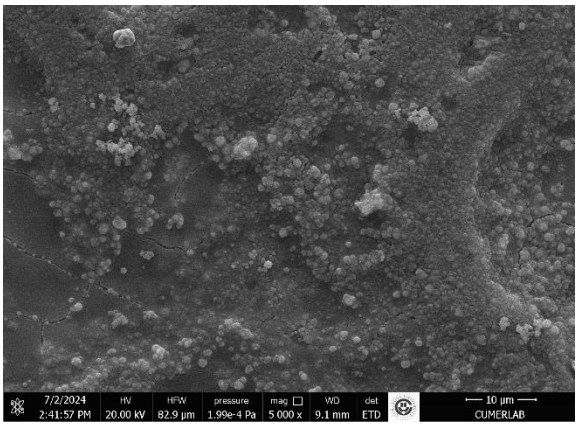

5000x

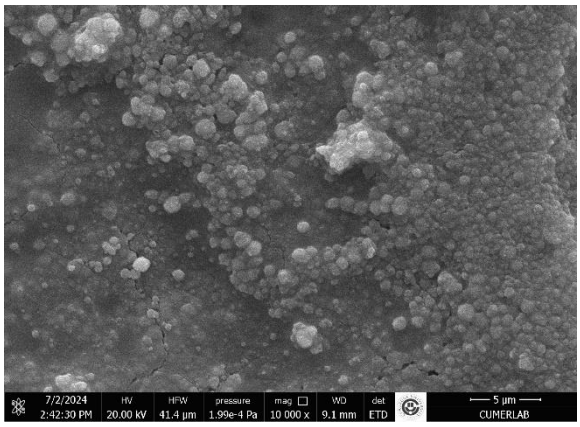

10000x

Figure 4.8. Sm1-BEA

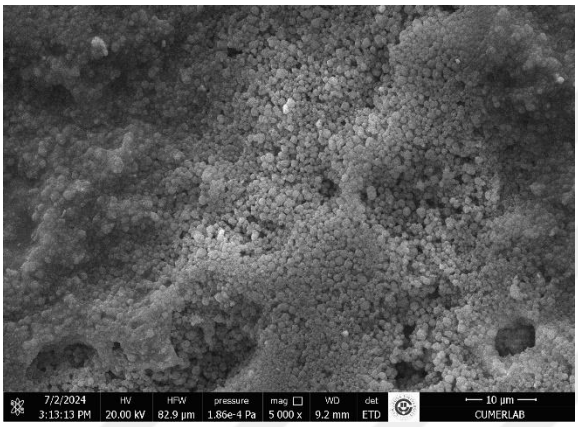

5000x

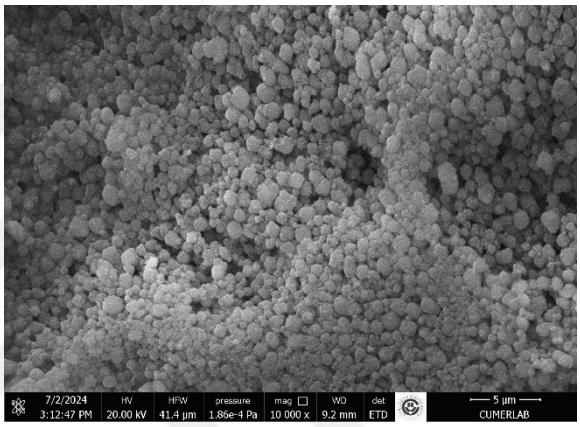

10000x

Figure 4.9. Sm2-BEA

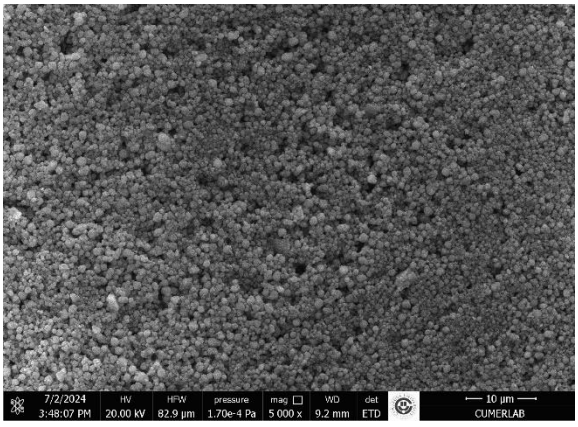

5000x

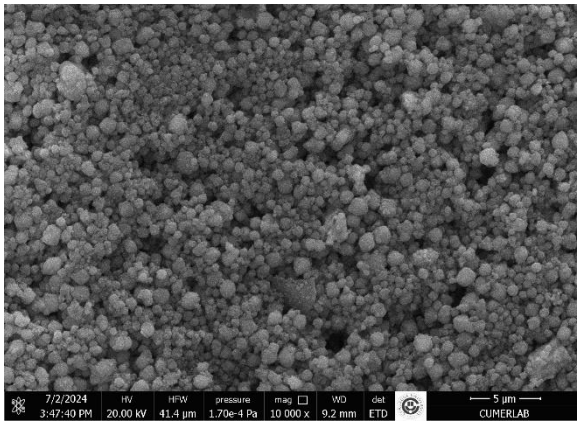

10000x

Figure 4.10. Sm4-BEA

Figures 4.7 to 4.10 present SEM images of the set-in which Beta zeolite was used as a support material. Upon examining the images at 5000x and 10000x magnifications, a uniform distribution on the surface morphology is again observed. However, these images appear darker, and the materials on the surface exhibit a more compact structure compared to the Y zeolite set. Additionally, the

cracks and pores formed after acid treatment are tightly covered by the powder catalyst, further contributing to the dense appearance.

4.2. EDS mapping analysis

Elemental analysis was performed using EDS mapping in the SEM device. EDS analyses were conducted on a selected region of the SEM images at 500x magnification. Figures 4.11 through 4.14 present the images belonging to the Y zeolite set, while Figures 4.15 through 4.18 show the images of the Beta zeolite set. In addition, quantitative analysis was performed on the same regions using the same device. The values for the Y zeolite set are presented in Tables 4.2 through 4.5, while the values for the Beta zeolite set are provided in Tables 4.6 through 4.9.

Upon examining Figure 4.11, it can be observed that oxygen (O), magnesium (Mg), aluminum (Al), and silicon (Si), which constitute the content of cordierite, are homogeneously distributed across the surface and pores. It is also observed that the dominant colors are red, yellow, and navy blue, which correspond to O, Si, and Al (Figure 11.b). These elements are more prominent on the catalyst surface. When the Y zeolite, which also contains the same elements due to its structure, is analyzed proportionally, these elements are found to be present at higher concentrations. It has been determined that the Cu elements, which are expected to exhibit catalytic activity as a result of the coating, have penetrated the surface and pores, displaying a homogeneous distribution. The values presented in Table 4.2, which contain the quantitative analysis data, are consistent with the mapping images provided for the Sm0-Y catalyst.

The EDS mapping images for the Sm1-Y catalyst are presented in Figure 4.12. In these images, in addition to O, Mg, Al, and Si elements found in the structure of cordierite and zeolite, the Sm, Cu, and Ce elements used in the coating are also observed. The Sm and Cu elements, which are expected to exhibit catalytic activity, are homogeneously distributed across the surface and pores. The values presented in Table 4.3, which contain the quantitative analysis data, are consistent with the mapping images provided for the Sm1-Y catalyst.

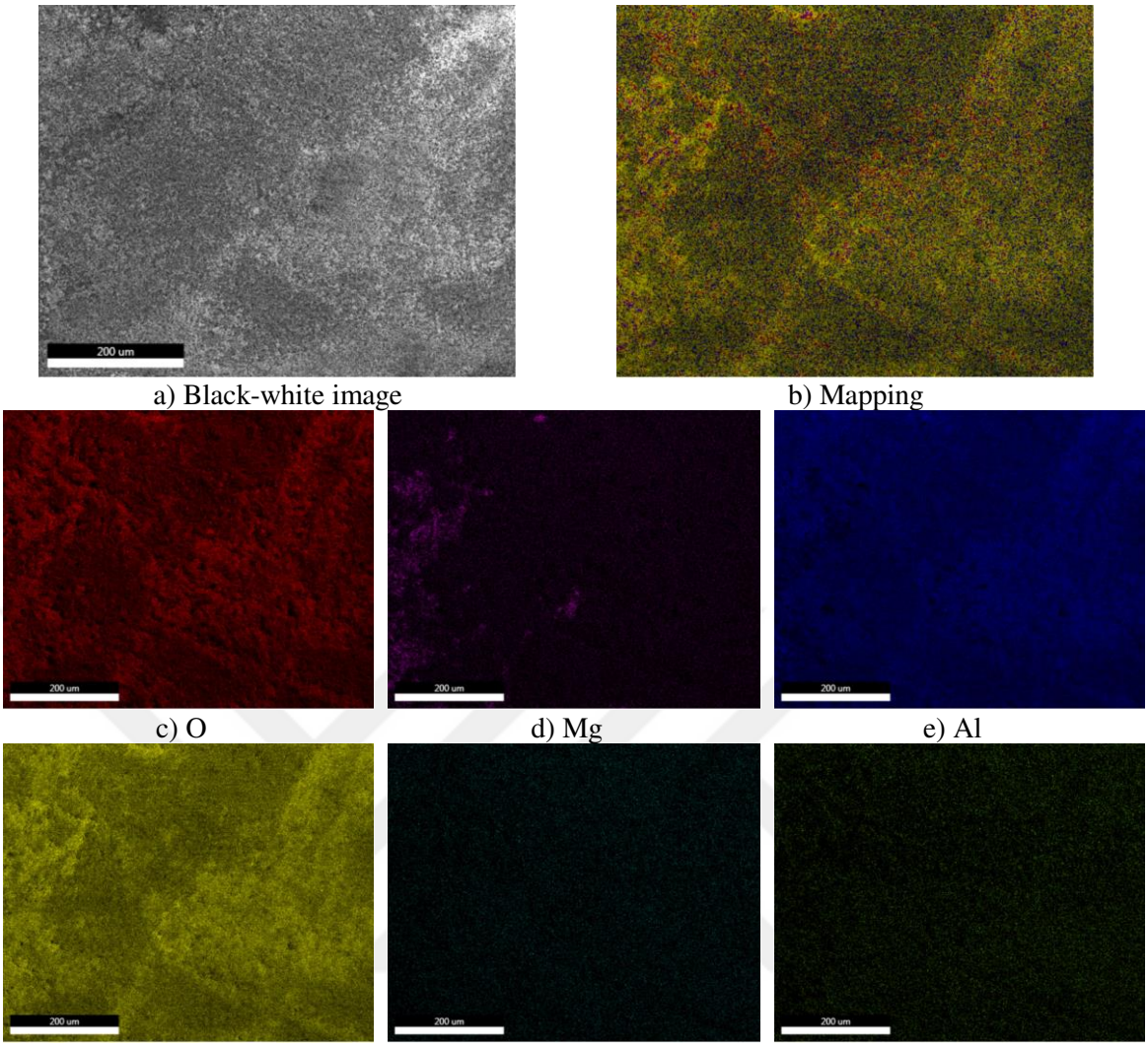

a) Black-white image b) Mapping

c) O d) Mg e) Al

f) Si g) Ce h) Cu

*23% O, 3% Mg, 19% Al, 49% Si, 3% Ce, 2% Cu

Figure 4.11. EDS Mapping images of Sm0-Y

Table 4.2. Sm0-Y quant results

Element	Sm0-Y		
	Weight (%)	**Atomic (%)**	**Net Int.**
O	43.5	61.79	3049.5
Ce	9.53	1.54	56.86
Cu	4.07	1.46	157.89
Mg	0.91	0.85	126.4
Al	11.35	9.56	1956.64
Si	30.65	24.8	5455.65

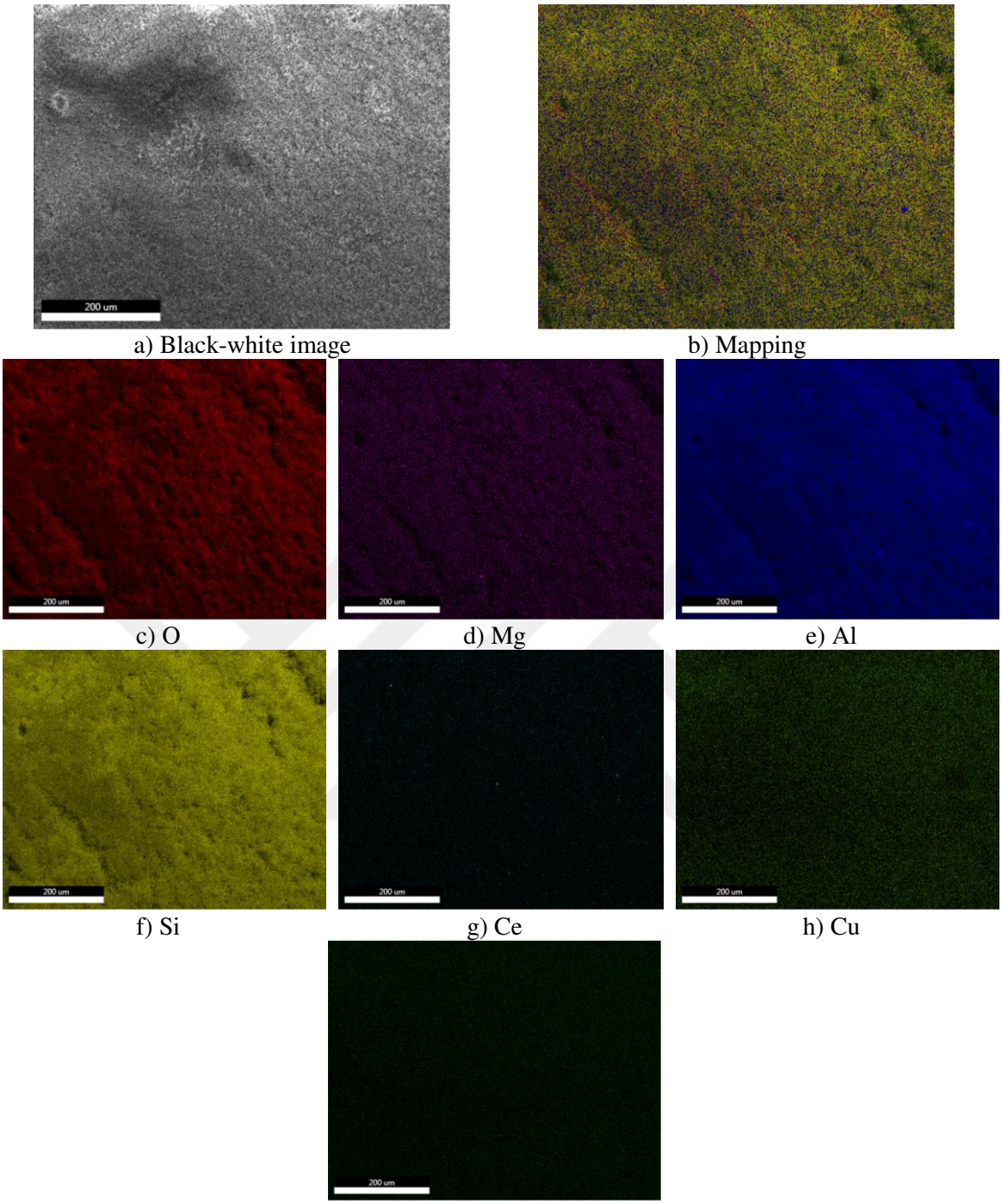

a) Black-white image b) Mapping

c) O d) Mg e) Al

f) Si g) Ce h) Cu

i) Sm

*18% O, 2% Mg, 20% Al, 52% Si, 2% Ce, 3% Cu, 3% Sm

Figure 4.12. EDS Mapping images of Sm1-Y

Figure 4.13 presents the EDS mapping images for the Sm2-Y catalyst. In these images, it can be observed that both the elements used in the coating process and those present in the structure of cordierite are homogeneously distributed across the surface and pores. It was also determined that the Si element, which is part of the structure of cordierite and zeolite, has a high concentration in the

Sm2-Y catalyst, as in all other catalysts. The values presented in Table 4.4, which contain the quantitative analysis data, are consistent with the mapping images provided for the Sm2-Y catalyst.

Table 4.3. Sm1-Y quant results

Element	Sm1-Y		
	Weight (%)	**Atomic (%)**	**Net Int.**
O	49.3	63.8	4015.98
Ce	0.1	0.01	5.15
Cu	1.9	0.62	103.18
Mg	0.27	0.23	53.96
Al	12.04	9.24	2933.41
Si	35.19	25.94	8231.84
Sm	1.21	0.17	53.72

Table 4.4. Sm2-Y quant results

Element	Sm2-Y		
	Weight (%)	**Atomic (%)**	**Net Int.**
O	52.93	66.95	4065.14
Ce	0.12	0.02	5.67
Cu	0.72	0.23	35.25
Mg	0.11	0.1	20.35
Al	11.45	8.59	2495.12
Si	33.19	23.92	6998.05
Sm	1.47	0.2	57.9

The EDS mapping images for the Sm4-Y catalyst are shown in Figure 4.14. These images reveal that the elements used in the coating process, as well as those naturally present in the structure of cordierite, are uniformly distributed across the surface and pores. Additionally, the Si element, which is a component of both cordierite and zeolite, is found in high concentrations within the Sm4-Y catalyst, similar to the other catalysts. The quantitative analysis values in Table 4.5 align with the mapping images for the Sm4-Y catalyst.

Table 4.5. Sm4-Y quant results

Element	Sm4-Y		
	Weight (%)	**Atomic (%)**	**Net Int.**
O	47.15	63.91	4573.63
Ce	0.34	0.05	21.8
Cu	2.25	0.77	137.1
Mg	0.19	0.17	39.5
Al	10.77	8.65	2774.22
Si	33.1	25.56	8519.9
Sm	6.19	0.89	308.29

When Tables 4.2 through 4.5 are considered overall, a quantitative increase in the amount of Sm is consistently observed. This indicates that the catalyst production method has been successfully implemented as intended.

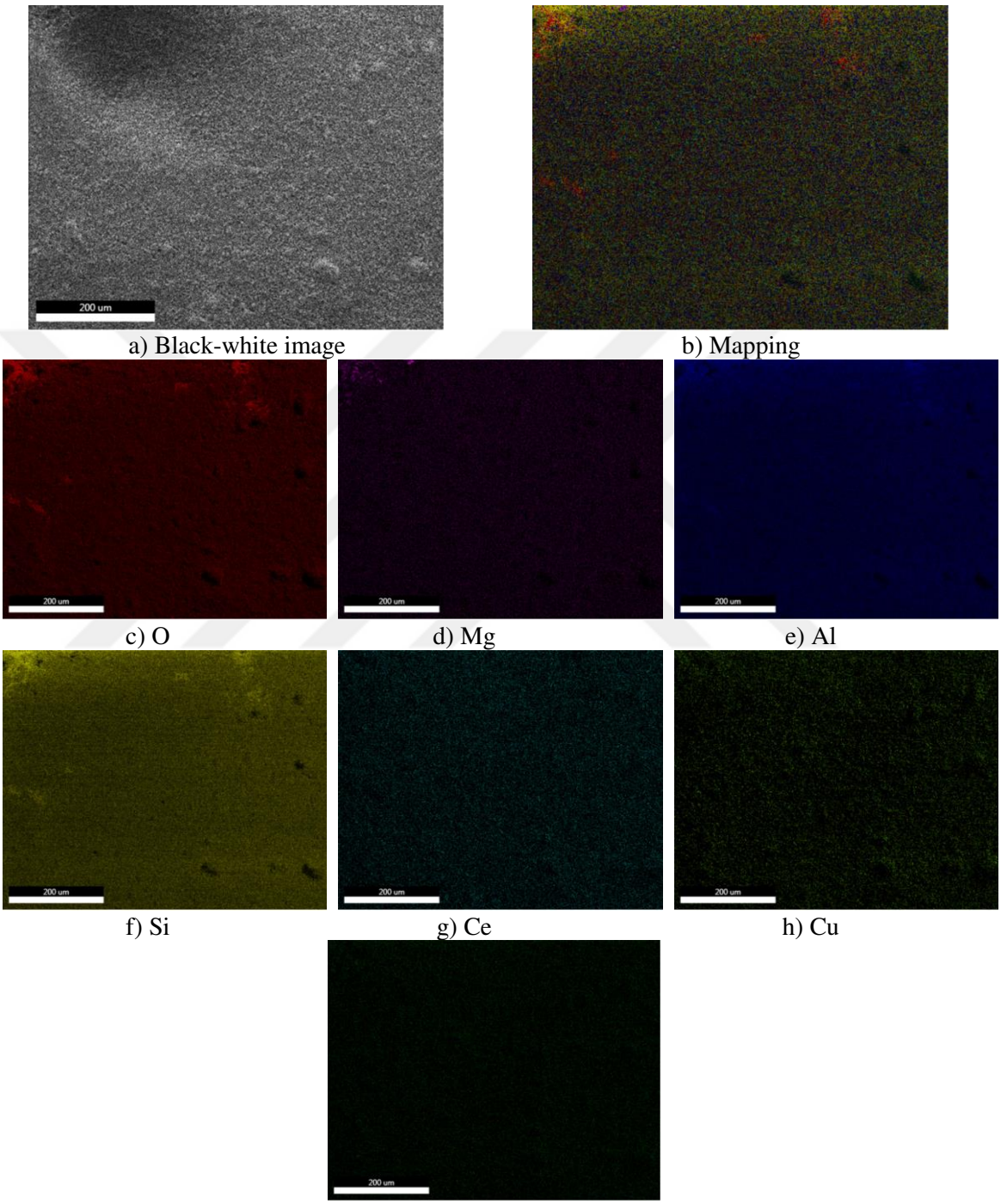

a) Black-white image b) Mapping

c) O d) Mg e) Al

f) Si g) Ce h) Cu

i) Sm

*26% O, 5% Mg, 20% Al, 37% Si, 4% Ce, 3% Cu, 4% Sm

Figure 4.13. EDS Mapping images of Sm2-Y

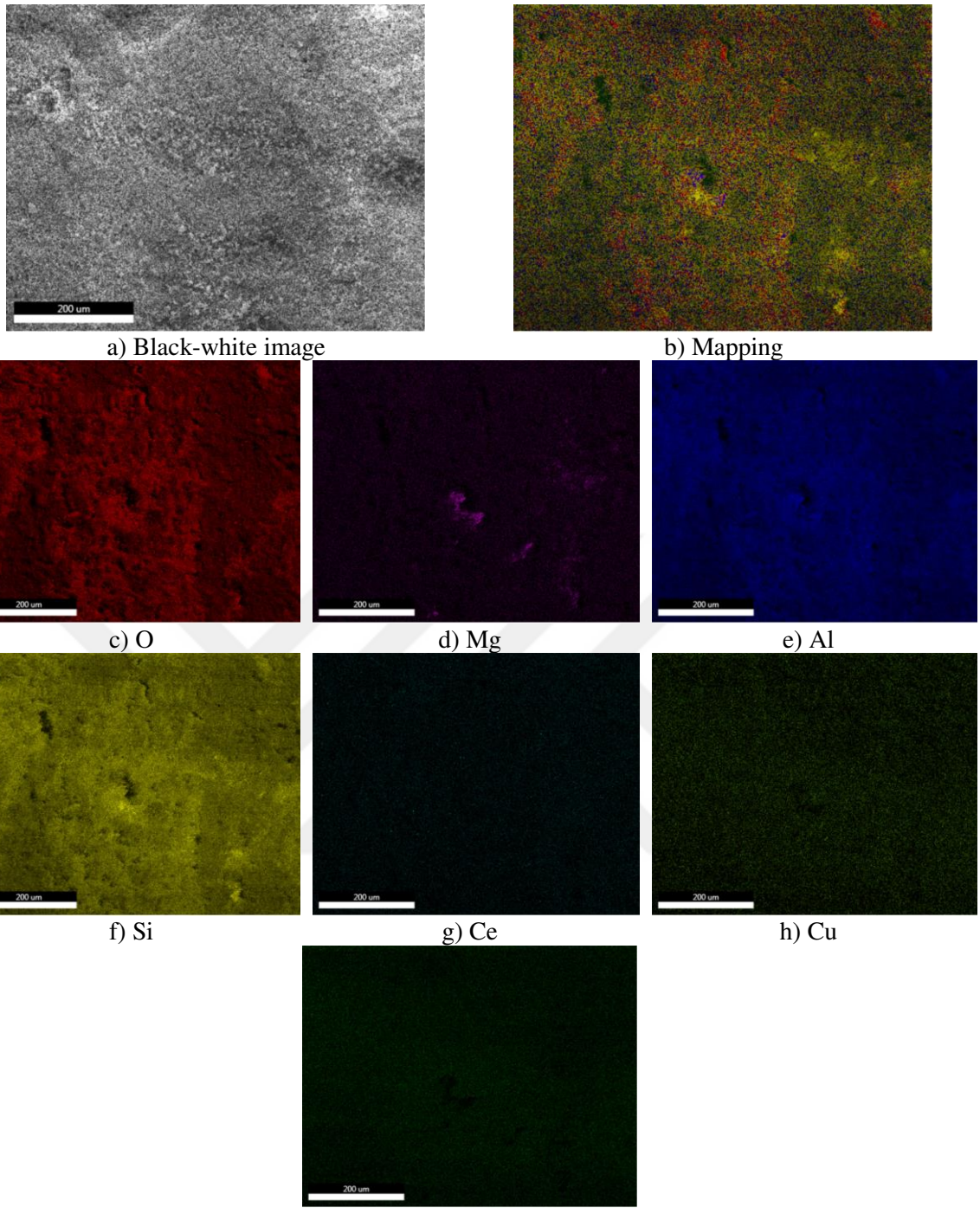

a) Black-white image b) Mapping

c) O d) Mg e) Al

f) Si g) Ce h) Cu

i) Sm

*22% O, 3% Mg, 18% Al, 48% Si, 3% Ce, 3% Cu, 4% Sm

Figure 4.14. EDS Mapping images of Sm4-Y

Upon examining Figure 4.15, it can be observed that O, Mg, Al, and Si, which constitute the content of cordierite, are homogeneously distributed across the surface and pores. It is also observed that the dominant colors are red, yellow, and navy blue, which correspond to O, Si, and Al (Figure 15.b). These elements are more prominent on the catalyst surface. When the Beta zeolite, which also contains the same elements due to its structure, is analyzed proportionally, these elements are found to be present at higher concentrations. It has been determined that the Cu elements, which are

expected to exhibit catalytic activity as a result of the coating, have penetrated the surface and pores, displaying a homogeneous distribution. The values presented in Table 4.6, which contain the quantitative analysis data, are consistent with the mapping images provided for the Sm0-BEA catalyst.

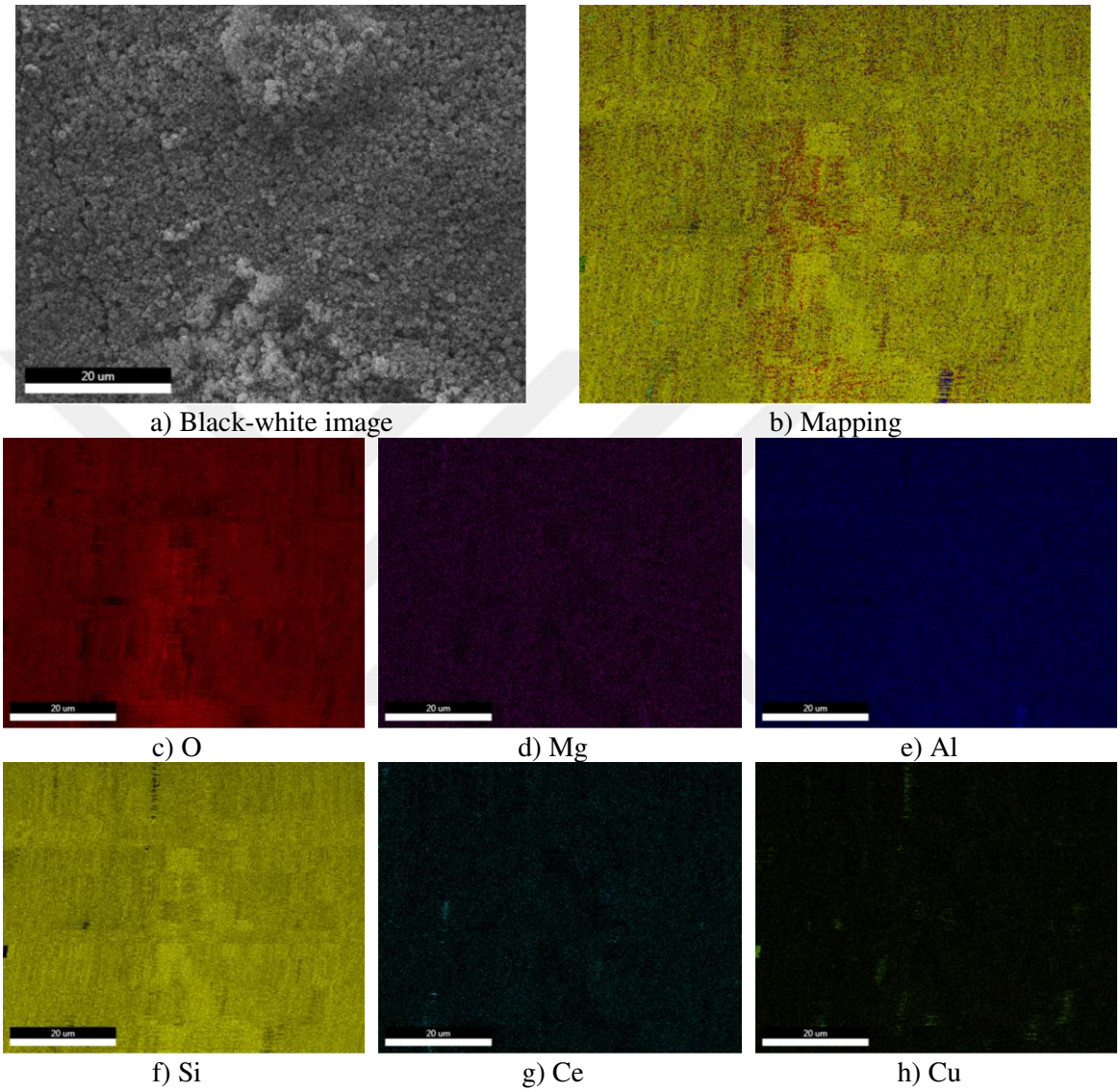

a) Black-white image b) Mapping

c) O d) Mg e) Al

f) Si g) Ce h) Cu

*21% O, 2% Mg, 5% Al, 69% Si, 1% Ce, 2% Cu

Figure 4.15. EDS Mapping images of Sm0-BEA

Table 4.6. Sm0-BEA quant results

Element	Sm0-BEA		
	Weight (%)	Atomic (%)	Net Int.
O	55.72	69.16	4974.85
Ce	0.26	0.04	14.7
Cu	1.08	0.34	62.52
Mg	0.36	0.29	72.71
Al	2.37	1.74	604.12
Si	40.21	28.43	11126.15

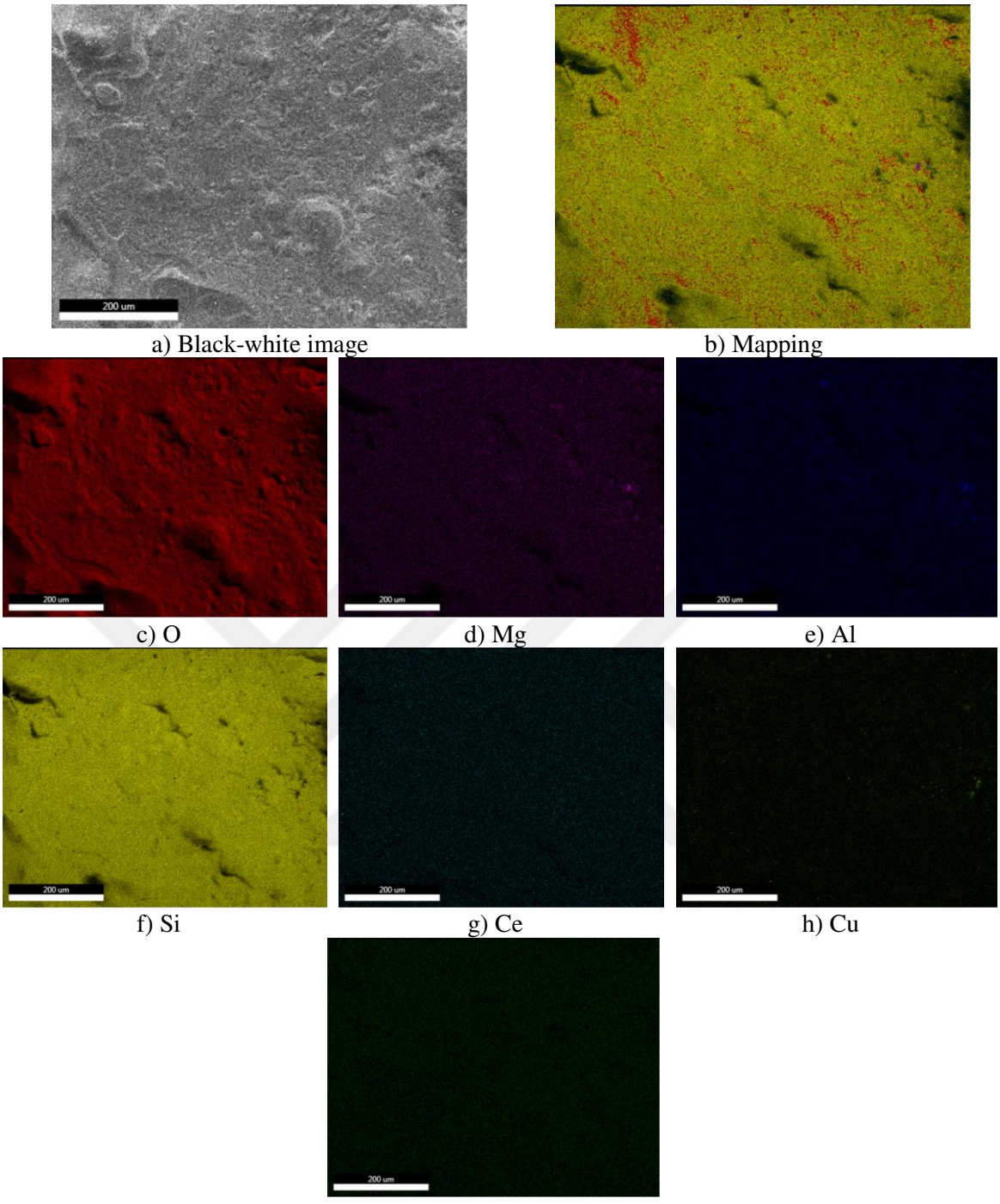

a) Black-white image b) Mapping

c) O d) Mg e) Al

f) Si g) Ce h) Cu

i) Sm

*16% O, 2% Mg, 4% Al, 70% Si, 2% Ce, 3% Cu, 3% Sm

Figure 4.16. EDS Mapping images of Sm1-BEA

Figure 4.16 presents the EDS mapping images for the Sm1-BEA catalyst. In these images, along with the O, Mg, Al, and Si elements that are part of the cordierite and zeolite structure, the Sm, Cu, and Ce elements used in the coating are also visible. The Sm and Cu elements, expected to provide catalytic activity, are uniformly distributed across the surface and pores. The quantitative analysis data provided in Table 4.7 correspond well with the mapping images of the Sm1-BEA catalyst, demonstrating a clear alignment between the two sets of data.

Table 4.7. Sm1-BEA

Element	Sm1-BEA		
	Weight (%)	**Atomic (%)**	**Net Int.**
O	50.57	65.2	4909.36
Ce	0.22	0.03	14.08
Cu	1.3	0.42	85.93
Mg	0.18	0.15	42.29
Al	1.96	1.5	580.55
Si	44.23	32.48	14247.61
Sm	1.55	0.21	81.91

The EDS mapping images for the Sm2-BEA catalyst are displayed in Figure 4.17. These images reveal that both the elements introduced during the coating process and those inherent to the cordierite structure are uniformly distributed across the surface and within the pores. Additionally, it has been observed that the Si element, which is a key component of both cordierite and zeolite, exhibits a notably high concentration in the Sm2-BEA catalyst, similar to other catalysts. The quantitative analysis data presented in Table 4.8 align closely with the mapping images, confirming the consistency of the findings for the Sm2-BEA catalyst.

Table 4.8. Sm2-BEA

Element	Sm2-BEA		
	Weight (%)	**Atomic (%)**	**Net Int.**
O	46.38	61.28	3267.16
Ce	0.18	0.03	8.68
Cu	1.7	0.57	83.79
Mg	1.13	0.98	207.34
Al	4.2	3.29	931.93
Si	44.65	33.61	10486.53
Sm	1.76	0.57	70.21

Figure 4.18 displays the EDS mapping images for the Sm4-BEA catalyst, illustrating a uniform distribution of both the coating elements and those naturally present in the cordierite structure across the surface and pores. Furthermore, the Si element, a key constituent of both cordierite and zeolite, is observed to be present in high concentrations within the Sm4-BEA catalyst, consistent with the findings for other catalysts. The quantitative analysis data in Table 4.9 correspond well with the mapping images, indicating alignment between the two sets of results for the Sm4-Y catalyst.

Table 4.9. Sm4-BEA

Element	Sm4-BEA		
	Weight (%)	Atomic (%)	Net Int.
O	58.19	71.99	2890.98
Ce	0.37	0.05	10.95
Cu	0.6	0.19	17.87
Mg	0.5	0.41	51.16
Al	2.11	1.55	268.12
Si	36.27	25.56	5089.18
Sm	1.97	0.26	46.78

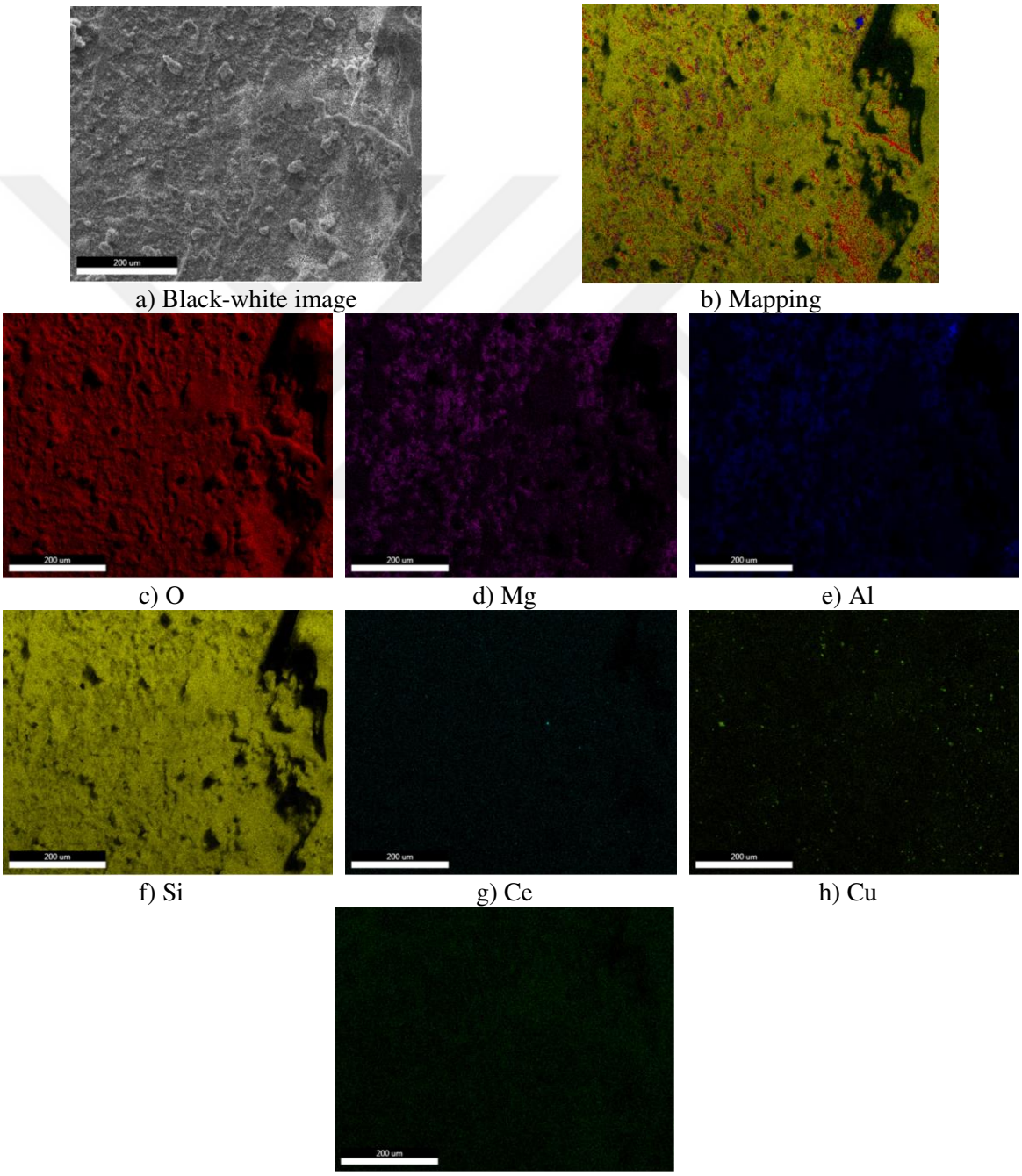

a) Black-white image b) Mapping

c) O d) Mg e) Al

f) Si g) Ce h) Cu

i) Sm

*15% O, 3% Mg, 8% Al, 60% Si, 4% Ce, 5% Cu, 5% Sm

Figure 4.17. EDS Mapping images of Sm2-BEA

Tables 4.6 through 4.9 reveals a consistent quantitative increase in the Sm content. This trend suggests that the catalyst production method was successfully executed according to the intended design.

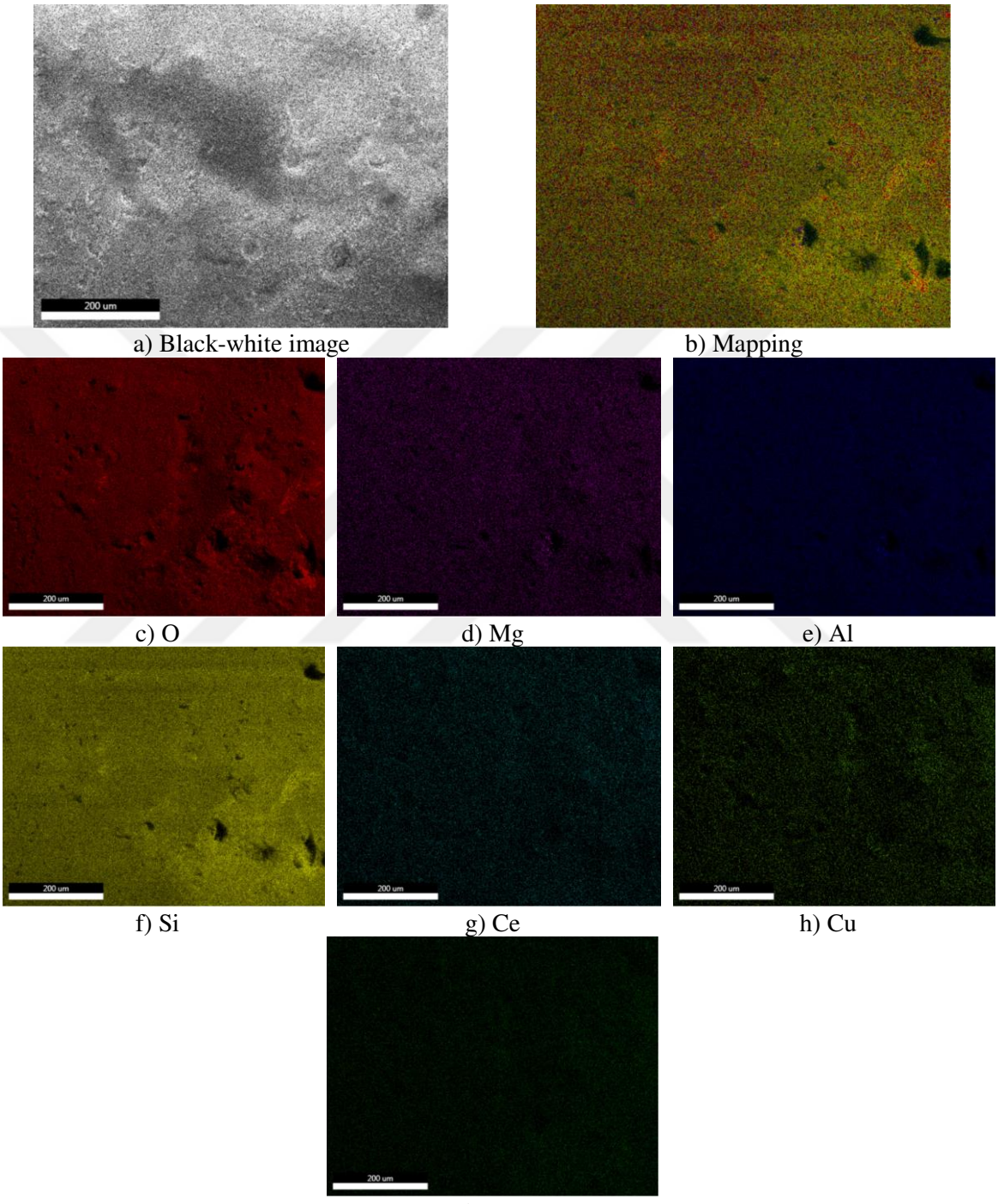

a) Black-white image b) Mapping

c) O d) Mg e) Al

f) Si g) Ce h) Cu

i) Sm

*24% O, 3% Mg, 6% Al, 56% Si, 3% Ce, 3% Cu, 4% Sm

Figure 4.18. EDS Mapping images of Sm4-BEA

4.3. XRD analysis

XRD analysis was conducted to examine the crystal structure of the materials. The XRD results for the synthesized catalyst samples are presented in Figures 4.19 to 4.26.

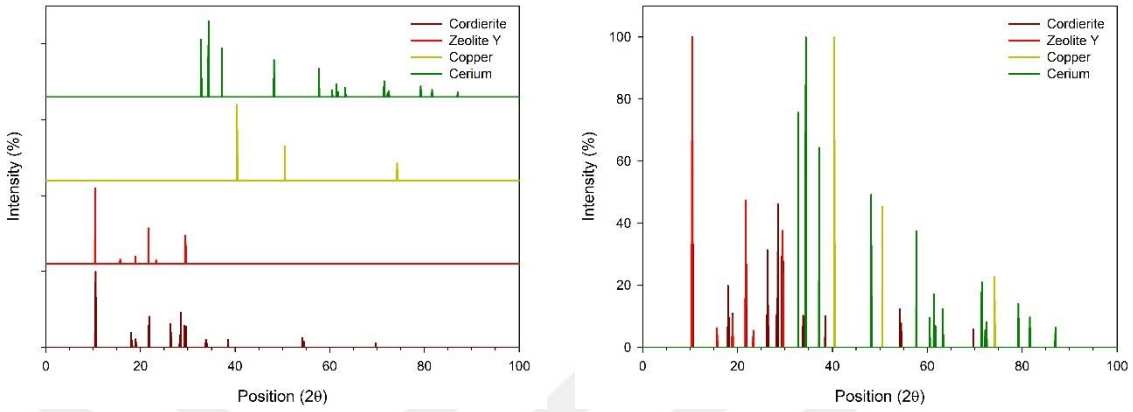

Figure 4.19. XRD analysis results of Sm0-Y; a) separated peaks, b) combined peaks.

Figure 4.19 displays the XRD results for the Sm0-Y catalyst sample. Among the observed peaks, cordierite ($Al_4Mg_2O_{18}Si_5$) and Ce exhibit an orthorhombic crystal structure, whereas Cu and zeolite Y display a cubic crystal structure. The XRD patterns reveal that zeolite Y exhibits the highest intensity, with strong peaks predominantly between 10° and 30°, indicating a highly ordered crystalline structure characterized by multiple symmetrical peaks in this range. Ce emerges as the second most prominent material, displaying intense peaks between 20° and 50°, suggesting the possible formation of cerium (IV) oxide (CeO_2), with additional peaks observed beyond 60°. Cu shows distinct peaks around 43° and 50°, indicative of its crystalline metallic form. Cordierite, in contrast, presents lower intensity peaks compared to zeolite Y and Ce, with its characteristic peaks spread between 10° and 40°, reflecting the typical structural features of cordierite.

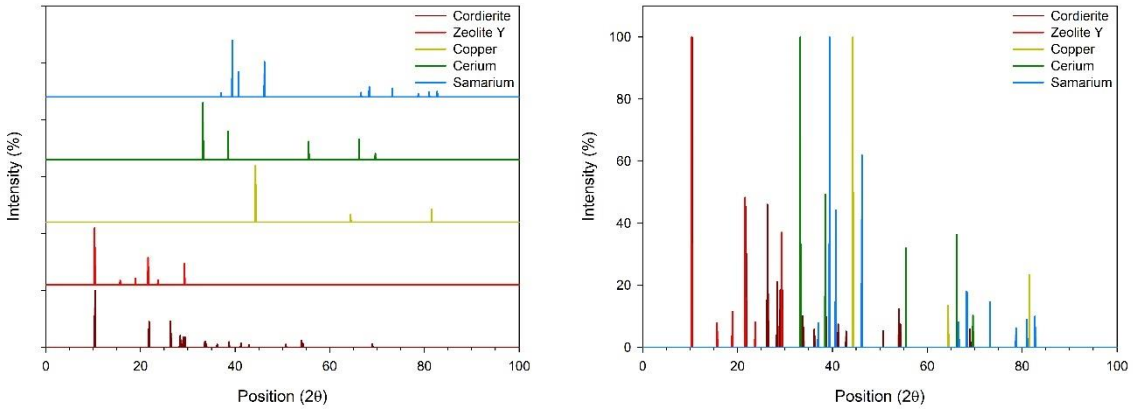

Figure 4.20. XRD analysis results of Sm1-Y; a) separated peaks, b) combined peaks.

Figure 4.20 presents the XRD results for the Sm1-Y catalyst sample. The analysis reveals that cordierite ($Al_4Fe_2O_{18}Si_5$) and Ce exhibit an orthorhombic crystal structure, while Cu and zeolite Y display a cubic crystal structure. Additionally, Sm is characterized by a hexagonal crystal structure. The XRD pattern shows similar structure with Sm0-Y that zeolite Y dominates the intensity profile with strong peaks between 10° and 30°, indicative of its highly ordered crystalline structure. Cerium displays notable peaks between 20° and 50°, along with smaller peaks beyond 60°, suggesting a CeO_2 phase. Cu exhibits characteristic peaks at around 43° and 50°, corresponding to its crystalline metallic form. Cordierite, though less intense, shows peaks between 10° and 40°, typical of its structural pattern. Samarium introduces additional peaks, particularly overlapping with the cerium and copper patterns, with significant peaks around 40° and several smaller ones extending towards higher angles, indicating a potential interaction or phase formation between these elements.

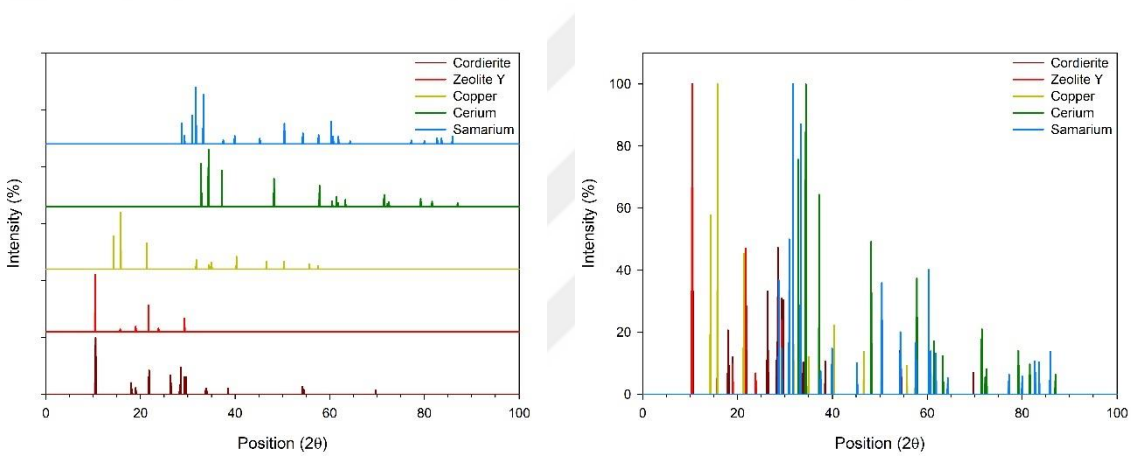

a) b)

Figure 4.21. XRD analysis results of Sm2-Y; a) separated peaks, b) combined peaks.

Figure 4.21 presents the XRD results for the Sm2-Y catalyst sample. The analysis indicates that cordierite ($Al_4Mg_2O_{18}Si_5$), Ce, and CuO_2 exhibit an orthorhombic crystal structure, while zeolite Y shows a cubic crystal structure. Furthermore, Sm is defined by a hexagonal crystal structure. When comparing the Figure 4.20 and Figure 4.21, the Sm2-Y sample clearly contains a higher concentration of Sm than the Sm1-Y sample, as indicated by the increased intensity of Sm characteristic peaks, particularly in the 30° to 50° range. In the Sm2-Y sample, Sm peaks dominate and overlap with those of other materials such as zeolite Y, cordierite, Cu, and Ce. While peak intensity of zeolite Y remains consistent across both samples, Sm greater presence in Sm2-Y suppresses the visibility of the other materials' patterns. Ce and Cu continue to show notable peaks around the 40° to 50° range, but the higher intensity of Sm in Sm2-Y suggests a stronger presence or interaction of Sm within the sample's crystalline structure. This increase in Sm content may also indicate changes in phase formation or integration with the other components compared to the Sm1-Y sample.

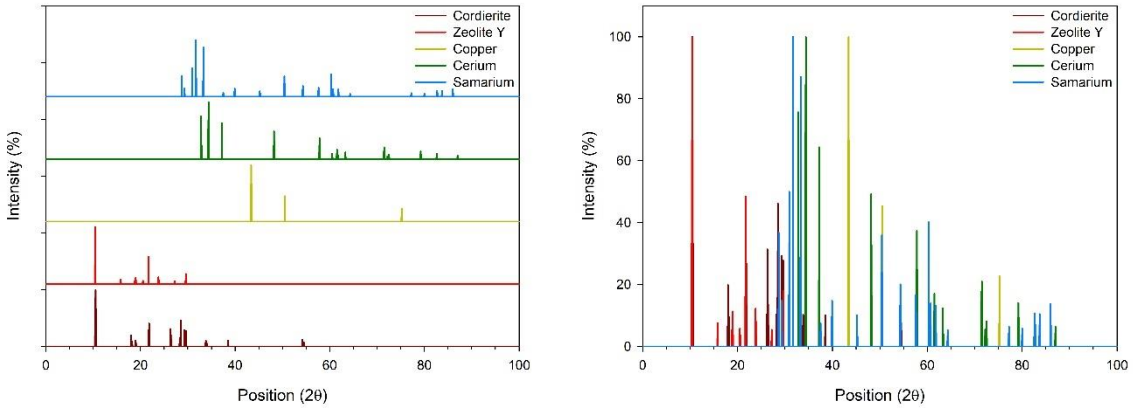

a) b)

Figure 4.22. XRD analysis results of Sm4-Y; a) separated peaks, b) combined peaks

Figure 4.22 displays the XRD results for the Sm4-Y catalyst sample. The analysis shows that cordierite ($Al_4Mg_2O_{18}Si_5$) and Ce have an orthorhombic crystal structure, whereas Cu and zeolite Y exhibit a cubic crystal structure. Furthermore, Sm is defined by its hexagonal crystal structure. In comparison, the main difference between Sm2-Y and Sm4-Y the two XRD patterns is the significantly higher Sm content in the Sm4-Y sample, as indicated by the stronger peaks between 30° and 50°. This higher concentration of Sm results in greater overlap with the peaks of other materials, such as zeolite Y, cordierite, Cu, and Ce, thereby reducing their visibility. In contrast, the Sm1-Y sample, with its lower Sm concentration, shows less overlap, allowing the characteristic peaks of zeolite Y, cordierite, Cu, and Ce to be more clearly distinguished. Overall, the increased Samarium content in Sm4-Y masks some of the features of the other materials, while Sm1-Y provides a clearer pattern for these components.

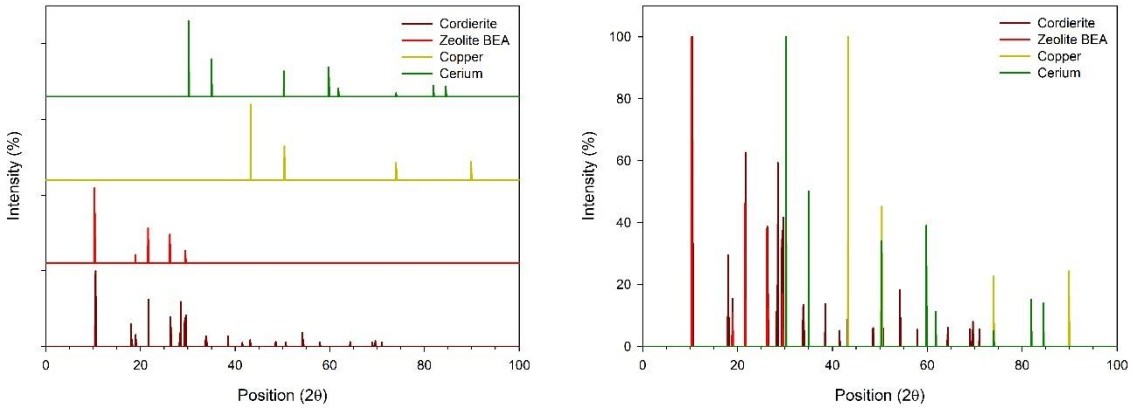

a) b)

Figure 4.23. XRD analysis results of Sm0-BEA; a) separated peaks, b) combined peaks

Figure 4.23 illustrates the XRD results for the Sm0-BEA catalyst sample, highlighting distinct crystal structures in the material. The orthorhombic cordierite phase ($Al_4Mg_2O_{18}Si_5$) is identified by characteristic diffraction peaks at 2θ ≈ 10.36°, 10.44°, 18.04°, 18.99°, 21.72°, 26.31°, 26.41°, 28.44°, 29.40°, 29.55°, 33.86°, 38.53°, and 54.16°.

Cubic Cu is indicated by prominent peaks at 2θ ≈ 43.29°, 50.42°, 74.07°, and 89.87°, while Ce also displays a cubic structure, with notable peaks observed at 2θ ≈ 30.19°, 35.00°, 50.00°, 59.82°, 81.90°, and 84.51°. Additionally, the tetragonal zeolite BEA phase is marked by prominent diffraction peaks at 2θ ≈ 10.28°, 18.85°, 21.58°, 26.22°, and 29.48°. These peaks confirm the coexistence of orthorhombic cordierite, cubic Cu and Ce, and tetragonal zeolite BEA within the Sm0-BEA catalyst structure, illustrating the complex crystalline composition of the sample.

The XRD analysis results for Cu-based zeolite BEA catalysts containing Sm are shown in Figures 4.24 to 4.26. These results confirm the presence of both orthorhombic crystal-structured cordierite ($Al_4Mg_2O_{18}Si_5$) and tetragonal crystal-structured zeolite BEA in the catalysts. The characteristic diffraction peaks for cordierite are observed at 2θ ≈ 10.44°, 18.05°, 18.99°, 21.73°, 26.32°, 28.47°, 29.61°, 33.79°, 38.54°, and 54.18°. For the Sm1-BEA and Sm4-BEA catalysts, distinct diffraction peaks corresponding to cubic copper (I) oxide (Cu_2O) and hexagonal Ce phases are present at 2θ ≈ 36.88°, 42.85°, 62.21°, and 74.57° for Cu_2O and 2θ ≈ 32.69°, 34.46°, 37.00°, 48.24°, 58.35°, 63.47°, 69.56°, and 71.19° for Ce. In the Sm2-BEA catalyst, cubic Cu and anorthic CeO_2 are identified, with notable diffraction peaks appearing at 2θ ≈ 43.04°, 50.12°, 73.60°, and 89.24° for Cu and 2θ ≈ 28.27°, 32.76°, 47.01°, and 55.77° for CeO_2. Moreover, all Sm-doped catalysts (Sm1-BEA, Sm2-BEA, and Sm4-BEA) exhibit prominent peaks indicating the presence of hexagonal Sm at 2θ ≈ 39.44°, 40.68°, 46.24°, 68.28°, 73.16°, and 82.66°. These findings reveal the crystalline phases and confirm the successful incorporation of Sm, Cu, and Ce structures within the BEA zeolite framework.

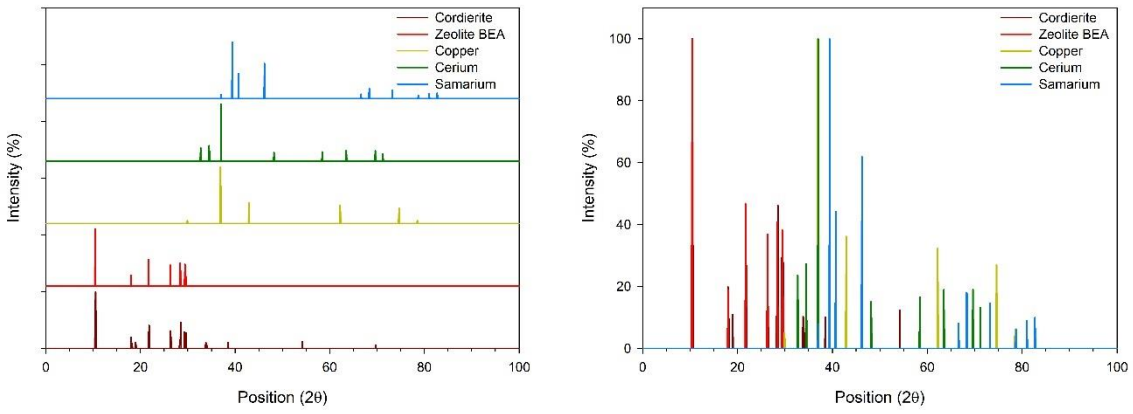

a) b)

Figure 4.24. XRD analysis results of Sm1-BEA; a) separated peaks, b) combined peaks

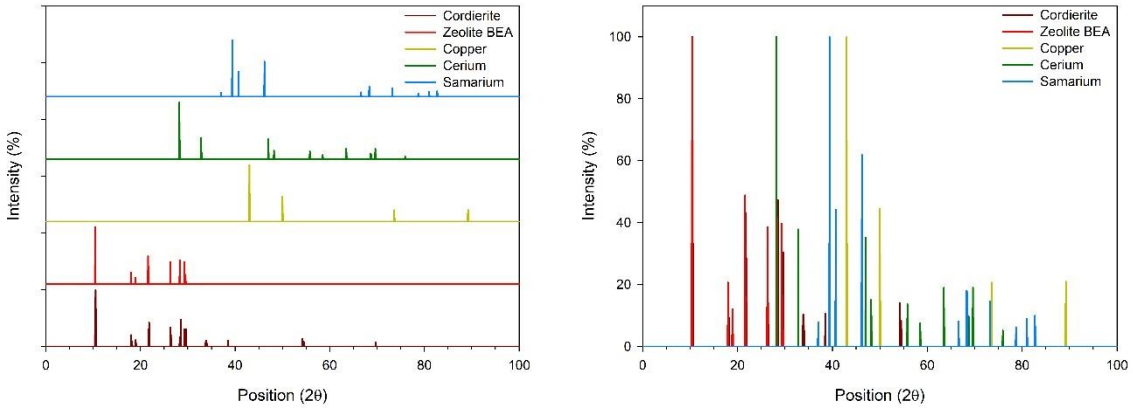

a) b)

Figure 4.25. XRD analysis results of Sm2-BEA; a) separated peaks, b) combined peaks

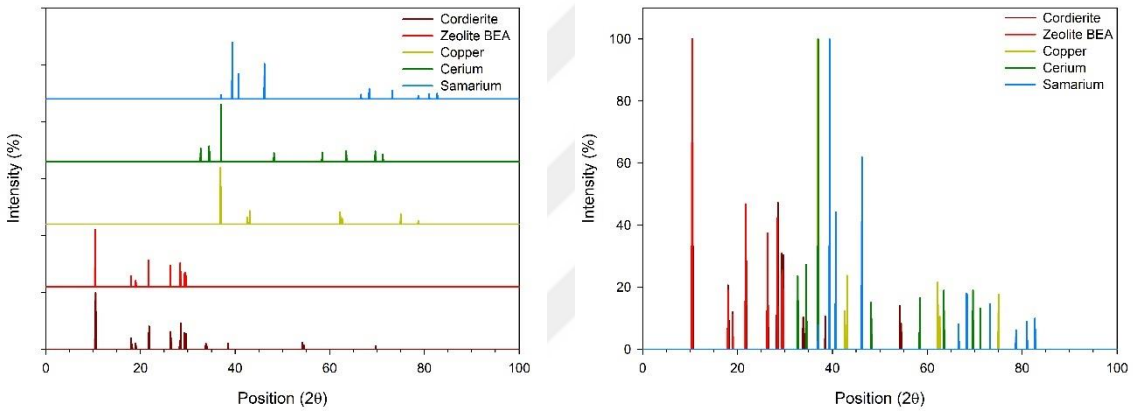

a) b)

Figure 4.26. XRD analysis results of Sm4-BEA; a) separated peaks, b) combined peaks

4.4. FT-IR analysis

FT-IR analysis was performed to identify the chemical composition of the catalyst samples.

Figure 4.27 illustrates the spectra of Y zeolite-based catalysts samples. The spectra exhibit several characteristic peaks: 3360-3369 cm^{-1}: This region typically shows a broad absorption band associated with OH groups, indicating the presence of water or hydroxyl groups. This could be attributed to water molecules within the porous structure of the Y zeolite. 1632-1633 cm^{-1}: This peak corresponds to the deformation vibrations of water molecules and is consistent across all samples. It suggests the presence of adsorbed water on the surface of the zeolite. 1030-1040 cm^{-1}: This region displays the characteristic Si-O or Al-O vibrations of Y zeolite. Despite modification with Sm and Cu, the primary Si-O-Al skeleton of the zeolite remains intact. 580-766 cm^{-1}: Different vibrations are observed in this range, which may be associated with Cu and Sm elements. Peaks in this low wavenumber region are often related to metal-oxygen bonds, suggesting the integration of Sm or Cu into the zeolite structure. Around 450 cm^{-1}: This peak is associated with the Si-O or Al-O bonds, which are fundamental components of the zeolite structure. With increasing Sm concentration slight

shifts and intensity changes are observed in the lower wavenumber peaks. This suggests that the higher concentration of Sm induces some structural changes in the zeolite framework. Particularly in the 579-580 cm^{-1} range: These peaks appear to be influenced by the presence of Sm and Cu, indicating that both elements may interact with the zeolite structure in their oxide forms.

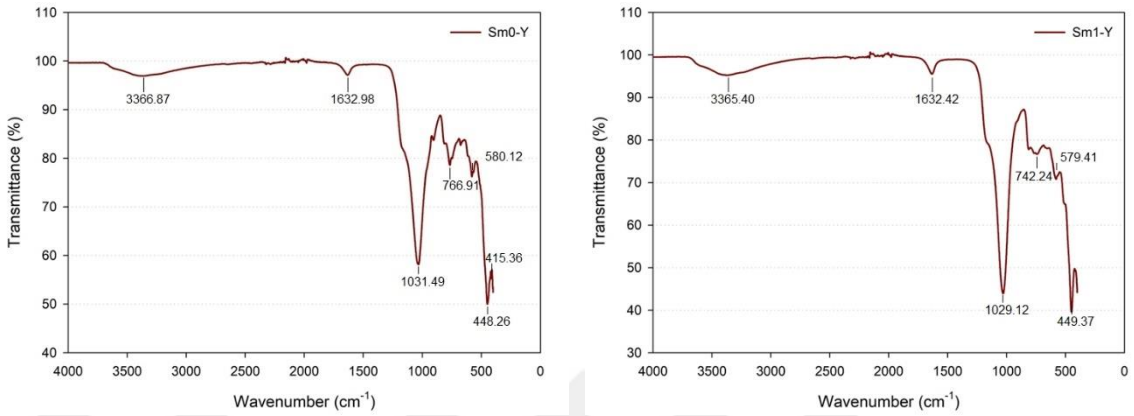

a) Sm0-Y

b) Sm1-Y

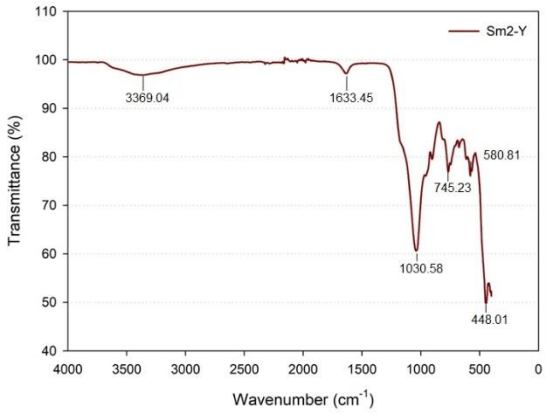

c) Sm2-Y

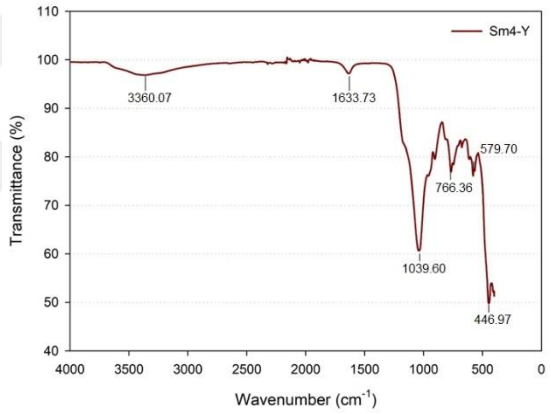

d) Sm4-Y

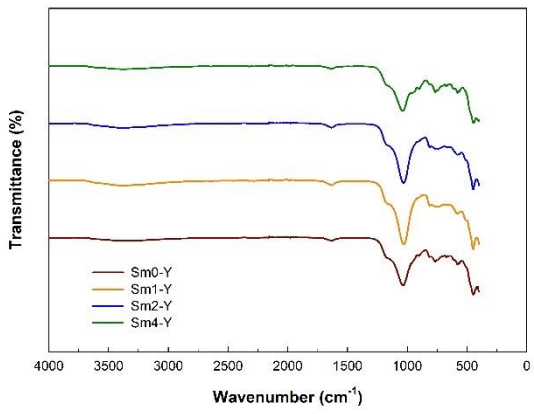

e) FT-IR spectra of zeolite Y set

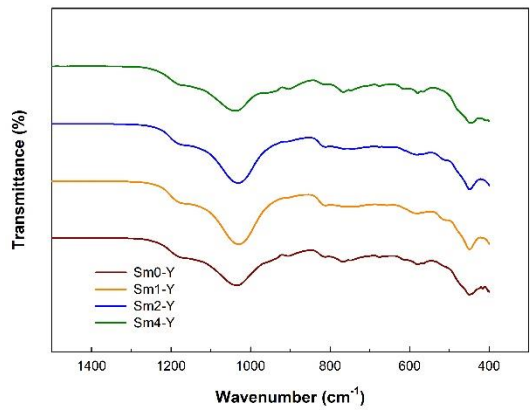

f) FT-IR spectra of zeolite Y set (1500-400 cm^{-1})

Figure 4.27. FT-IR spectra of Y zeolite-based catalyst samples

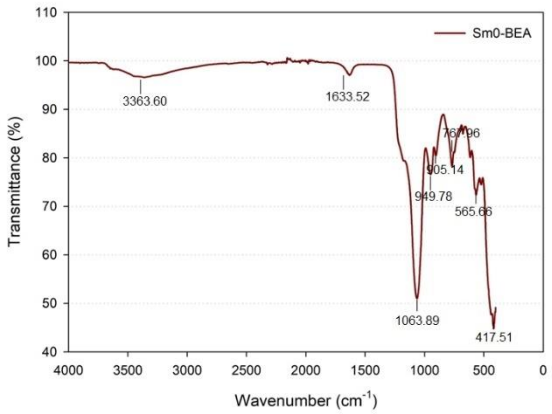

a) Sm0-BEA

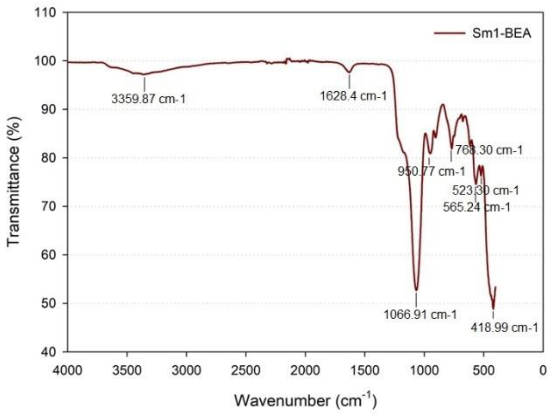

b) Sm1-BEA

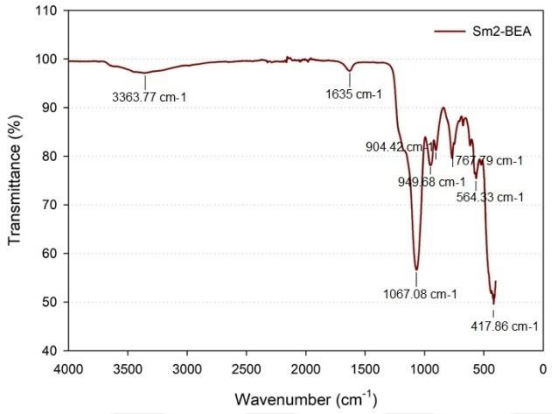

c) Sm2-BEA

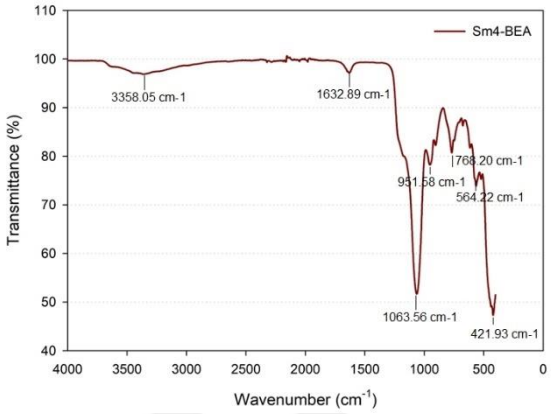

d) Sm4-BEA

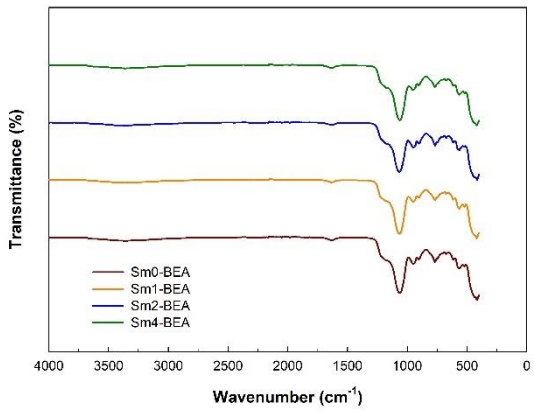

e) FT-IR spectra of zeolite BEA set

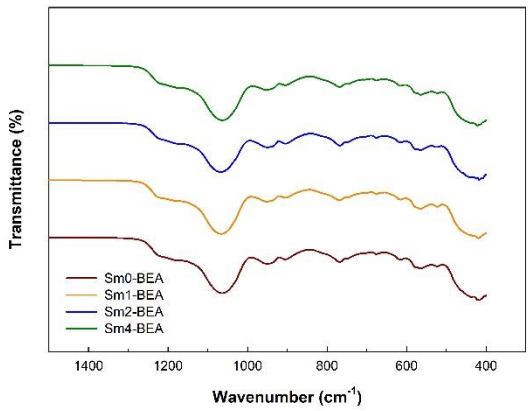

f) FT-IR spectra of zeolite BEA set (1500-400 cm^{-1})

Figure 4.28. FT-IR spectra of BEA zeolite-based catalyst samples

Figure 4.28 represents the spectra of BEA zeolite-based catalysts samples. 3358-3363 cm^{-1}: This region shows a broad band, likely associated with OH stretching vibrations, which can be attributed to adsorbed water molecules in the zeolite structure. The presence of these peaks indicates water or hydroxyl groups within the BEA zeolite's porous structure. 1632-1635 cm^{-1}: This peak corresponds to the bending vibration of water molecules, confirming the presence of adsorbed water

on the BEA zeolite surface, similar to what was observed in Y zeolite samples. 1063-1067 cm^{-1}: This range shows the characteristic Si-O or Al-O vibrations in the BEA zeolite framework. The presence of Sm and Cu does not appear to significantly alter the main structure of the BEA zeolite, as the Si-O-Al framework remains stable. 564-768 cm^{-1}: Peaks in this region could be linked to interactions involving Cu and Sm within the BEA structure. These lower wavenumber peaks are often associated with metal-oxygen bonds, indicating that Cu and Sm may be integrated into the zeolite matrix, affecting its structure and possibly its catalytic properties. 417-421 cm^{-1}: This low-wavenumber peak could be attributed to the fundamental framework vibrations of the BEA zeolite structure, specifically associated with Si-O or Al-O bonds, but might also indicate the influence of Sm and Cu on the zeolite's lattice structure. The BEA zeolite samples exhibit similar water-related peaks (around 3350-3360 cm^{-1} and 1630 cm^{-1}), indicating that the presence of adsorbed water is common across both BEA and Y zeolite structures. In BEA zeolite, the Si-O or Al-O framework vibrations (1060-1070 cm^{-1}) are slightly higher compared to Y zeolite, suggesting minor structural differences between BEA and Y frameworks. BEA samples generally display lower-intensity peaks in the 564-768 cm^{-1} range, potentially indicating a different mode of interaction or integration of Sm and Cu in the BEA structure compared to Y zeolite.

4.5. BET analysis

The BET surface areas of the cordierite and the synthesized catalysts were measured using nitrogen gas. The BET surface area of the unmodified cordierite material was approximately 0.5 m^2/g, as reported by Shigapov et al. (1999). The data related to the surface and pore area of the samples are presented in Table 4.10. The table reveals that, following acid treatment, the surface area of the sample increased by approximately 50 times. In addition, within the set using Y zeolite, the surface areas of the Sm0-Y, Sm1-Y, Sm2-Y, and Sm4-Y catalysts increased by 210, 290, 250, and 125 times, respectively. In the set using Beta zeolite, the increase ratios of surface areas for the Sm0-BEA, Sm1-BEA, Sm2-BEA, and Sm4-BEA catalysts were observed to be 150, 140, 150, and 130, respectively. Examining the samples within the Set Y reveals that the addition of Sm initially increases the surface area; however, with further loading, the surface area begins to decrease. In Set BEA, the trend differs slightly: with the addition of 1% Sm, the surface area decreases; however, at 2% Sm loading, a slight increase in surface area is observed. For both sets, the catalysts with 4% Sm addition exhibit a lower surface area compared to the catalyst samples without Sm addition. For all catalyst samples, the micropore area follows a similar trend of increase and decrease as observed in the overall surface area.

Table 4.10. Surface and pore area values for catalyst sample

Catalyst Sample	BET surface area (m^2/g)	Langmuir surface area (m^2/g)	Micropore area (m^2/g)
Acid-treated	24.9842	31.1386	18.5634
Sm0-Y	104.5103	123.8599	88.1507
Sm1-Y	143.7719	169.0003	122.4393
Sm2-Y	123.9457	144.3760	106.8772
Sm4-Y	62.4686	75.1811	48.4662
Sm0-BEA	74.1148	92.7152	47.9113
Sm1-BEA	71.1378	86.2749	62.4882
Sm2-BEA	74.8524	96.4016	33.5314
Sm4-BEA	66.8737	86.9873	28.8989

4.6. DeNO$_x$ Performance Test Results

The produced catalysts were subjected to SCR performance testing to determine NO_x conversion efficiency. The tests were conducted at space velocities of 30000 and 40000 h^{-1}, within a temperature range of 150°C to 240°C, under no-load and two different load conditions (2 kW and 4 kW), using ethanol as the reductant.

4.6.1. NO$_x$ conversion efficiency of the Y zeolite-based catalysts

The conversion rates obtained for the four catalysts produced using Y zeolite under no-load and two different load (2 and 4 kW) conditions are presented in the following graphs.

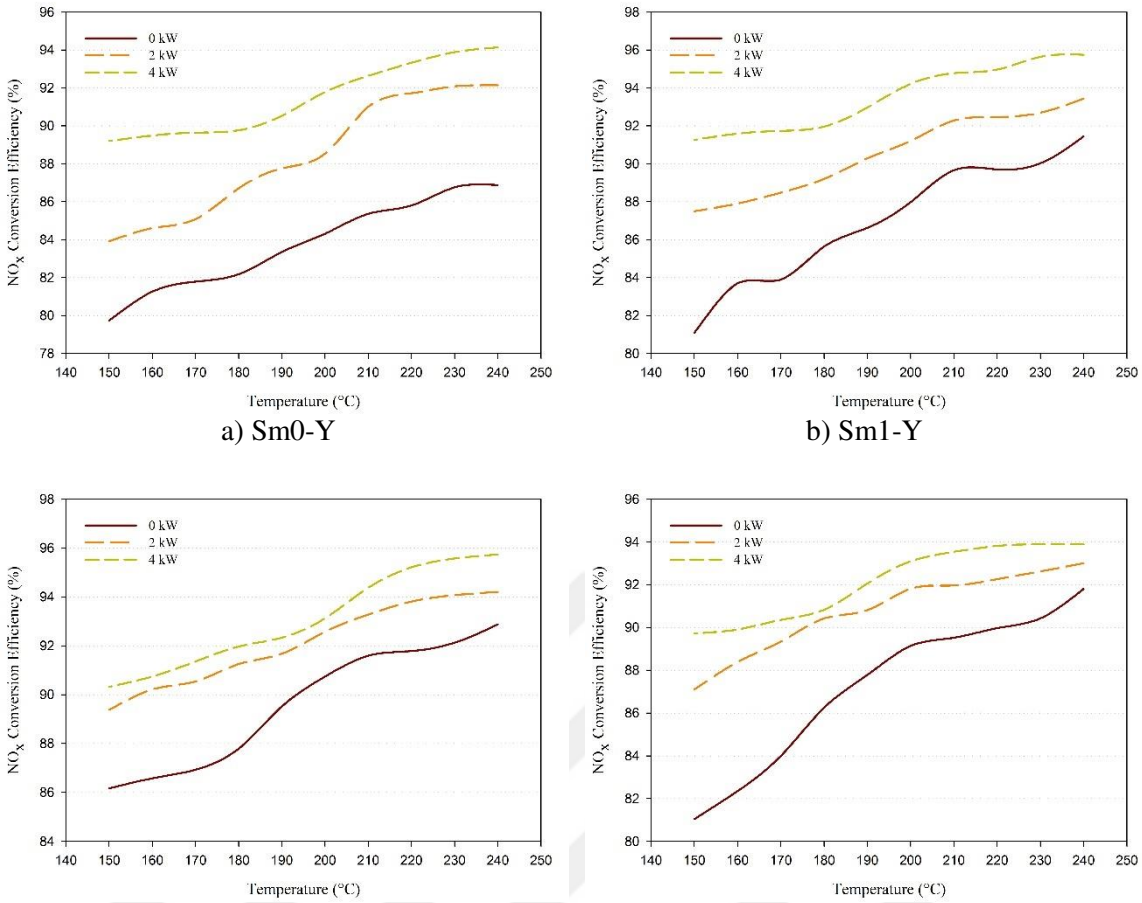

a) Sm0-Y b) Sm1-Y

c) Sm2-Y d) Sm4-Y

Figure 4.29. DeNO$_x$ performance of Y zeolite-based catalysts at 30000 h^{-1}

Figure 4.29 presents the temperature-dependent variation of NO_x conversion rates for the Sm0-Y, Sm1-Y, Sm2-Y, and Sm4-Y catalysts at space velocity of 30000 h^{-1}. The graph examination shows that, for all four catalysts, the conversion rates increase with a temperature rise. Additionally, the increase in engine load positively impacts the conversion rate.

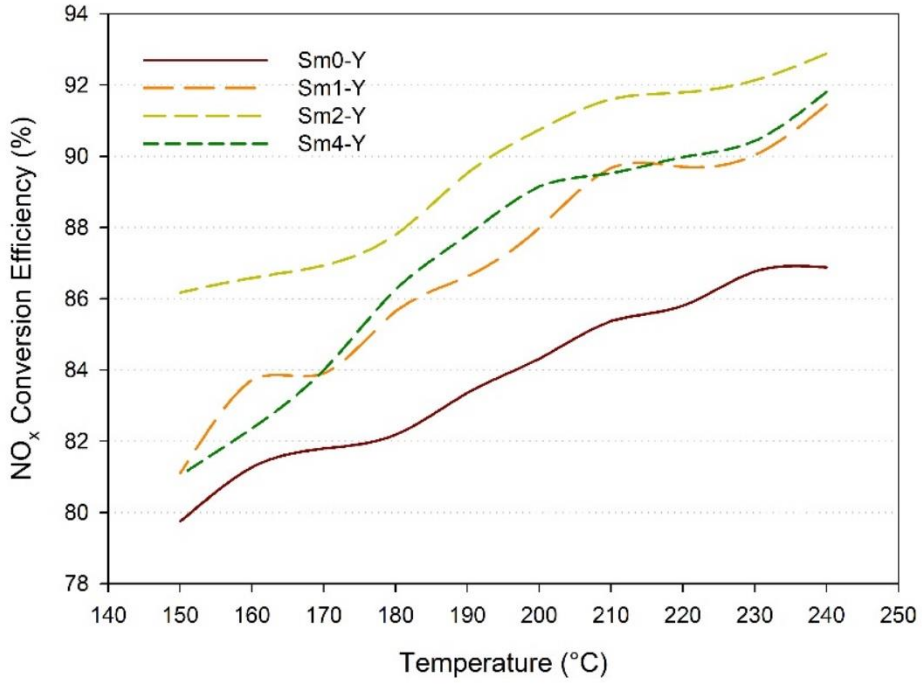

Figure 4.30. NO_x conversion efficiency of the Y zeolite-based catalysts under no-load at 30000 h^{-1}

Figure 4.30 shows the NO_x conversion rates for the Y zeolite-based catalyst set at space velocity of 30000 h^{-1} under no-load conditions. Examination of the graph indicates that the addition of Sm leads to an increase in conversion rates; however, when the Sm addition exceeds 2%, this conversion rate decreases. The catalysts with the highest to lowest conversion rates are ranked as Sm2-Y > Sm4-Y > Sm1-Y > Sm0-Y, with their respective maximum conversion rates at 240°C being 92.88%, 91.81%, 91.45%, and 86.88%. The conversion rates obtained at different temperatures throughout the test are provided in detail in Table 4.11.

Table 4.11. NO_x conversion efficiency of the Y zeolite-based catalysts under no-load at 30000 h^{-1}

Temperature (°C)	**Sm0-Y**	**Sm1-Y**	**Sm2-Y**	**Sm4-Y**
240	86.8784	91.4489	92.8805	91.8100
230	86.7677	90.0338	92.1310	90.4294
220	85.8043	89.7033	91.7908	89.9754
210	85.3704	89.6656	91.6008	89.5214
200	84.3171	87.9841	90.7452	89.1476
190	83.3597	86.6258	89.5242	87.7887
180	82.1831	85.6455	87.7956	86.2590
170	81.7942	83.9013	86.9324	83.9969
160	81.2695	83.7093	86.5780	82.3550
150	79.7489	81.1017	86.1687	81.0400
Average (%)	**83.7493**	**86.9819**	**89.6147**	**87.2324**

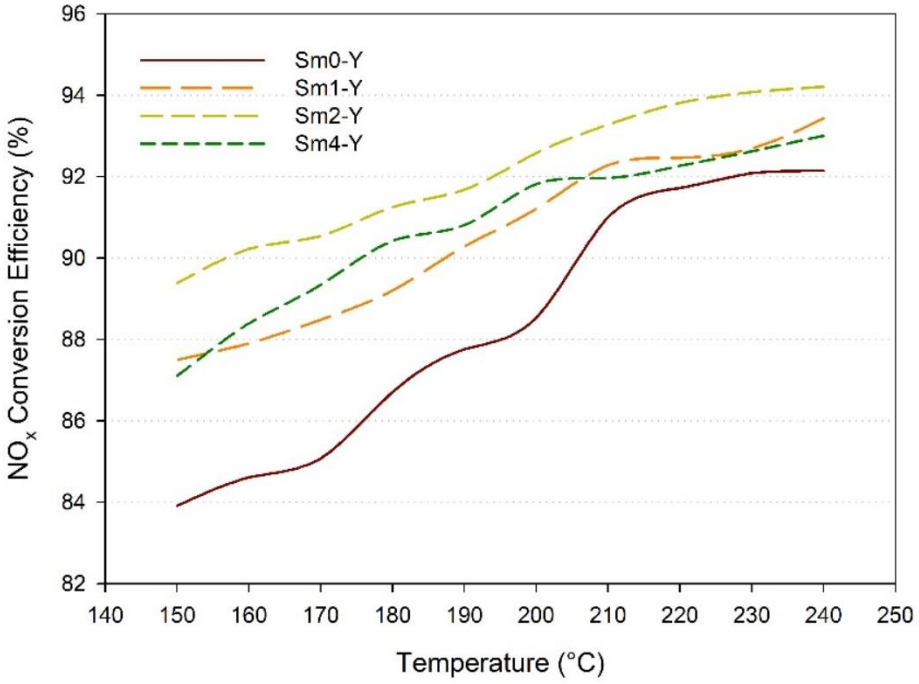

Figure 4.31. NO_x conversion efficiency of the Y zeolite-based catalysts under 2 kW load at 30000 h^{-1}

Figure 4.31 illustrates the NO_x conversion rates for the Y zeolite-based catalyst set at a space velocity of 30000 h^{-1} under 2 kW load conditions. The graph reveals that adding Sm enhances the conversion rates, though this effect diminishes when the Sm content exceeds 2%. Among the catalysts, Sm2-Y demonstrates the highest conversion rate, followed by Sm1-Y, Sm4-Y, and Sm0-Y, with their respective maximum conversion rates at 240°C recorded as 94.20%, 93.43%, 93.00%, and 92.14%. Detailed conversion rates across various temperatures observed during the test are presented in Table 4.12.

Table 4.12. NO_x conversion efficiency of the Y zeolite-based catalysts under 2 kW load at 30000 h^{-1}

Temperature (°C)	Sm0-Y	Sm1-Y	Sm2-Y	Sm4-Y
240	92.1420	93.4363	94.2046	93.0036
230	92.0863	92.6928	94.0726	92.6187
220	91.7207	92.4613	93.8100	92.2619
210	91.0078	92.2800	93.2764	91.9609
200	88.5328	91.2052	92.5773	91.8163
190	87.7574	90.2873	91.6748	90.8076
180	86.7032	89.1987	91.2526	90.4244
170	85.0768	88.4793	90.5407	89.3373
160	84.6089	87.8993	90.2194	88.3914
150	83.9153	87.4954	89.3819	87.1048
Average (%)	**88.3551**	**90.5436**	**92.1010**	**90.7727**

Figure 4.32 displays the NO_x conversion rates for the Y zeolite-based catalyst set at space velocity of 30000 h^{-1} under 4 kW load conditions. The data indicate that the addition of Sm improves the conversion rates except 240 °C, but this enhancement decreases when the Sm content surpasses 2%. Of the catalysts tested, Sm1-Y achieved the highest conversion rate, followed by Sm2-Y, Sm0-Y, and Sm4-Y, with maximum conversion rates at 240°C measured at 95.74%, 95.73%, 94.14%, and 93.88%, respectively. A comprehensive breakdown of conversion rates at different temperatures recorded during the test is shown in Table 4.13.

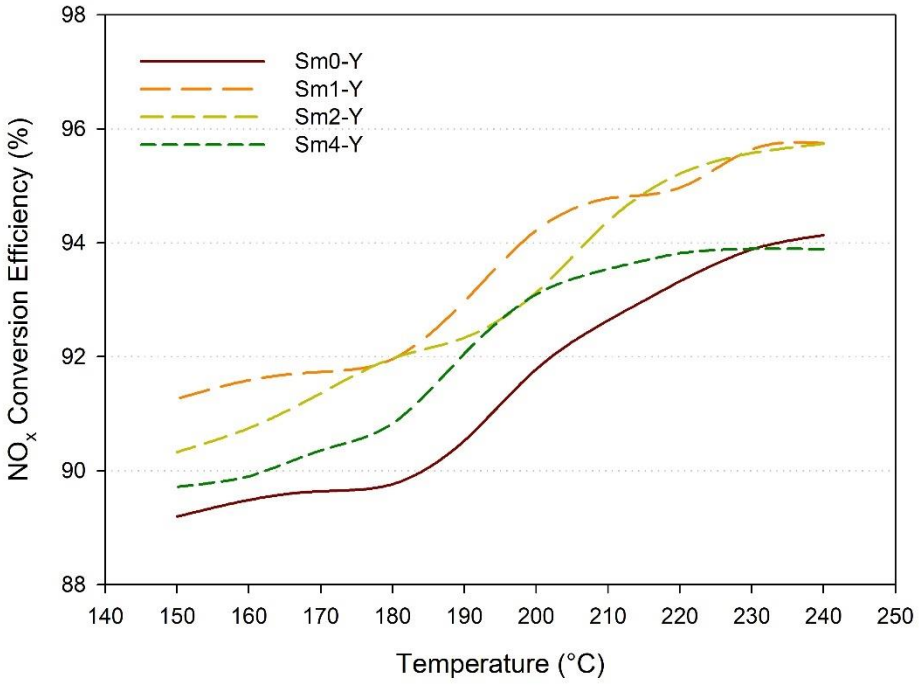

Figure 4.32. NO_x conversion efficiency of the Y zeolite-based catalysts under 4 kW load at 30000 h^{-1}

Table 4.13. NO_x conversion efficiency of the Y zeolite-based catalysts under 4 kW load at 30000 h^{-1}

Temperature (°C)	Sm0-Y	Sm1-Y	Sm2-Y	Sm4-Y
240	94.1341	95.7481	95.7348	93.8897
230	93.8821	95.6377	95.5733	93.8942
220	93.3252	94.9642	95.2107	93.8150
210	92.6357	94.7767	94.3773	93.5375
200	91.7831	94.2141	93.1253	93.0931
190	90.5268	92.9714	92.3306	92.0548
180	89.7618	91.9563	91.9672	90.8247
170	89.6373	91.7288	91.3553	90.3517
160	89.4858	91.5843	90.7433	89.8976
150	89.1950	91.2603	90.3233	89.7144
Average (%)	**91.4367**	**93.4842**	**93.0741**	**92.1073**

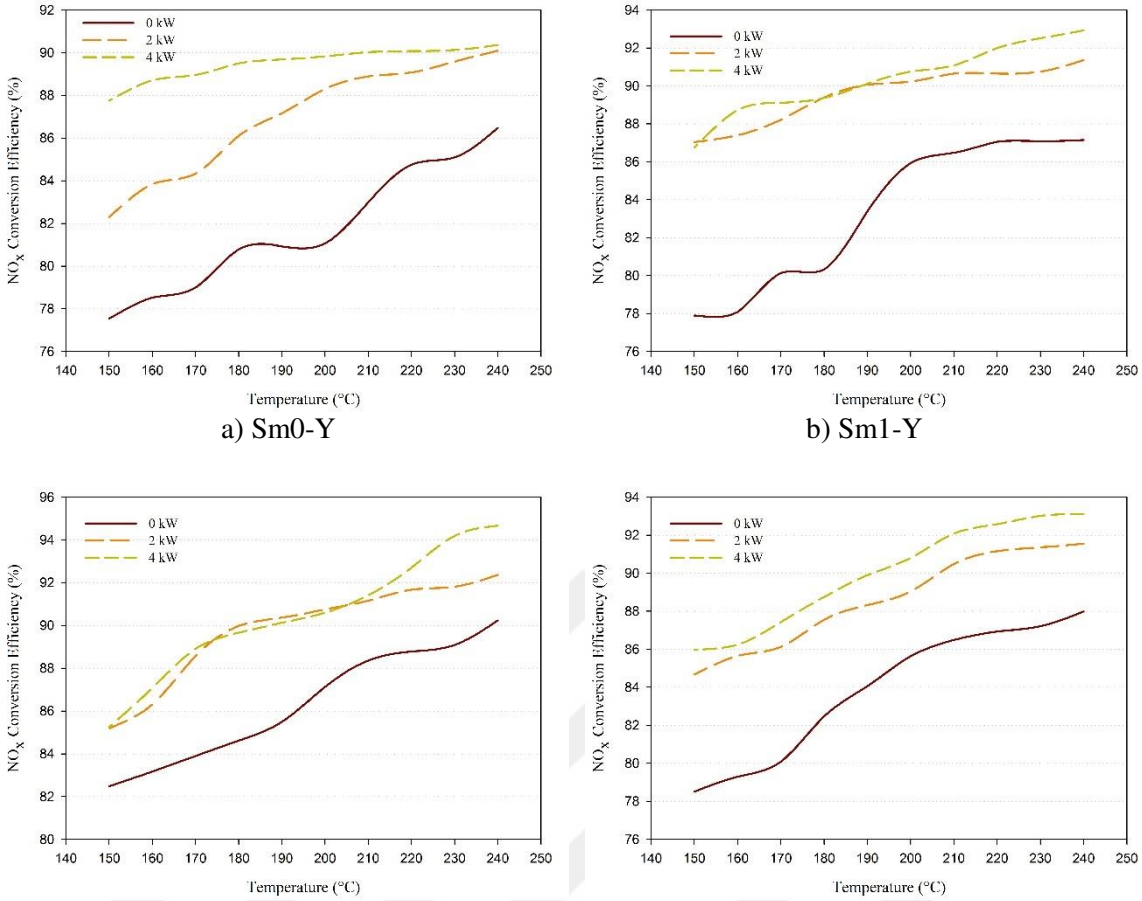

a) Sm0-Y b) Sm1-Y

c) Sm2-Y d) Sm4-Y

Figure 4.33. DeNO$_x$ efficiency of Y zeolite-based catalysts at 40000 h^{-1}

Figure 4.33 shows the NO$_x$ conversion rates for the Sm0-Y, Sm1-Y, Sm2-Y, and Sm4-Y catalysts at 40000 h^{-1}. In addition to increasing the temperature, the rise in load also led to higher NO$_x$ conversion rates, as observed at a space velocity of 30000 h^{-1}.

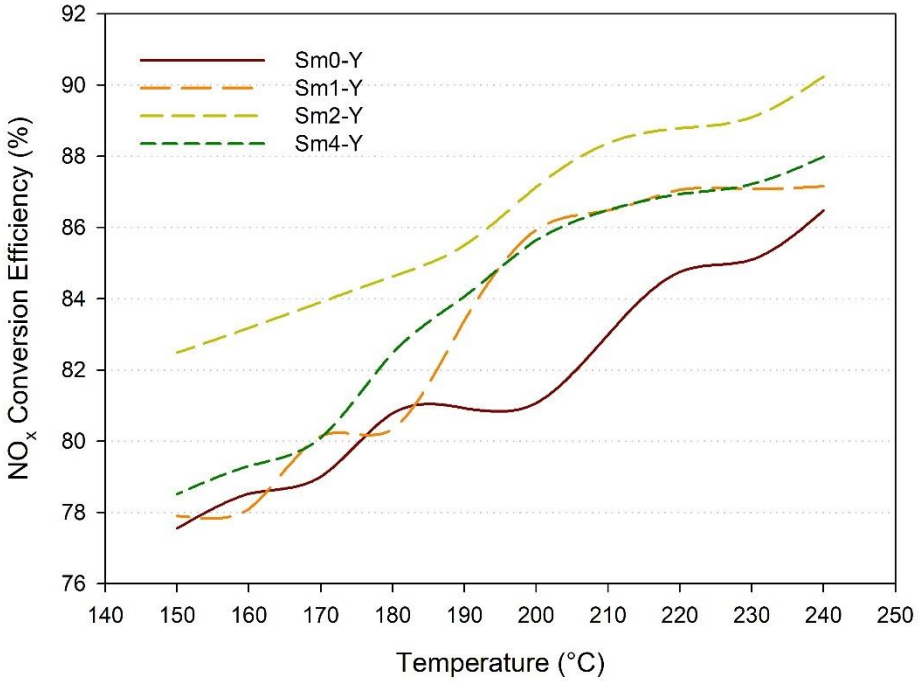

Figure 4.34. NO_x conversion efficiency of the Y zeolite-based catalysts under no-load at 40000 h^{-1}

Figure 4.34 shows the NO_x conversion efficiency of four catalysts (Sm0-Y, Sm1-Y, Sm2-Y, and Sm4-Y) across a temperature range from 150°C to 240°C, with all catalysts displaying improved efficiency as temperature increases. Sm2-Y achieves the highest efficiency, surpassing 90% at 240°C, followed closely by Sm4-Y, which reaches nearly 88% at higher temperatures. Sm1-Y performs better than Sm4-Y at lower temperatures but is eventually surpassed as temperatures rise, peaking slightly above 85%. Sm0-Y, with no Sm addition, has the lowest efficiency, starting around 78% and reaching just above 86% at the highest temperature. The addition of Sm enhances NO_x conversion efficiency, with 2% Sm (Sm2-Y) providing optimal improvement, while higher Sm content (Sm4-Y) shows diminishing returns, indicating that both increased temperature and an optimal Sm concentration contribute to superior catalytic performance, with Sm2-Y being the most effective. Detailed data related to the graph are provided in Table 4.14.

Table 4.14. NO_x conversion efficiency of the Y zeolite-based catalysts under no-load at 40000 h^{-1}

Temperature (°C)	Sm0-Y	Sm1-Y	Sm2-Y	Sm4-Y
240	86.4800	87.1508	90.2400	87.9900
230	85.0972	87.0856	89.0950	87.2161
220	84.7554	87.0581	88.7865	86.9368
210	82.9919	86.4788	88.3629	86.4887
200	81.0727	85.9323	87.1329	85.6433
190	80.9289	83.3896	85.4980	84.0601
180	80.7850	80.3286	84.6200	82.4769
170	79.0000	80.1389	83.8975	80.0870
160	78.5275	78.0900	83.1750	79.2985
150	77.5500	77.8983	82.4821	78.5100
Average (%)	**81.7189**	**83.3551**	**86.3290**	**83.8708**

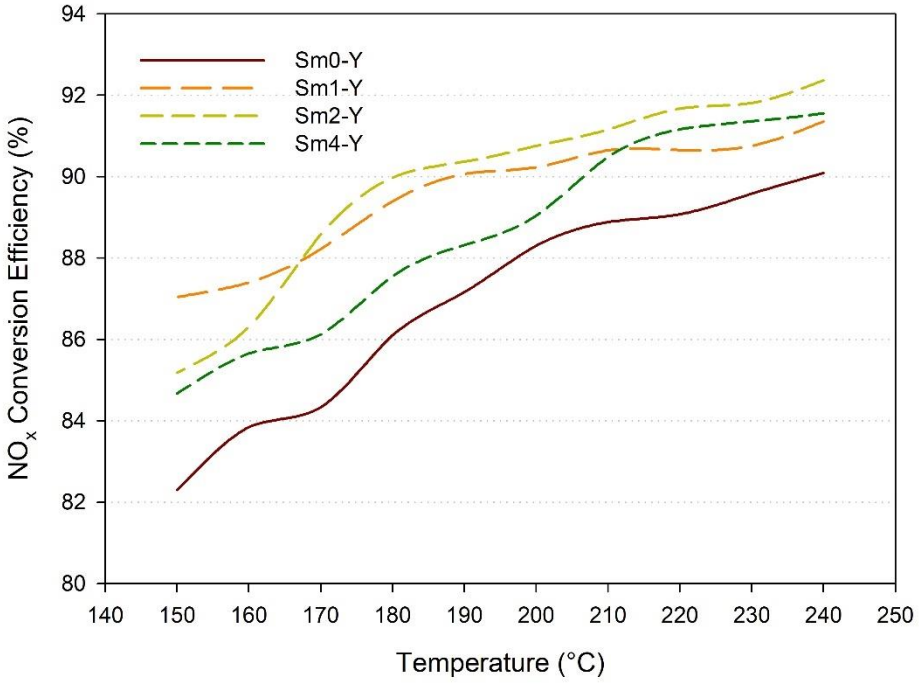

Figure 4.35. NO_x conversion efficiency of the Y zeolite-based catalysts under 2 kW load at 40000 h^{-1}

Figure 4.35 shows the NO_x conversion efficiency of Sm0-Y, Sm1-Y, Sm2-Y, and Sm4-Y across a temperature range from 150°C to 240°C, indicating that efficiency improves with increasing temperature for all catalysts. Sm2-Y demonstrates the highest conversion efficiency throughout the temperature range, reaching around 92% at 240°C. Sm1-Y and Sm4-Y follow closely, both surpassing 90% efficiency at higher temperatures, with Sm1-Y slightly outperforming Sm4-Y at lower temperatures. Sm0-Y, lacking Sm addition, shows the lowest efficiency, starting at 83% and reaching 90% at the highest temperature. The addition of Sm significantly boosts conversion efficiency, with 2% Sm (in Sm2-Y) providing the optimal enhancement, while additional Sm (as in Sm4-Y) yields diminishing returns in NO_x reduction performance. Table 4.15 provides a detailed breakdown of the conversion rates recorded at various temperatures throughout the test.

Table 4.15. NO_x conversion efficiency of the Y zeolite-based catalysts under 2 kW load at 40000 h^{-1}

Temperature (°C)	Sm0-Y	Sm1-Y	Sm2-Y	Sm4-Y
240	90.0900	91.3568	92.3667	91.5532
230	89.5833	90.7520	91.8080	91.3596
220	89.0767	90.6500	91.6700	91.1591
210	88.8857	90.6426	91.1550	90.4825
200	88.3062	90.2295	90.7550	89.0406
190	87.1611	90.0620	90.3669	88.3171
180	86.1056	89.3918	89.9750	87.5491
170	84.3291	88.2174	88.5792	86.1207
160	83.8476	87.3963	86.3063	85.6520
150	82.3000	87.0348	85.1825	84.6725
Average (%)	**86.9685**	**89.5733**	**89.8165**	**88.5906**

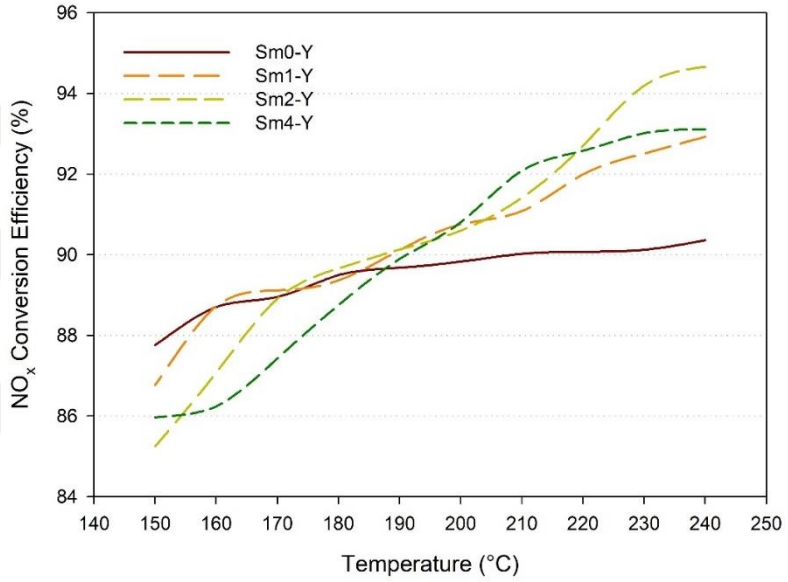

Figure 4.36. NO_x conversion efficiency of the Y zeolite-based catalysts under 4 kW load at 40000 h^{-1}

Figure 4.36 illustrates the NO_x conversion efficiency of Sm0-Y, Sm1-Y, Sm2-Y, and Sm4-Y over a temperature range from 150 °C to 240°C. As temperature increases, all catalysts show a general improvement in NO_x conversion efficiency. Sm2-Y achieves the highest efficiency, surpassing 94% at higher temperatures, closely followed by Sm4-Y, which also reaches above 93% as temperatures rise. Sm1-Y follows a similar trend, reaching around 92%, while Sm0-Y exhibits the lowest efficiency, remaining below 91% across the temperature range. The addition of Sm clearly enhances catalytic performance, with Sm2-Y showing the optimal NO_x conversion efficiency, particularly at elevated temperatures, while further Sm addition in Sm4-Y leads to slightly diminished returns. This suggests that both temperature elevation and an optimal level of Sm addition (as in Sm2-Y) contribute to maximum NO_x conversion efficiency. Table 4.16 provides a detailed breakdown of NO_x conversions at various temperatures under a space velocity of 40000 h^{-1} and a 4-kW load.

Table 4.16. NO_x conversion efficiency of the Y zeolite-based catalysts under 4 kW load at 40000 h^{-1}

Temperature (°C)	Sm0-Y	Sm1-Y	Sm2-Y	Sm4-Y
240	90.3597	92.9240	94.6600	93.1132
230	90.1246	92.5054	94.1874	93.0119
220	90.0734	91.9917	92.6983	92.5763
210	90.0222	91.0813	91.4105	92.0865
200	89.8317	90.7500	90.5940	90.8039
190	89.6800	90.1133	90.1270	89.8944
180	89.4981	89.3650	89.6600	88.7456
170	88.9543	89.1156	88.9100	87.4247
160	88.7094	88.7280	87.0800	86.2364
150	87.7606	86.7689	85.2500	85.9631
Average (%)	**89.5014**	**90.3343**	**90.4577**	**89.9856**

Above graphs indicate that NO_x conversion efficiency improves with increasing temperature for all Y zeolite-based catalysts. Sm2-Y consistently shows the highest efficiency, suggesting that a 2% Sm addition optimally enhances performance. Sm4-Y and Sm1-Y also perform well, while Sm0-Y, without Sm, has the lowest efficiency. Higher loads and temperatures further boost conversion rates, demonstrating that temperature, Sm content, and operating conditions significantly impact NO_x reduction, with Sm2-Y being the most effective catalyst across all tested scenarios.

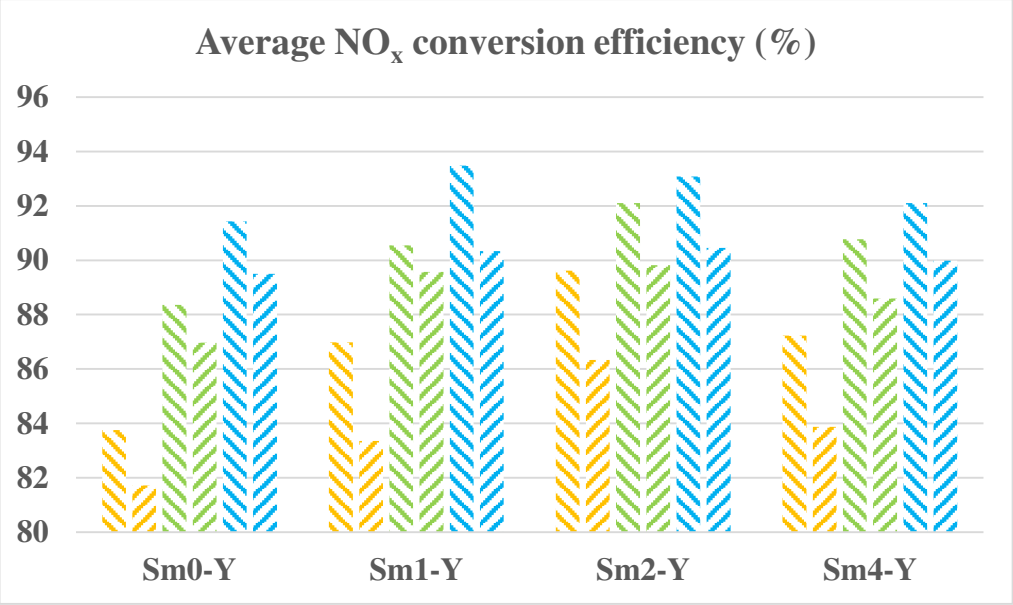

Figure 4.37. Average NO_x conversion efficiency for Y zeolite-based catalysts

Figure 4.37 illustrates the average NO_x conversion efficiencies for Y zeolite-based catalysts between 150 to 240 °C for loads of 0, 2, and 4 kW, represented by the orange, green, and blue lines, respectively. Additionally, the left-leaning lines denote average conversion rates achieved at a space velocity of 30000 h^{-1}, while the right-leaning lines indicate those obtained at a space velocity of 40000 h^{-1}. For each sample, the NO_x conversion efficiency increases with higher load. At a space

velocity of 30000 h^{-1}, conversion efficiencies tend to be slightly higher compared to 40000 $^{h-1}$ for the same load and sample. These trends indicate that both increased load and lower space velocity contribute to improved NO_x conversion efficiency across the samples in the specified temperature range.

4.6.2. NO_x conversion efficiency of the Beta zeolite-based catalysts

Similar to the Y zeolite-based catalyst, the conversion rates achieved for the four catalysts produced using BEA zeolite under no-load and two different load conditions (2 kW and 4 kW) are shown in the following graphs.

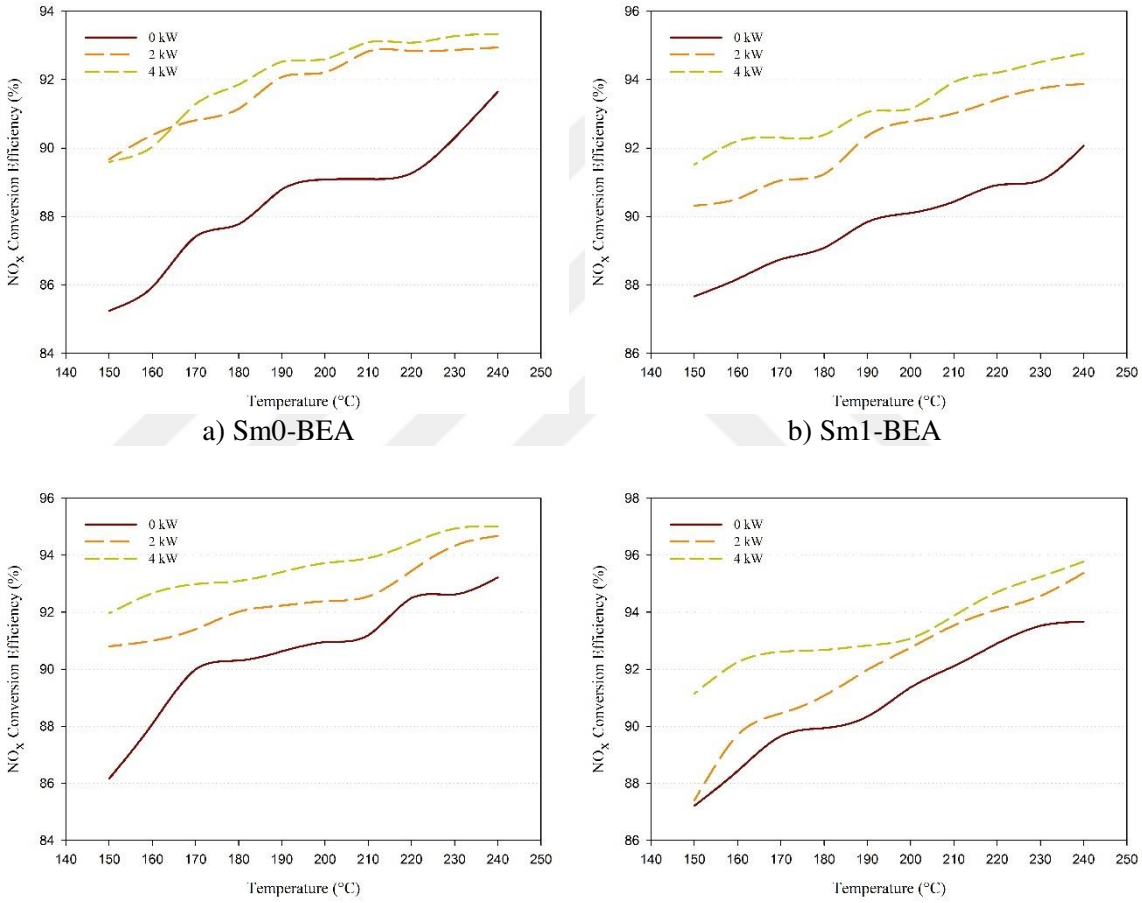

a) Sm0-BEA b) Sm1-BEA

c) Sm2-BEA d) Sm4-BEA

Figure 4.38. $DeNO_x$ performance of BEA zeolite-based catalysts at 30000 h^{-1}

Figure 4.38 illustrates the NO_x conversion rates as a function of temperature for the Sm0-BEA, Sm1-BEA, Sm2-BEA, and Sm4-BEA catalysts at a space velocity of 30000 h^{-1}. Analysis of the graph reveals that NO_x conversion rates for each catalyst improve progressively with increasing temperature. Furthermore, an increase in engine load enhances the conversion rates, indicating that higher loads contribute positively to the catalytic efficiency.

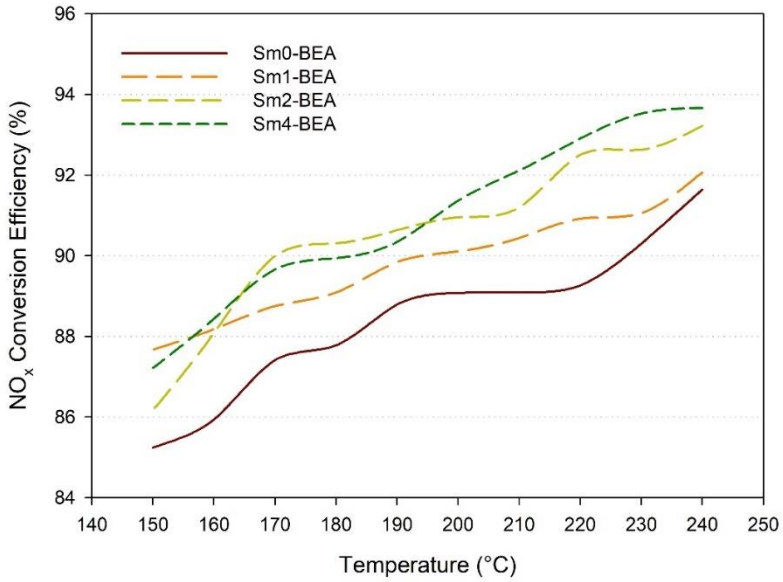

Figure 4.39. NO_x conversion efficiency of the BEA zeolite-based catalysts under no-load at 30000 h^{-1}

Figure 4.39 shows the NO_x conversion efficiency of BEA-based catalysts (Sm0-BEA, Sm1-BEA, Sm2-BEA, and Sm4-BEA) as a function of temperature under no-load (0 kW) conditions at a space velocity of 30000 h^{-1}. As temperature increases from 150°C to 240°C, NO_x conversion efficiency improves across all catalysts. Among the catalysts, Sm4-BEA consistently exhibits the highest NO_x conversion efficiency across the temperature range, reaching nearly 95% at higher temperatures. In contrast, Sm0-BEA shows the lowest efficiency, indicating that the presence and quantity of Sm in the catalyst formulation positively impact NO_x reduction performance. Sm1-BEA and Sm2-BEA follow intermediate trends, showing improved efficiency relative to Sm0-BEA but not reaching the levels observed for Sm4-BEA. Table 4.17 provides a comprehensive summary of NO_x conversions at various temperatures for the BEA catalyst under a space velocity of 30000 h^{-1} and no-load condition.

Table 4.17. NO_x conversion efficiency of the BEA zeolite-based catalysts under no-load at 30000 h^{-1}

Temperature (°C)	Sm0-BEA	Sm1-BEA	Sm2-BEA	Sm4-BEA
240	91.6467	92.0700	93.2210	93.6675
230	90.3011	91.0550	92.6225	93.5234
220	89.2625	90.9160	92.4989	92.9071
210	89.0943	90.4360	91.1931	92.1133
200	89.0767	90.1043	90.9540	91.3654
190	88.7953	89.8433	90.6322	90.3429
180	87.7774	89.0860	90.3075	89.9408
170	87.4144	88.7500	89.9971	89.6586
160	85.9378	88.1750	88.0835	88.4364
150	85.2429	87.6667	86.1700	87.2143
Average (%)	**88.4549**	**89.8102**	**90.5680**	**90.9170**

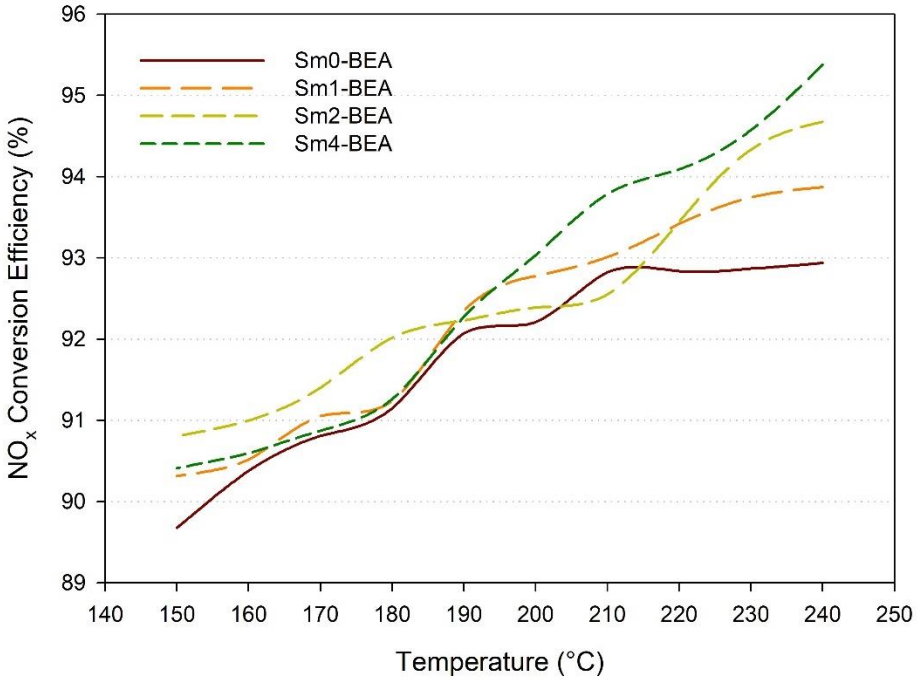

Figure 4.40. NO_x conversion efficiency of the BEA zeolite-based catalysts under 2 kW load at 30000 h^{-1}

Figure 4.40 shows NOx conversion efficiency as a function of temperature for Sm0-BEA, Sm1-BEA, Sm2-BEA, and Sm4-BEA under 2 kW load conditions and a space velocity of 30000 h^{-1}. As the temperature rises from 150°C to 240°C, the NO_x conversion efficiency improves for all catalysts, with Sm4-BEA achieving the highest efficiency, reaching around 96% at 240°C. Sm2-BEA, Sm1-BEA, and Sm0-BEA follow with conversion efficiencies of approximately 94%, 93%, and 92%, respectively, at the same temperature. These results indicate that increasing Sm content enhances NO_x reduction performance, with Sm4-BEA consistently showing the best catalytic efficiency across the temperature range. The detailed data corresponding to the graph are provided in Table 4.18.

Table 4.18. NO_x conversion efficiency of the BEA zeolite-based catalysts under 2 kW load at 30000 h^{-1}

Temperature (°C)	Sm0-BEA	Sm1-BEA	Sm2-BEA	Sm4-BEA
240	92.9382	93.8692	94.6742	95.3778
230	92.8671	93.7424	94.3300	94.5729
220	92.8367	93.4180	93.4450	94.0880
210	92.8240	93.0100	92.5478	93.7867
200	92.2088	92.7750	92.3870	93.0312
190	92.0721	91.9450	92.2263	92.2757
180	91.1467	91.2340	92.0167	91.2582
170	90.8088	91.0520	91.4000	90.8717
160	90.3776	90.5141	90.9963	90.5933
150	89.6767	90.3131	90.8023	90.4100
Average (%)	**91.7757**	**92.1873**	**92.4825**	**92.6265**

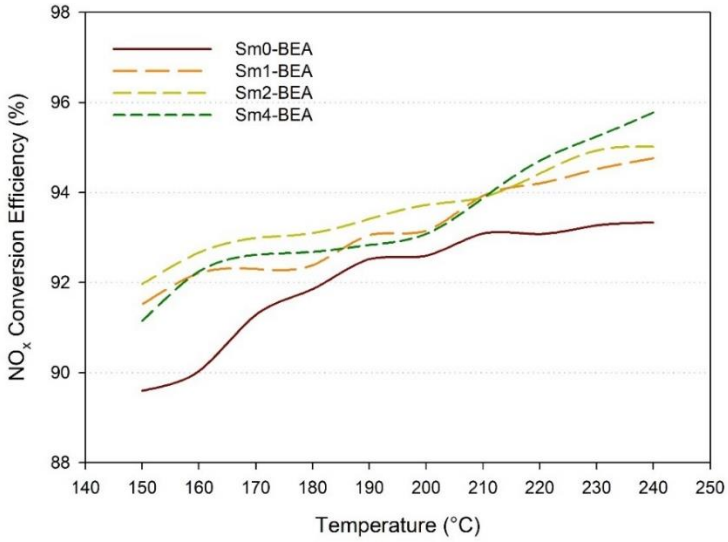

Figure 4.41. NO_x conversion efficiency of the BEA zeolite-based catalysts under 4 kW load at 30000 h^{-1}

Figure 4.41 illustrates NO_x conversion efficiency for BEA-based catalysts (Sm0-BEA, Sm1-BEA, Sm2-BEA, and Sm4-BEA) across a temperature range of 150°C to 240°C under a 4-kW load and a space velocity of 30000 h^{-1}. Notably, all catalysts show improved NOx conversion efficiency as the temperature increases, but the extent of improvement varies by catalyst type. Sm4-BEA exhibits the highest efficiency throughout the temperature range, reaching close to 96% at 240°C, which suggests a stronger temperature-dependent catalytic activity for higher Sm concentrations. Sm2-BEA and Sm1-BEA also show notable performance improvements, peaking around 95% and 94%, respectively, at 240°C, while Sm0-BEA remains comparatively lower, stabilizing around 93%. These results indicate that both higher temperatures and increased Sm content in BEA catalysts positively influence NO_x conversion efficiency, with Sm4-BEA demonstrating the best performance under these conditions. Table 4.19 provides a detailed breakdown of NO_x conversions at various temperatures under a space velocity of 30000 h^{-1} and a 4-kW load.

Table 4.19. NO_x conversion efficiency of the BEA zeolite-based catalysts under 4 kW load at 30000 h^{-1}

Temperature (°C)	Sm0-BEA	Sm1-BEA	Sm2-BEA	Sm4-BEA
240	93.3300	94.7571	95.0128	95.7754
230	93.2693	94.5152	94.9291	95.2400
220	93.0767	94.2007	94.4200	94.7046
210	93.0911	93.9261	93.8933	93.8729
200	92.5971	93.1452	93.7200	93.0752
190	92.5230	93.0506	93.4085	92.8300
180	91.8520	92.3810	93.0970	92.6780
170	91.2833	92.3026	92.9850	92.6141
160	90.0329	92.2056	92.6645	92.2468
150	89.5960	91.5168	91.9675	91.1463
Average (%)	**92.0651**	**93.2001**	**93.6098**	**93.4183**

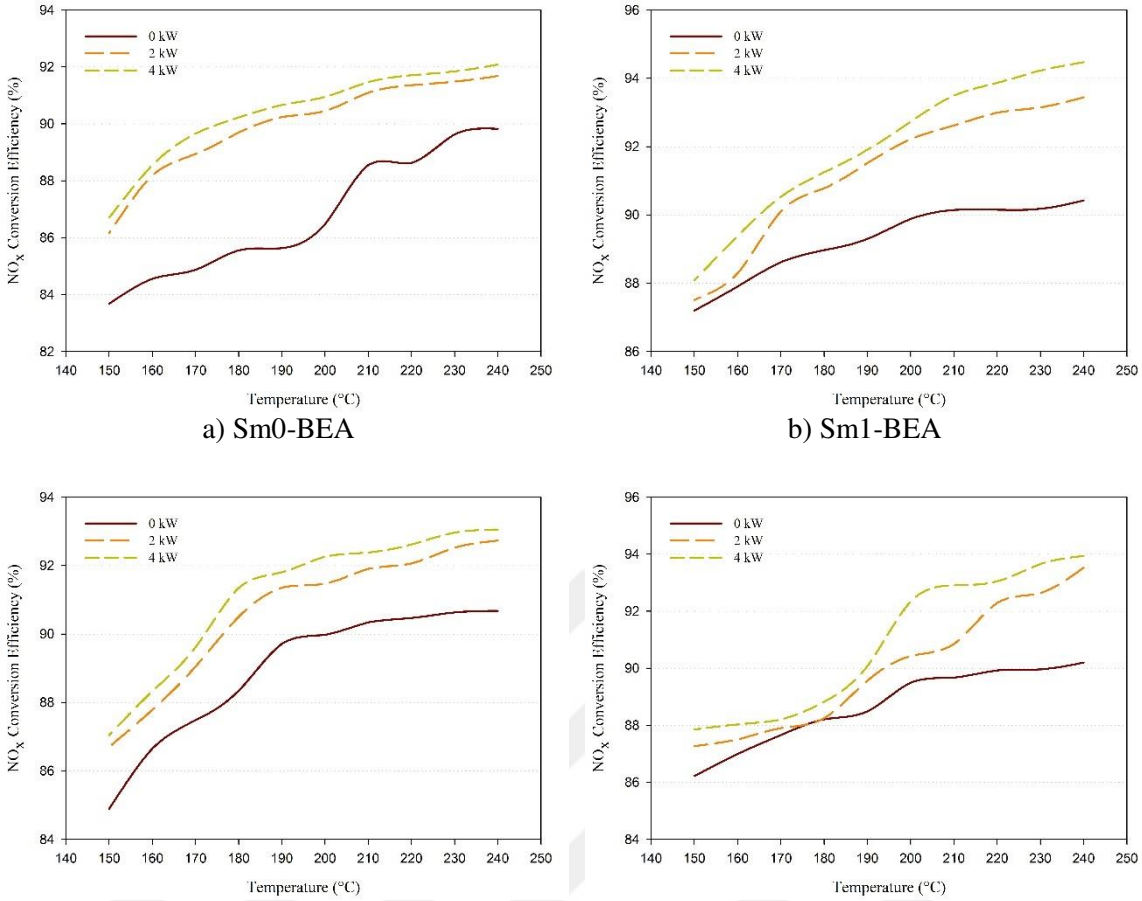

a) Sm0-BEA b) Sm1-BEA

c) Sm2-BEA d) Sm4-BEA

Figure 4.42. DeNO$_x$ efficiency of BEA zeolite-based catalysts at 40000 h^{-1}

Figure 4.42 presents the NO$_x$ conversion rates for Sm0-BEA, Sm1-BEA, Sm2-BEA, and Sm4-BEA catalysts at a space velocity of 40000 h^{-1}. The results indicate that both an increase in temperature and an increase in load contribute to higher NO$_x$ conversion rates. This trend is consistent with observations at a lower space velocity of 30000 h^{-1}, where higher loads similarly enhanced NO$_x$ conversion. These findings suggest that both temperature and load are critical factors in maximizing the efficiency of NO$_x$ conversion for these catalysts.

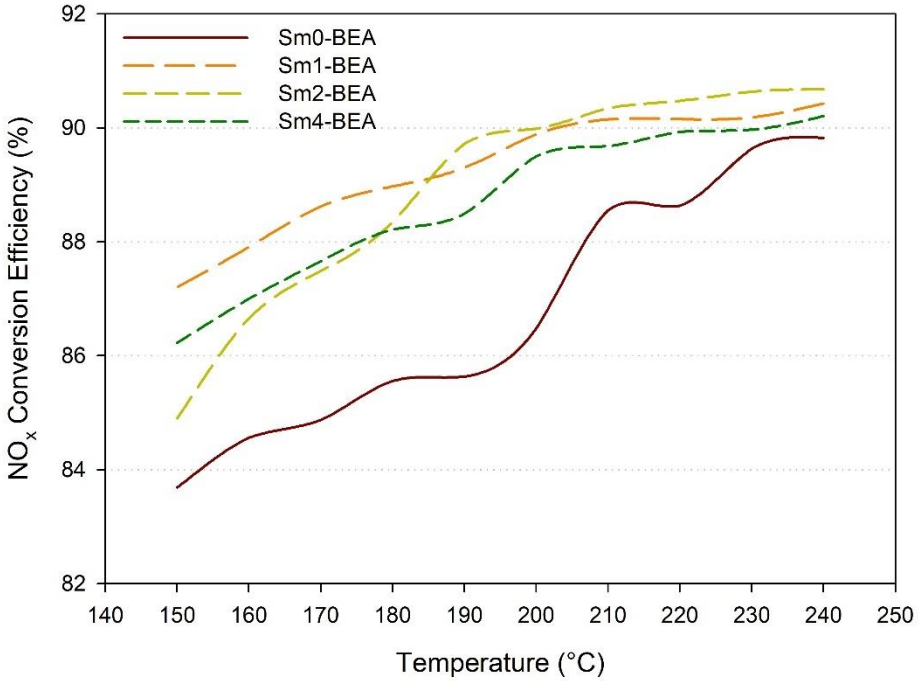

Figure 4.43. NO_x conversion efficiency of the BEA zeolite-based catalysts under no-load at 40000 h^{-1}

Figure 4.43 shows the NO_x conversion efficiencies of BEA-based catalysts (Sm0-BEA, Sm1-BEA, Sm2-BEA, and Sm4-BEA) at various temperatures under a space velocity of 40000 h^{-1} and a no-load (0 kW) condition. The maximum conversion efficiencies for each catalyst are as follows: Sm0-BEA 89.82%, Sm1-BEA at 90.42%, Sm2-BEA at 90.67%, and Sm4-BEA at 90.20% at 240 °C. These results demonstrate that higher Sm content significantly boosts NO_x conversion efficiency, and increasing temperature has a positive effect on catalytic performance. The conversion rates obtained at different temperatures throughout the test are provided in detail in Table 4.20.

Table 4.20. NO_x conversion efficiency of the BEA zeolite-based catalysts under no-load at 40000 h^{-1}

Temperature (°C)	Sm0-BEA	Sm1-BEA	Sm2-BEA	Sm4-BEA
240	89.8238	90.4258	90.6767	90.2038
230	89.6338	90.1806	90.6321	89.9629
220	88.6315	90.1531	90.4706	89.9267
210	88.5508	90.1429	90.3425	89.6746
200	86.4800	89.8827	89.9825	89.4967
190	85.6364	89.3000	89.7144	88.4900
180	85.5554	88.9700	88.3470	88.2125
170	84.8710	88.6157	87.4863	87.6585
160	84.5600	87.9079	86.6538	86.9985
150	83.6867	87.2000	84.9000	86.2250
Average (%)	**86.7429**	**89.2779**	**88.9206**	**88.6849**

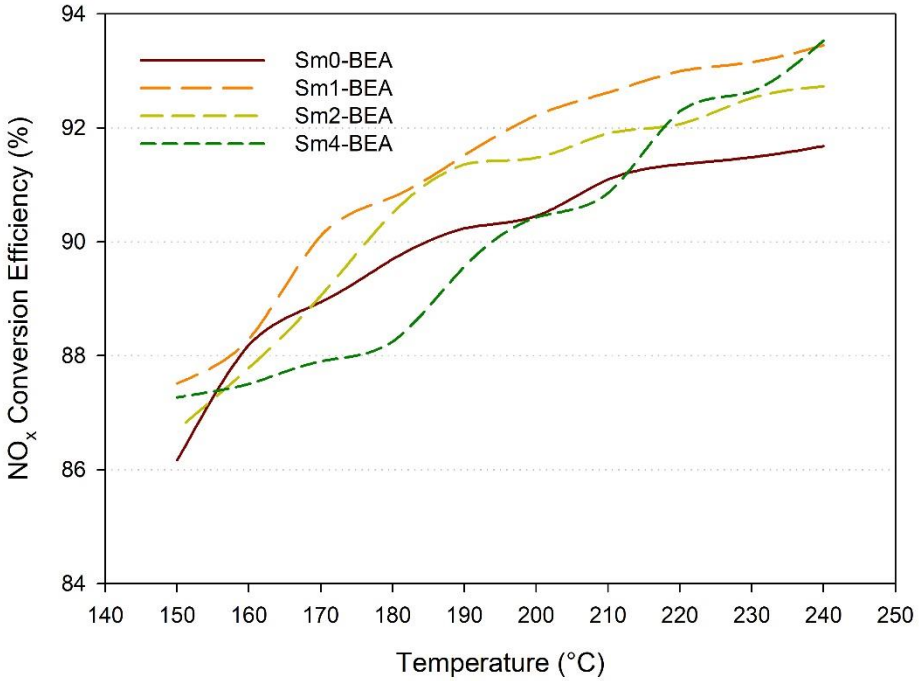

Figure 4.44. NO_x conversion efficiency of the BEA zeolite-based catalysts under 2 kW load at 40000 h^{-1}

Figure 4.44 represents the NO_x conversion efficiency of Sm0-BEA, Sm1-BEA, Sm2-BEA, and Sm4-BEA under a 2-kW load condition and a space velocity of 40,000 h^{-1} across a temperature range from 150°C to 240°C. Under a 2-kW load and a 40000 h^{-1} space velocity, the NO_x conversion efficiencies at 240°C are approximately 91% for Sm0-BEA, 93% for Sm1-BEA, just above 93% for Sm2-BEA, and nearly 94% for Sm4-BEA. The results highlight that both temperature and increased Sm loading enhance the NO_x conversion efficiency, with Sm4-BEA consistently performing the best at higher temperatures. Table 4.21 provides a detailed summary of the conversion rates achieved at various temperatures throughout the test.

Table 4.21. NO_x conversion efficiency of the BEA zeolite-based catalysts under 2 kW load at 40000 h^{-1}

Temperature (°C)	Sm0-BEA	Sm1-BEA	Sm2-BEA	Sm4-BEA
240	91.6786	93.4464	92.7265	93.5295
230	91.4843	93.1490	92.5222	92.6362
220	91.3571	92.9922	92.0628	92.2885
210	91.0933	92.6175	91.9017	90.8517
200	90.4533	92.2182	91.4717	90.4273
190	90.2360	91.5193	91.3536	89.5633
180	89.6964	90.7800	90.5041	88.2450
170	88.9415	90.1046	89.0518	87.9000
160	88.1920	88.2908	87.7850	87.5000
150	86.1667	87.5088	86.6986	87.2659
Average (%)	**89.9299**	**91.2627**	**90.6078**	**90.0207**

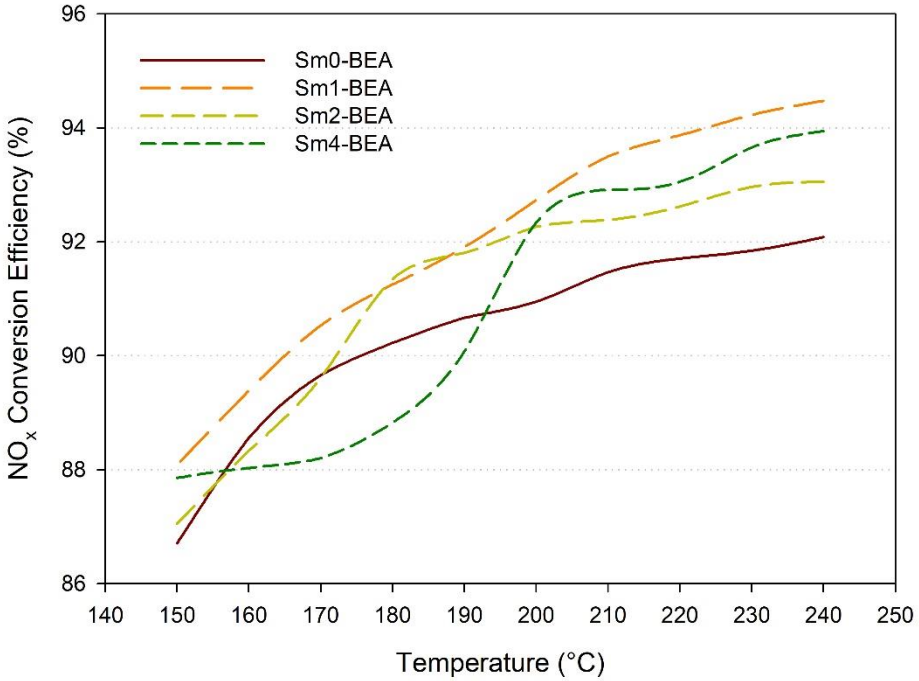

Figure 4.45. NO_x conversion efficiency of the BEA zeolite-based catalysts under 4 kW load at 40000 h^{-1}

Figure 4.45 illustrates NO_x conversion efficiency for Sm0-BEA, Sm1-BEA, Sm2-BEA, and Sm4-BEA under a 4-kW load condition and a space velocity of 40000 h^{-1} across a temperature range from 150°C to 240°C. Under a 4-kW load, Sm1-BEA demonstrates the highest NO_x conversion efficiency, followed closely by Sm4-BEA and Sm2-BEA. Sm0-BEA lags behind, emphasizing the importance of Sm loading in achieving optimal NO_x reduction performance.

Table 4.22. NO_x conversion efficiency of the BEA zeolite-based catalysts under 4 kW load at 40000 h^{-1}

Temperature (°C)	Sm0-BEA	Sm1-BEA	Sm2-BEA	Sm4-BEA
240	92.0828	94.4719	93.0510	93.9400
230	91.8450	94.2268	92.9600	93.6541
220	91.7060	93.8677	92.6178	93.0516
210	91.4650	93.4938	92.3820	92.9089
200	90.9490	92.7300	92.2613	92.3411
190	90.6644	91.9083	91.8049	90.0757
180	90.2260	91.2500	91.3486	88.8250
170	89.6586	90.5300	89.6140	88.1996
160	88.5560	89.3875	88.3320	88.0265
150	86.7100	88.0886	87.0500	87.8533
Average (%)	**90.3863**	**91.9955**	**91.1422**	**90.8876**

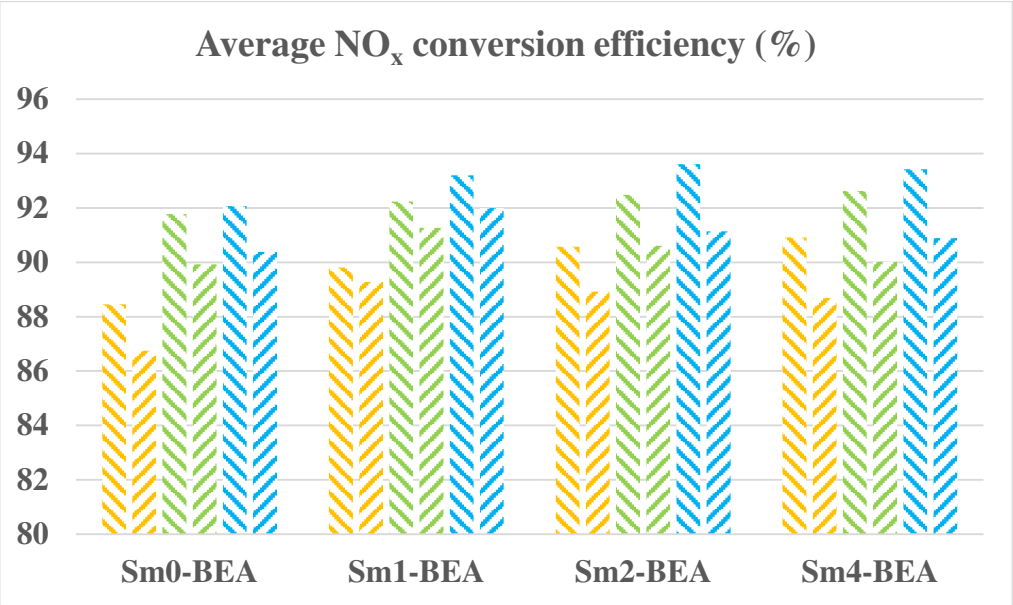

Figure 4.46. Average NO_x conversion efficiency for BEA zeolite-based catalysts

Figure 4.46 illustrates the average NO_x conversion efficiencies for BEA zeolite-based catalysts between 150 to 240 °C for loads of 0, 2, and 4 kW, represented by the orange, green, and blue lines, respectively. Additionally, the left-leaning lines denote average conversion rates achieved at a space velocity of 30000 h^{-1}, while the right-leaning lines indicate those obtained at a space velocity of 40000 h^{-1}. For each sample, the NO_x conversion efficiency increases with higher load. At a space velocity of 30000 h^{-1}, conversion efficiencies tend to be slightly higher compared to 40000 h^{-1} for the same load and sample. These trends indicate that both increased load and lower space velocity contribute to improved NO_x conversion efficiency across the samples in the specified temperature range. When the comparison of Figure 4.37 and 4.46, BEA-based samples achieve better NO_x conversion than Y-based samples, with more pronounced improvements at higher loads and space velocities. This could imply that BEA-type zeolite structures are more suitable for applications targeting high NO_x conversion rates under varying load and flow conditions.

4.7. Cost analysis

SCR catalysts are essential in reducing NO_x emissions from diesel engines, playing a critical role in meeting stringent environmental regulations. A cost analysis of SCR catalysts involves evaluating the upfront investment and operational costs associated with their production, installation, and maintenance. Factors influencing these costs include the materials used, such as precious metals, catalyst design, system integration, and the expenses related to periodic catalyst replacement and reductant consumption. Understanding these costs is crucial for optimizing the economic feasibility and overall performance of SCR systems in automotive applications. Tables 4.23 and 4.24 present the cost analysis of the produced SCR catalysts. As evidenced by the data, an increase in Sm content

has resulted in a corresponding rise in for both catalyst groups costs. Figure 4.47 is presented in order to better understand price changes. Although the same chemical proportions were utilized, the variation in the support element, specifically the type of zeolites used, is the primary factor contributing to the price difference between the two groups.

Table 4.23. Cost analysis for Y zeolite-based catalysts

Catalyst	Chemical	Usage Ratio (%)	Used amount of chemical (g)	Unit Price ($/kg)	Cost ($)
Sm0-Y	Sm_2O_3	0	0	**2050**	0
	CeO_2	0.3	0.185	**910**	0.168
	$CuCl_2$	4	5.366	**142**	0.762
	Zeolite Y	96	48.000	**756**	36.288
				Total	**37.218**
Sm1-Y	Sm_2O_3	1	1.160	**2050**	2.378
	CeO_2	0.3	0.185	**910**	0.168
	$CuCl_2$	4	5.366	**142**	0.762
	Zeolite Y	95	47.500	**756**	35.910
				Total	**39.218**
Sm2-Y	Sm_2O_3	2	2.320	**2050**	4.756
	CeO_2	0.3	0.185	**910**	0.168
	$CuCl_2$	4	5.366	**142**	0.762
	Zeolite Y	94	47.000	**756**	35.532
				Total	**41.218**
Sm4-Y	Sm_2O_3	4	4.639	**2050**	9.510
	CeO_2	0.3	0.185	**910**	0.168
	$CuCl_2$	4	5.366	**142**	0.762
	Zeolite Y	92	46.000	**756**	34.776
				Total	**45.216**

Table 4.24. Cost analysis for BEA zeolite-based catalysts

Catalyst	Chemical	Usage Ratio (%)	Used amount of chemical (g)	Unit Price ($/kg)	Cost ($)
Sm0-BEA	Sm_2O_3	0	0	**2050**	0
	CeO_2	0.3	0.185	**910**	0.168
	$CuCl_2$	4	5.366	**142**	0.762
	Zeolite BEA	96	48.000	**1100**	52.8
				Total	**53.730**
Sm1-BEA	Sm_2O_3	1	1.160	**2050**	2.378
	CeO_2	0.3	0.185	**910**	0.168
	$CuCl_2$	4	5.366	**142**	0.762
	Zeolite BEA	95	47.500	**1100**	52.25
				Total	**55.558**
Sm2-BEA	Sm_2O_3	2	2.320	**2050**	4.756
	CeO_2	0.3	0.185	**910**	0.168
	$CuCl_2$	4	5.366	**142**	0.762
	Zeolite BEA	94	47.000	**1100**	51.7
				Total	**57.386**
Sm4-BEA	Sm_2O_3	4	4.639	**2050**	9.510
	CeO_2	0.3	0.185	**910**	0.168
	$CuCl_2$	4	5.366	**142**	0.762
	Zeolite BEA	92	46.000	**1100**	50.60
				Total	**61.040**

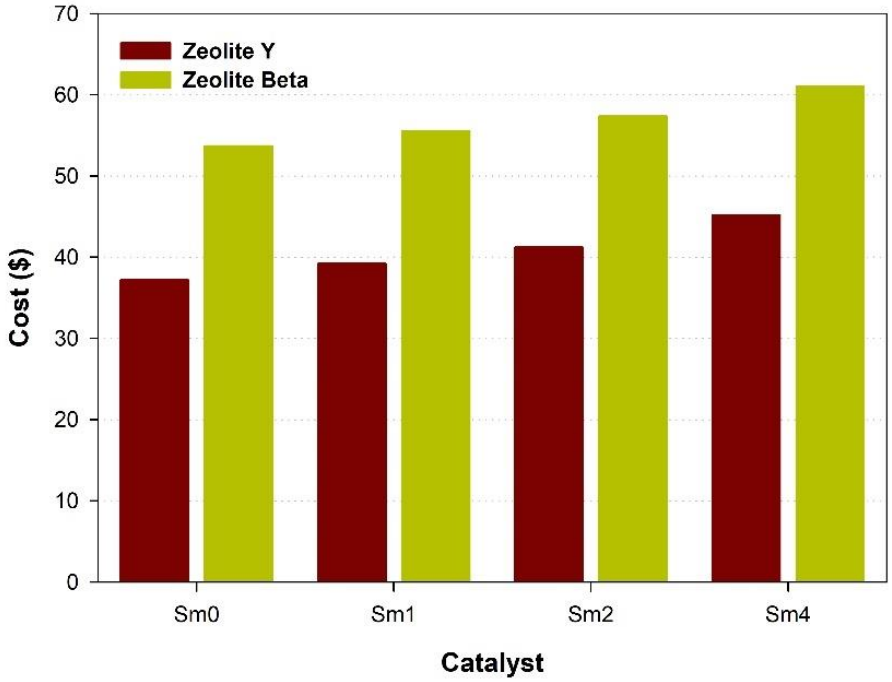

Figure 4.47. Cost comparison of produced catalysts

A commercially produced catalyst was also examined in the cost analysis section. In this study, the total weight of chemicals used in catalyst production was standardized at 50 g. The same amount was also considered for the production of the commercial catalyst. Details of the examined catalyst are given in Table 4.25. Upon examining the production cost of the commercially used catalyst, it was found that its production cost was significantly lower compared to the catalysts prepared within the scope of this study. Therefore, the commercialization of the produced zeolite-based catalysts may take time.

Table 4.25. Cost analysis for commercial catalyst (Long et al., 2021)

Commercial catalyst	Chemical	Molar Ratio	Used amount of chemical (g)	Unit Price ($/kg)	Cost ($)
V_2O_5-WO_3/TiO_2	V_2O_5	1.62	3.549	405	1.437
	WO_3	1	2.793	415	1.159
	TiO_2	45.41	43.697	75	3.277
				Total	**5.873**

5. CONCLUSIONS

In this thesis, two different catalyst sets, which a total of eight catalysts, were produced for SCR tests under real exhaust flow conditions. The Y and BEA zeolite sets were tested under loads of 0, 2, and 4 kW at two different space velocities in a temperature range of 150 °C to 240 °C. The chemical characterization of the catalysts was determined using SEM, EDS, XRD, FT-IR, and BET analyses. The outcomes from this study can be summarized as follows:

- Initially, the acid treatment of the main structure (cordierite) led to the formation of cracks, which increased its specific surface area.
- Surface morphologies were revealed through SEM and EDS analyses, indicating a uniform distribution of all the chemicals used in the catalysts.
- Due to the inherent nature of cordierite and zeolites, the dominance of Si, O, and Al contents was observed in all catalysts. Additionally, the presence of other chemicals used (Cu, Ce, and Sm) was confirmed through analyses.
- For both sets, EDS mapping results demonstrated that the Sm addition increased proportionally in the catalysts produced with a higher percentage of Sm incorporation.
- It was observed that the surface areas of the Y zeolite set catalysts (Sm0-Y, Sm1-Y, Sm2-Y, and Sm4-Y) increased by 210, 290, 250, and 125 times, respectively. Similarly, in the Beta zeolite set, the surface area enhancement ratios for the catalysts (Sm0-BEA, Sm1-BEA, Sm2-BEA, and Sm4-BEA) were determined to be 150, 140, 150, and 130, respectively.
- The highest specific surface area in the Y zeolite set was 143.7719 m^2/g, belonging to Sm1-Y, while in the BEA set, the catalyst with the highest specific surface area was Sm2-BEA, with a value of 74.8524 m^2/g.
- Strong XRD peaks corresponding to cordierite and zeolites were observed in the 10° to 30° range, and it was concluded that the crystal structure of cordierite is orthorhombic, Y zeolite is cubic, and BEA zeolite is tetragonal.
- The peaks corresponding to Sm were observed in the 30° to 50° range, and it was determined to have a hexagonal crystal structure.
- The FT-IR spectra reveal characteristic peaks indicating the structural integrity of the Y zeolite, with Si-O and Al-O vibrations remaining intact despite Sm and Cu modifications. Peaks in the 580–766 cm^{-1} range and slight shifts in lower wavenumbers suggest the integration of Sm and Cu into the zeolite structure and potential structural changes at higher Sm concentrations.

- The FT-IR spectra of BEA zeolite indicate the structural stability of the Si-O-Al framework, with characteristic peaks showing minimal changes despite the addition of Sm and Cu. Peaks in the 564–768 cm^{-1} range suggest the integration of Sm and Cu into the zeolite matrix, potentially influencing its catalytic properties.
- For all catalysts, the conversion rates improved with rising temperatures. An increase in engine load positively influenced the conversion rate, whereas a higher SV had a negative impact.
- Under a load of 4 kW, the highest NO_x conversion rate of 95.7481% was achieved using the Sm1-Y catalyst at an SV of 30000 h^{-1}. At an SV of 40000 h^{-1}, the Sm2-Y catalyst exhibited a NO_x conversion rate of 94.6600% at a temperature of 240 °C.
- Under a load of 4 kW, the highest NO_x conversion rate of 95.7754% was achieved using the Sm4-BEA catalyst at an SV of 30000 h^{-1}. At an SV of 40000 h^{-1}, the Sm1-BEA catalyst exhibited a NO_x conversion rate of 94.4719% at a temperature of 240 °C.
- Comparing the average NO_x conversion rates in the temperature range of 150-240 °C, the catalysts with the highest average conversion rates for the Y zeolite-based catalyst set were Sm1-Y as 93.4842% for 30000 h^{-1} and Sm2-Y as 90.4577% for 40000 h^{-1}.
- Comparing the average NO_x conversion rates in the temperature range of 150-240 °C, the catalysts with the highest average conversion rates for the BEA zeolite-based catalyst set were Sm2-BEA as 93.6098% for 30000 h^{-1} and Sm1-BEA as 91.9955% for 40000 h^{-1}.
- The addition of Sm demonstrated positive effects for both catalyst sets. Based on the results, it was concluded that the optimal Sm loading rates were 1% and 2%.

Although the study has yielded convincing results, there is still room for further improvement. For instance, even better outcomes could potentially be achieved by employing more than one SCR catalysts and injecting the reductant before each catalysts. Additionally, the catalysts developed in this study could be produced using different coating methods, providing an opportunity to evaluate the influence of these methods on catalyst performance. Moreover, exploring the use of different hydrocarbons or oxygenated hydrocarbons as reductants could offer valuable insights into optimizing NO_x reduction efficiency. Another promising avenue for future research involves studying the performance of the catalysts at higher temperatures to better understand how their efficiency changes compared to their behavior at lower temperatures. Investigating the interaction of samarium with catalysts prepared using lower-cost zeolites could provide a cost-effective approach to enhancing NO_x conversion, contributing to the development of more economical and efficient catalytic systems. The performance of catalysts and the efficiency of SCR systems could be optimized using artificial intelligence (AI) and machine learning algorithms. This approach would

allow real-time analysis of system parameters to achieve the best possible outcomes. Studies could focus on the recycling and reuse of spent catalysts. This would not only reduce costs but also contribute to minimizing environmental impacts.

REFERENCES

Amano, F., Suzuki, S., Yamamoto, T., and Tanaka, T. 2006. One-electron reducibility of isolated copper oxide on alumina for selective NO–CO reaction. Applied Catalysis B: Environmental, 64(3–4), 282–289. doi:10.1016/j.apcatb.2005.12.011

Bai, Y., Bian, X., and Wu, W. 2019. Catalytic properties of CuO/CeO2-Al2O3 catalysts for low concentration NO reduction with CO. Applied Surface Science, 463, 435–444. doi:10.1016/j.apsusc.2018.08.229

Ballor, G. 2023. Liberal Environmentalism: The Public-Private Production of European Emissions Standards. Business History Review, 97(3), 575–601. doi:10.1017/S0007680523000272

Barbero, B. P., and Cadus, L. E. 2002. Evaluation and characterization of Sm-V-O catalytic system for propane oxydehydrogenation: Sm2O3-impregnated V2O5 catalysts. Applied Catalysis A: General, 234(1–2), 245–258. doi:10.1016/S0926-860X(02)00228-4

Bartolomeu, R., Henriques, C., da Costa, P., and Ribeiro, F. 2011. deNOx over Ag/H-ZSM-5: Study of NO2 interaction with ethanol. Catalysis Today, 176(1), 81–87. doi:10.1016/j.cattod.2011.02.009

Borchers, M., Lott, P., and Deutschmann, O. 2023. Selective Catalytic Reduction with Hydrogen for Exhaust gas after-treatment of Hydrogen Combustion Engines. Topics in Catalysis, 66(13–14), 973–984. doi:10.1007/s11244-022-01723-1

Bowman, C. T. 1975. Kinetics of pollutant formation and destruction in combustion. Progress in Energy and Combustion Science, 1(1), 33–45. doi:10.1016/0360-1285(75)90005-2

Cao, L., Wang, Q., and Yang, J. 2020. Ultrafine Pt particles directed by polyvinylpyrrolidone on zeolite beta as an efficient low-temperature H2-SCR catalyst. Journal of Environmental Chemical Engineering, 8(1), 103631. doi:10.1016/j.jece.2019.103631

Cao, Y., Feng, X., Xu, H., Lan, L., Gong, M., and Chen, Y. 2016. Novel promotional effect of yttrium on Cu-SAPO-34 monolith catalyst for selective catalytic reduction of NOx by NH3 (NH3-SCR). Catalysis Communications, 76, 33–36. doi:10.1016/j.catcom.2015.12.022

Chen, L., Yang, J., Ren, S., Chen, Z., Zhou, Y., and Liu, W. 2021. Effects of Sm modification on biochar supported Mn oxide catalysts for low-temperature NH3-SCR of NO. Journal of the Energy Institute, 98, 234–243. doi:10.1016/j.joei.2021.07.003

Chen, M., Li, J., Xue, W., Wang, S., Han, J., Wei, Y., Mei, D., Li, Y., and Yu, J. 2022. Unveiling Secondary-Ion-Promoted Catalytic Properties of Cu-SSZ-13 Zeolites for Selective Catalytic Reduction of NO_x. Journal of the American Chemical Society, 144(28), 12816–12824. doi:10.1021/jacs.2c03877

Chen, Z., Ren, S., Wang, M., Yang, J., Chen, L., Liu, W., Liu, Q., and Su, B. 2022. Insights into samarium doping effects on catalytic activity and SO2 tolerance of MnFeO catalyst for low-temperature NH3-SCR reaction. Fuel, 321, 124113. doi:10.1016/j.fuel.2022.124113

Costa, C. N., and Efstathiou, A. M. 2007. Low-temperature H2-SCR of NO on a novel Pt/MgO-CeO2 catalyst. Applied Catalysis B: Environmental, 72(3–4), 240–252. doi:10.1016/j.apcatb.2006.11.010

Costa, C. N., Savva, P. G., Fierro, J. L. G., and Efstathiou, A. M. 2007. Industrial H2-SCR of NO on a novel Pt/MgO–CeO2 catalyst. Applied Catalysis B: Environmental, 75(3–4), 147–156. doi:10.1016/j.apcatb.2007.04.018

Dec, J. E. 1997, February 24. *A Conceptual Model of DI Diesel Combustion Based on Laser-Sheet Imaging**. doi:10.4271/970873

Dornoff, J., and Rodríguez, F. 2024. *Euro 7: The new emission standard for light-and heavy-duty vehicles in the European Union*. https://theicct.org/wp-content/uploads/2024/03/ID-116-–-Euro-7-standard_final_v2.pdf

Dou, B., Lv, G., Wang, C., Hao, Q., and Hui, K. 2015. Cerium doped copper/ZSM-5 catalysts used for the selective catalytic reduction of nitrogen oxide with ammonia. Chemical Engineering Journal, 270, 549–556. doi:10.1016/j.cej.2015.02.004

Du, Y., Gao, F., Tang, X., Yi, H., Zhou, Y., Zhao, S., Duan, E., Wang, J., and Qi, Z. 2023. Mechanistic insight into the enhanced NO reduction by CO over a pre-reduced CuxOy-CeO2 multiphase catalyst. Journal of Environmental Chemical Engineering, 11(5), 110386. doi:10.1016/j.jece.2023.110386

Dzwigaj, S., Janas, J., Rojek, W., Stievano, L., Wagner, F. E., Averseng, F., and Che, M. 2009. Effect of iron impurities on the catalytic activity of BEA, MOR and MFI zeolites in the SCR of NO by ethanol. Applied Catalysis B: Environmental, 86(1–2), 45–52. doi:10.1016/j.apcatb.2008.07.017

Environmental Protection Agency. 2019. *Federal and California Light-Duty Vehicle Emissions Standards for Air Pollutants*. https://nepis.epa.gov/Exe/tiff2png.cgi/P100XCIV.PNG?-r+75+-g+7+D%3A%5CZYFILES%5CINDEX%20DATA%5C16THRU20%5CTIFF%5C00000603%5CP100XCIV.TIF

Environmental Protection Agency. 2024. *Smog Vehicle Emissions*. https://www.epa.gov/greenvehicles/smog-vehicle-emissions#history

Fu, G., Yang, R., Liang, Y., Yi, X., Li, R., Yan, N., Zheng, A., Yu, L., Yang, X., and Jiang, J. 2021. Enhanced hydrothermal stability of Cu/SSZ-39 with increasing Cu contents, and the mechanism of selective catalytic reduction of NO. Microporous and Mesoporous Materials, 320, 111060. doi:10.1016/j.micromeso.2021.111060

Gajbhiye, M. D., Lakshmanan, S., Kumar, N., Bhattacharya, S., and Nishad, S. 2023. Effectiveness of India's Bharat Stage mitigation measures in reducing vehicular emissions. Transportation Research Part D: Transport and Environment, 115, 103603. doi:10.1016/j.trd.2022.103603

Gao, C., Shi, J.-W., Fan, Z., Wang, B., Wang, Y., He, C., Wang, X., Li, J., and Niu, C. 2018. “Fast SCR” reaction over Sm-modified MnOx-TiO2 for promoting reduction of NOx with NH3. Applied Catalysis A: General, 564, 102–112. doi:10.1016/j.apcata.2018.07.017

Gholami, Z., and Luo, G. 2018. Low-Temperature Selective Catalytic Reduction of NO by CO in the Presence of O_2 over Cu:Ce Catalysts Supported by Multiwalled Carbon Nanotubes. Industrial & Engineering Chemistry Research, 57(27), 8871–8883. doi:10.1021/acs.iecr.8b01343

Guan, B., Zhan, R., Lin, H., and Huang, Z. 2014. Review of state of the art technologies of selective catalytic reduction of NOx from diesel engine exhaust. Applied Thermal Engineering, 66(1–2), 395–414. doi:10.1016/j.applthermaleng.2014.02.021

Habib, H. A., Basner, R., Brandenburg, R., Armbruster, U., and Martin, A. 2014. Selective Catalytic Reduction of NO_x of Ship Diesel Engine Exhaust Gas with C_3H_6 over Cu/Y Zeolite. ACS Catalysis, 4(8), 2479–2491. doi:10.1021/cs500348b

Han, Z., Yu, Q., Xue, Z., Liu, K., and Qin, Q. 2018. Sm-doped manganese-based Zr–Fe polymeric pillared interlayered montmorillonite for low temperature selective catalytic reduction of NO_x by NH_3 in metallurgical sintering flue gas. RSC Advances, 8(73), 42017–42024. doi:10.1039/C8RA09434A

He, H., and Yang, L. 2017. *China’s Stage 6 Emission Standard for New Light-Duty Vehicles (Final Rule)*. https://theicct.org/publication/chinas-stage-6-emission-standard-for-new-light-duty-vehicles-final-rule/

Held, W., König, A., Richter, T., and Puppe, L. 1990. Catalytic NOx reduction in net oxidizing exhaust gas. SAE Technical Papers. doi:10.4271/900496

Heywood, J. B. 2018. *Internal Combustion Engine Fundamentals*. McGraw-Hill Education.

Hong, Z., Sun, X., Wang, Z., Zhao, G., Li, X., and Zhu, Z. 2019. Pt/SSZ-13 as an efficient catalyst for the selective catalytic reduction of NO_x with H_2. Catalysis Science & Technology, 9(15), 3994–4001. doi:10.1039/C9CY00898E

Hong, Z., Wang, Z., Chen, D., Sun, Q., and Li, X. 2018. Hollow ZSM-5 encapsulated Pt nanoparticles for selective catalytic reduction of NO by hydrogen. Applied Surface Science, 440, 1037–1046. doi:10.1016/j.apsusc.2018.01.239

Intergovernmental Panel on Climate Change (IPCC). 2023. *Climate Change 2021 – The Physical Science Basis*. Cambridge University Press. doi:10.1017/9781009157896

International Energy Agency. 2022. *Transport sector CO2 emissions by mode in the Sustainable Development Scenario, 2000-2030*. https://www.iea.org/data-and-statistics/charts/transport-sector-co2-emissions-by-mode-in-the-sustainable-development-scenario-2000-2030

Janas, J., and Dzwigaj, S. 2011. Physico-chemical properties of FeAlBEA and FeSiBEA zeolites and their catalytic activity in the SCR of NO with ethanol or methane. Catalysis Today, 176(1), 272–276. doi:10.1016/j.cattod.2010.12.012

Janas, J., Machej, T., Che, M., and Dzwigaj, S. 2007. State of cobalt in CoSiBEA zeolite and ITS role in NO SCR with ethanol. In *Studies in Surface Science and Catalysis* (Vol. 170, Issue B, pp. 1466–1470). Elsevier Inc. doi:10.1016/S0167-2991(07)81017-2

Japan: Heavy-duty: Emissions. 2024. Japan: Heavy-duty: Emissions

Japan: Light-duty: Emissions. 2024. https://www.transportpolicy.net/standard/japan-light-duty-emissions/

Lacis, A. A., Schmidt, G. A., Rind, D., and Ruedy, R. A. 2010. Atmospheric CO_2 : Principal Control Knob Governing Earth's Temperature. Science, 330(6002), 356–359. doi:10.1126/science.1190653

Li, X., Ren, S., Jiang, Y., Chen, Z., Wang, L., Liu, M., and Chen, T. 2023. In situ IR spectroscopy study of NO removal over CuCe catalyst for CO-SCR reaction at different temperature. Catalysis Today, 418, 114082. doi:10.1016/j.cattod.2023.114082

Li, X., Zhang, X., Xu, Y., Liu, Y., and Wang, X. 2015. Influence of support properties on H2 selective catalytic reduction activities and N2 selectivities of Pt catalysts. Chinese Journal of Catalysis, 36(2), 197–203. doi:10.1016/S1872-2067(14)60197-2

Lin, Q., Feng, X., Zhang, H., Lin, C., Liu, S., Xu, H., and Chen, Y. 2018. Hydrothermal deactivation over CuFe/BEA for NH3-SCR. Journal of Industrial and Engineering Chemistry, 65, 40–50. doi:10.1016/j.jiec.2018.04.009

Liu, F., Yang, L., Cheng, J., Wu, X., Quan, W., and Saito, K. 2019. Low Temperature deNOx Catalytic Activity with C2H4 as a Reductant Using Mixed Metal Fe-Mn Oxides Supported on Activated Carbon. Energies, 12(22), 4341. doi:10.3390/en12224341

Liu, H., Fan, Z., Sun, C., Yu, S., Feng, S., Chen, W., Chen, D., Tang, C., Gao, F., and Dong, L. 2019. Improved activity and significant SO2 tolerance of samarium modified CeO2-TiO2 catalyst for NO selective catalytic reduction with NH3. Applied Catalysis B: Environmental, 244, 671–683. doi:10.1016/j.apcatb.2018.12.001

Liu, K., Yu, Q., Qin, Q., and Wang, C. 2018. Selective catalytic reduction of nitric oxide with carbon monoxide over alumina-pellet-supported catalysts in the presence of excess oxygen. Environmental Technology, 39(15), 1878–1885. doi:10.1080/09593330.2017.1341554

Liu, S., Gao, J., Xu, W., Ji, Y., Zhu, T., Xu, G., Zhong, Z., and Su, F. 2024. Transition metal-based catalysts for selective catalytic reduction of NO by CO: A state-of-the-art review. Chemical Engineering Journal, 486, 150285. doi:10.1016/j.cej.2024.150285

Liu, Z., Yu, F., Dong, D., Gui, R., Li, W., Sun, R., Wan, Y., Dan, J., Wang, Q., and Dai, B. 2021. Transition-metal-doped ceria carried on two-dimensional vermiculite for selective catalytic reduction of NO with CO: Experiments and density functional theory. Applied Surface Science, 566, 150704. doi:10.1016/j.apsusc.2021.150704

Long, Y., Su, Y., Xue, Y., Wu, Z., and Weng, X. 2021. V_2O_5–WO_3/TiO_2 Catalyst for Efficient Synergistic Control of NO_x and Chlorinated Organics: Insights into the Arsenic Effect. Environmental Science & Technology, 55(13), 9317–9325. doi:10.1021/acs.est.1c02636

Majewski, W. A., and Jääskeläinen, H. 2023. *Diesel Emissions and Their Control, Second Edition* (Second edition). SAE International. doi:10.4271/9781468605709

Martínez-Arias, A., Hungría, A. B., Iglesias-Juez, A., Fernández-García, M., Anderson, J. A., Conesa, J. C., Munuera, G., and Soria, J. 2012. Redox and catalytic properties of CuO/CeO2 under CO+O2+NO: Promoting effect of NO on CO oxidation. Catalysis Today, 180(1), 81–87. doi:10.1016/j.cattod.2011.02.014

Mehregan, M., and Moghiman, M. 2020. Experimental investigation of the distinct effects of nanoparticles addition and urea-SCR after-treatment system on NOx emissions in a blended-biodiesel fueled internal combustion engine. Fuel, 262, 116609. doi:10.1016/j.fuel.2019.116609

Ming, S., Pang, L., Fan, C., Guo, W., Dong, Y., Liu, P., Chen, Z., and Li, T. 2019. Chemical deactivation of Cu-SAPO-18 deNO catalyst caused by basic inorganic contaminants in diesel exhaust. Chinese Journal of Catalysis, 40(4), 590–599. doi:10.1016/S1872-2067(19)63312-7

Mohan, S., Dinesha, P., and Kumar, S. 2020. NOx reduction behaviour in copper zeolite catalysts for ammonia SCR systems: A review. Chemical Engineering Journal, 384(August 2019), 123253. doi:10.1016/j.cej.2019.123253

Muhammad Farhan, S., Pan, W., Zhijian, C., and JianJun, Y. 2024. Innovative catalysts for the selective catalytic reduction of NOx with H2: A systematic review. Fuel, 355, 129364. doi:10.1016/j.fuel.2023.129364

Pan, K. L., Young, C. W., Pan, G. T., and Chang, M. B. 2020. Catalytic reduction of NO by CO with Cu-based and Mn-based catalysts. Catalysis Today, 348, 15–25. doi:10.1016/j.cattod.2019.08.038

Popovych, N. O., Kyriienko, P. I., Soloviev, S. O., Orlyk, S. M., and Dzwigaj, S. 2016. Influence of partial dealumination of BEA zeolites on physicochemical and catalytic properties of AgAlSiBEA in H 2 -promoted SCR of NO with ethanol. Microporous and Mesoporous Materials, 226, 10–18. doi:10.1016/j.micromeso.2015.12.031

Qi, G., Yang, R. T., and Rinaldi, F. C. 2006. Selective catalytic reduction of nitric oxide with hydrogen over Pd-based catalysts. Journal of Catalysis, 237(2), 381–392. doi:10.1016/j.jcat.2005.11.025

Reşitoğlu, İ. A., Altinişik, K., and Keskin, A. 2015. The pollutant emissions from diesel-engine vehicles and exhaust aftertreatment systems. Clean Technologies and Environmental Policy, 17(1), 15–27. doi:10.1007/s10098-014-0793-9

Reuters. 2024, March 13. *EU Parliament approves compromise on vehicle pollution limits*. https://www.reuters.com/world/europe/eu-parliament-approves-compromise-vehicle-pollution-limits-2024-03-13/

Ritchie, H. 2020. *Cars, planes, trains: where do CO_2 emissions from transport come from?* https://ourworldindata.org/co2-emissions-from-transport

Ritchie, H. 2023. *How much CO2 can the world emit while keeping warming below 1.5°C and 2°C?* https://ourworldindata.org/how-much-co2-can-the-world-emit-while-keeping-warming-below-15c-and-2c

Ritchie, H., and Rosado, P. 2024. *Energy Mix*. https://ourworldindata.org/energy-mix

Ritchie, H., and Roser, M. 2024, January. *CO_2 emissions*. https://ourworldindata.org/co2-emissions

Rohde, R. 2023. *Global Temperature Report for 2022*. https://berkeleyearth.org/global-temperature-report-for-2022/

Saaid, I. M., Mohamed, A. R., and Bhatia, S. 2002. Activity and characterization of bimetallic ZSM-5 for the selective catalytic reduction of NOx. Journal of Molecular Catalysis A: Chemical, 189(2), 241–250. doi:10.1016/S1381-1169(02)00330-8

Schay, Z., Guczi, L., Beck, A., Nagy, I., Samuel, V., Mirajkar, S. P., Ramaswamy, A. V., and Pál-Borbély, G. 2002. DeNO reactions on Cu-zeolites. Catalysis Today, 75(1–4), 393–399. doi:10.1016/S0920-5861(02)00088-3

Selleri, T., Melas, A. D., Joshi, A., Manara, D., Perujo, A., and Suarez-Bertoa, R. 2021. An Overview of Lean Exhaust deNOx Aftertreatment Technologies and NOx Emission Regulations in the European Union. Catalysts, 11(3), 404. doi:10.3390/catal11030404

Shigapov, A. N., Graham, G. W., McCabe, R. W., Paputa Peck, M., and Kiel Plummer, H. 1999. The preparation of high-surface-area cordierite monolith by acid treatment. Applied Catalysis A: General, 182(1), 137–146. doi:10.1016/S0926-860X(99)00003-4

Sierra-Pereira, C. A., and Urquieta-González, E. A. 2014. Reduction of NO with CO on CuO or Fe2O3 catalysts supported on TiO2 in the presence of O2, SO2 and water steam. Fuel, 118, 137–147. doi:10.1016/j.fuel.2013.10.054

Stephens, L. 2020, September 28. *How Does a Diesel Exhaust System Work?* http://nmema.org/diesel-exhaust-system/

Ström, L., Carlsson, P. A., Skoglundh, M., and Härelind, H. 2018. Surface species and metal oxidation state during H2-assisted NH3-SCR of NOx over alumina-supported silver and indium. Catalysts, 8(1). doi:10.3390/catal8010038

Sun, C., Liu, H., Chen, W., Chen, D., Yu, S., Liu, A., Dong, L., and Feng, S. 2018. Insights into the Sm/Zr co-doping effects on N2 selectivity and SO2 resistance of a MnOx-TiO2 catalyst for the NH3-SCR reaction. Chemical Engineering Journal, 347, 27–40. doi:10.1016/j.cej.2018.04.029

Tylecote, R. F. 1992. *A history of metallurgy* (2nd edition). Maney Publising.

Valanidou, L., Theologides, C., Zorpas, A. A., Savva, P. G., and Costa, C. N. 2011. A novel highly selective and stable Ag/MgO-CeO2-Al2O3 catalyst for the low-temperature ethanol-SCR of NO. Applied Catalysis B: Environmental, 107(1–2), 164–176. doi:10.1016/j.apcatb.2011.07.010

Vignesh, R., and Ashok, B. 2020. Critical interpretative review on current outlook and prospects of selective catalytic reduction system for De-NOx strategy in compression ignition engine. Fuel, 276, 117996. doi:10.1016/j.fuel.2020.117996

Wang, H., Xu, R., Jin, Y., and Zhang, R. 2019. Zeolite structure effects on Cu active center, SCR performance and stability of Cu-zeolite catalysts. Catalysis Today, 295–307. doi:10.1016/j.cattod.2018.04.035

Wang, J., Liu, J., Tang, X., Xing, C., and Jin, T. 2021. The promotion effect of niobium on the low-temperature activity of Al-rich Cu-SSZ-13 for selective catalytic reduction of NOx with NH3. Chemical Engineering Journal, 418, 129433. doi:10.1016/j.cej.2021.129433

Wang, L., Chen, H., Yuan, M.-H., Rivillon, S., Klingenberg, E. H., Li, J. X., and Yang, R. T. 2014. Selective catalytic reduction of nitric oxide by hydrogen over Zn-ZSM-5 and Pd and Pd/Ru based catalysts. Applied Catalysis B: Environmental, 152–153, 162–171. doi:10.1016/j.apcatb.2014.01.036

Wang, W., Herreros, J. M., Tsolakis, A., and York, A. P. E. 2015. Increased NO2 concentration in the diesel engine exhaust for improved Ag/Al2O3 catalyst NH3-SCR activity. Chemical Engineering Journal, 270(2), 582–589. doi:10.1016/j.cej.2015.02.067

Wang, Y., Shi, X., Shan, Y., Du, J., Liu, K., and He, H. 2020. Hydrothermal Stability Enhancement of Al-Rich Cu-SSZ-13 for NH $_3$ Selective Catalytic Reduction Reaction by Ion Exchange with Cerium and Samarium. Industrial & Engineering Chemistry Research, 59(14), 6416–6423. doi:10.1021/acs.iecr.0c00285

Wen, B. 2002. NO reduction with H2 in the presence of excess O2 over Pd/MFI catalyst. Fuel, 81(14), 1841–1846. doi:10.1016/S0016-2361(02)00141-2

Wikipedia. 2022. *European emission standards for heavy-duty diesel engines*. https://en.wikipedia.org/wiki/European_emission_standards#Emission_standards_for_trucks_and_buses

Wilken, N., Nedyalkova, R., Kamasamudram, K., Li, J., Currier, N. W., Vedaiyan, R., Yezerets, A., and Olsson, L. 2013. Investigation of the effect of accelerated hydrothermal aging on the Cu sites in a Cu-BEA catalyst for NH3-SCR applications. Topics in Catalysis, 56(1–8), 317–322. doi:10.1007/s11244-013-9973-9

Wrangham, R. 2017. Control of Fire in the Paleolithic. Current Anthropology, 58(S16), S303–S313. doi:10.1086/692113

Xu, J., Qin, Y., Wang, H., Guo, F., and Xie, J. 2020. Recent advances in copper-based zeolite catalysts with low-temperature activity for the selective catalytic reduction of NO_x with hydrocarbons. New Journal of Chemistry, 44(3), 817–831. doi:10.1039/C9NJ04735B

Xu, Q., Fang, Z., Chen, Y., Guo, Y., Guo, Y., Wang, L., Wang, Y., Zhang, J., and Zhan, W. 2020. Titania–Samarium–Manganese Composite Oxide for the Low-Temperature Selective Catalytic Reduction of NO with NH_3. Environmental Science & Technology, 54(4), 2530–2538. doi:10.1021/acs.est.9b06701

Yang, L., and He, H. 2018. *China's Stage VI Emission Standard for Heavy-Duty Vehicles (final rule)*. https://www.theicct.org/publications/urban-cycle-

Yu, Q., Richter, M., Li, L., Kong, F., Wu, G., and Guan, N. 2010. The promotional effect of Cr on catalytic activity of Pt/ZSM-35 for H2-SCR in excess oxygen. Catalysis Communications, 11(11), 955–959. doi:10.1016/j.catcom.2010.03.021

Yue, Y., Liu, B., Lv, N., Wang, T., Bi, X., Zhu, H., Yuan, P., Bai, Z., Cui, Q., and Bao, X. 2019. Direct Synthesis of Hierarchical FeCu-ZSM-5 Zeolite with Wide Temperature Window in Selective Catalytic Reduction of NO by NH_3. ChemCatChem, 11(19), 4744–4754. doi:10.1002/cctc.201901104

Zhang, Q., Zhang, S., Hu, X., and Huang, Y. 2024. Effect of samarium doping on the activity and sulfur resistance of Ce/MnFeO catalyst for low-temperature selective catalytic reduction of NO by ammonia. Chinese Journal of Chemical Engineering, 71, 272–282. doi:10.1016/j.cjche.2024.03.012

Zhang, S., Zhang, B., Wu, B., Liu, B., and Zhang, S. 2023. Effect of samarium on the N2 selectivity of SmxMn0.3−xTi catalysts during selective catalytic reduction of NOx with NH3. International Journal of Minerals, Metallurgy and Materials, 30(4), 642–652. doi:10.1007/s12613-021-2348-5

Zhu, N., Shan, Y., Shan, W., Sun, Y., Liu, K., Zhang, Y., and He, H. 2020. Distinct NO_2 Effects on Cu-SSZ-13 and Cu-SSZ-39 in the Selective Catalytic Reduction of NO_x with NH_3. Environmental Science & Technology, 54(23), 15499–15506. doi:10.1021/acs.est.0c06256

CURRICULUM VITAE

Ali Cem YAKARYILMAZ. Completed his primary education at Atatürk Primary School in 2006 and graduated from Osmaniye Hasan Aybaba Anatolian Teacher High School in 2010. He began his Bachelor of Science (BSc) studies in Automotive Engineering at Çukurova University in 2010. Following his undergraduate degree, he pursued a Master of Science (MSc) in Automotive Engineering at Çukurova University in 2017, successfully graduating in 2018. Subsequently, he commenced his PhD studies in the same department in 2018. Since May 2017, he has been serving as a research assistant in the Automotive Engineering Department at Çukurova University.